Developing Simple and Reliable Tools for Chemical Analysis Using Droplet-Based Microfluidic Platforms.

BY

Michael Francis DeLaMarre
B.S., Grand Valley State University, 2009

THESIS

Submitted as partial fulfillment of the requirements
for the degree of Doctor of Philosophy in Chemistry
in the Graduate College of the
University of Illinois at Chicago, 2015

Chicago, Illinois

Defense Committee:

Scott Shippy, Chair and Advisor
Leslie Fung
Luke Hanely
Yoshitaka Ishi
David Eddington, Bioengineering

This work is dedicated to my wife Sara, who inspires me to be better in everything I do.

ACKNOWLEDGEMENTS

A Ph.D. is something I have been working towards for my entire life. Along the way I have been fortunate to have support and encouragement from many people in my life.

I would like to thank my committee members, Dr. David Eddington, Dr. Leslie Fung, Dr. Luke Hanely, and Dr. Yoshitaka Ishi, for helping me complete this last step of my Ph.D. I sincerely appreciate the time and effort you put into helping me edit my thesis.

When I first began my Ph.D. work, UIC's Microenvironmental Control Foundry, directed by Dr. David Eddington, generously funded my first microfluidic project. This project went on to shape the rest of my graduate research. I would like to thank Dr. David Eddington, the Foundry, and UIC for providing this introduction to microfluidics. I would also like to thank Dr. Shawn Oppegard. During his post-doctorate work with Dr. Eddington, Shawn generously helped me learn microfluidic fabrication techniques. I would also like to thank the UIC Machine Shop for their expertise and exceptional craftsmanship, especially Richard Frueh, Kevin Lynch, and Curt Cornell

Perhaps one of the most pleasant parts of my graduate work at UIC was the atmosphere within the research group of Dr. Scott Shippy. I consider myself fortunate that I had the opportunity to do research in such a collaborative environment with coworkers I am happy to call friends. I would like to thank all current and past group members for their friendship, especially Geovannie Ojeda-Torres, Srivani Borra, Qi Zeng, Vitaly Avilov, and Marisa Becker.

As of this year I have been in school for 22 years. Along the way I have had outstanding teachers who taught me the skills required to succeed. These teachers also taught me to be passionate about learning. I would like to thank all my previous teachers, especially Dr. Mary Karpen, Dr. Andrew Lantz, and Mrs. Andrea Spaanstra.

College has been the most challenging, most rewarding, and most fun experience of my life. I firmly believe that college should not be challenging for financial reasons. I would like to thank my grandparents for their financial support during my undergraduate experience. Being able to focus on my education, rather than tuition, was a huge relief.

The first three semester of graduate school were the hardest for me. I would like to thank my wife, Sara, for her love and encouragement during that time. She, more than anyone, gives me the strength to continue perusing my passions.

I have had enough jobs to know that any job is only as good as your boss. I would like to thank Dr. Scott Shippy for being the best boss I've ever had. He made my graduate experience one of the best jobs I've ever had, and I have grown into the scientist I am today under his mentorship.

Lastly I would like to thank my parents, who more than anyone else in my life have always encouraged my curiosity and passion for learning. Weather it was helping me hunt for food to keep my pet snake alive or building stilts for me to walk around the block on, my parents have always inspired me to explore the world around me.

MFD

STATEMENT OF CONTRIBUTION OF CORRESPONDING AUTHORS

Chapter 1 is an introductory chapter which I wrote reviewing research in the area of microfluidics over the past several decades. Chapter 2 is based on a published manuscript [M. DeLaMarre, A. Keyzer, and S. Shippy, *Development of a Simple Droplet-Based Microfluidic Capillary Viscometer for Low-Viscosity Newtonian Fluids*, Analytical Chemistry, 2015. 87(9): p. 4649-4657.] which I was the first author on. Experiments related to measurement of slopes at varying aqueous and oil inlet lengths were performed by Alec Keyzer under my instruction. I performed all other experiments. I also performed all device fabrication, wrote the manuscript, and helped in experimental design. Dr. Scott Shippy aided in experimental design and manuscript editing. Chapter 3 is based on an unpublished manuscript. I performed all experiments, fabricated all devices, helped with experimental design, and wrote the manuscript. Dr. Scott Shippy aided in experimental design and manuscript editing. Chapter 4 is based on a published manuscript [M. DeLaMarre and S. Shippy, *Development of a Simplified Microfluidic Injector for Analysis of Droplet Content via Capillary Electrophoresis*, Analytical Chemistry, 2014. 86(20): p. 10193-10200.] which I was the first author on. Dr. Shawn Oppegard instructed me in microfluidic fabrication techniques, performed all photolithography for fabrication of silica masters, and helped in device fabrication. I helped in device fabrication, performed all experiments, helped in experimental design, and wrote the manuscript. Dr. Scott Shippy helped with experimental design and in editing the manuscript. Chapter 5 is based on two unpublished experiments. I performed all device fabrication and experimental design, and performed all experiments. Chapter 6 consists of conclusions I have drawn based on my research.

TABLE OF CONTENTS

TABLE OF CONTENTS (CONTINUED)

TABLE OF CONTENTS (CONTINUED)

TABLE OF CONTENTS (CONTINUED)

LIST OF FIGURES

FIGURE PAGE

LIST OF FIGURES (CONTINUED)

FIGURE PAGE

LIST OF TABLES

TABLE PAGE

LIST OF ABBREVIATIONS

BGE	Background Electrolyte
BSA	Bovine Serum Albumin
C_a	Capillary Number
CE	Capillary Electrophoresis
CFA	Continuous Flow Analysis
ESI-MS	Electrospray Ionization Mass Spectrometry
f	Droplet Frequency
GC	Gas Chromatography
i.d.	Inner Diameter
LC	Liquid Chromatography
LOC	Lab on a Chip
LOD	Limit of Detection
MALDI	Matrix-Assisted Laser Desorption/Ionization MS
MPT	Multiple Particle Tracking
MS	Mass Spectrometry
NMR	Nuclear Magnetic Resonance
o.d.	Outer Diameter
PDMS	Polydimethylsiloxane
PFD	Perfluorodecalin
PFO	1H,1H,2H,2H-Perfluoro-1-octanol
P_L	Laplace Pressure
RSD	Relative Standard Deviation
$\dot{\gamma}$	Shear Rate
TCPFOS	Trichloro(1H,1H,2H,2H-perfluorooctyl)silane
UV-Vis	Ultra Violet Visible

SUMMARY

Two-phase flow is more complicated than single phase flow, which adds an additional layer of complexity to droplet microfluidic systems. This can cause problems with reliability, making use of droplet platforms for routine analysis particularly difficult. This work aims at developing new, reliable droplet microfluidic tools for chemical analysis by using simple design principles.

The theory and demonstration of two simple droplet microfluidic viscometers with complementary operating modes is presented. The viscometers utilize either droplet frequency or the spacing of droplets in a droplet train to determine the viscosity of nanoliter-scale samples. Accuracy and precision were characterized and found to be equivalent to or better than many commercial viscometers. Depending on the specific design, viscosities spanning three orders of magnitude could be measured at shear rates spanning four orders of magnitude. Measurement of nonaqueous and aqueous samples was demonstrated, and a combination of surface fluorination and use of a fluorous surfactant was used to allow compatibility with protein solutions containing up to 26 mg/mL BSA. Viscosity could also be determined from a fluorescence trace of droplets, making simultaneous spectroscopic analysis and rheological characterization of samples possible. The simple designs allowed for reliable operation, and could allow for integration of viscometric measurement capabilities into existing droplet platforms with minimal changes to microfluidic architectures.

A microfluidic injector capable of delivering 750 pL aqueous sample droplets to a capillary for separation by capillary electrophoresis is also presented. The design is extremely simple and consists of two straight channels interfaced out of plane in the shape of a cross. Injector precision and separation efficiency were characterized and found to be acceptable. To demonstrate use of droplets for storing temporal information, a droplet train containing a step change in riboflavin concentration was injected. Temporal resolutions down to 15 s were possible. Riboflavin assay in human urine was also

performed to demonstrate a practical use for the injector. The simple nature of the design ensured reliable operation and may allow device fabrication by nontraditional means, which could make the design more available to research groups with limited access to expensive microfabrication equipment.

1. Introduction

1.1 Miniaturization in Science and Technology

Since the invention of the integrated circuit in 1959 (Kilby, 1964) miniaturization has been arguably the largest driving force in science and technology, with companies continuing to invest heavily in scaling technology down even today. The drive to scale technology down stems from a number of benefits. For instance, material costs associated with the manufacturing process are decreased and miniaturization continues to make technology more mobile and portable. Some of the most compelling reasons to downscale technology involve leveraging benefits based on material properties which depend on scale, such as electrical conductivity, thermal conductivity, and mass transfer. Some properties, such as quantum mechanical ones, are only accessible on small scales. Generally scaling benefits are used to improve the speed or quality of a technology while reducing its cost. The miniaturization of the integrated circuit has arguably been one of the most impactful technological breakthroughs in human history, and has allowed previously unimaginable achievements such as space flight and the modern smart phone.

The integrated circuit is based on transfer of electrical charge. This generates heat, which must also be transferred to avoid overheating. Both the transfer of electrical charge and heat occur through a medium (conduction). Many applications in science and technology involve transfer of mass, rather than electrical charge or heat transfer, which is based on active or passive flow of fluids rather than conduction through a medium. Consequentially, miniaturization in technologies involving fluids has been much slower than miniaturization in electronics. Over the past two decades, however, fabrication techniques developed for the electronics industry, such as lithography, have begun being used for microfabrication of fluidic systems. This new field, termed “microfluidics”, has the potential to revolutionize science and technology in the same way the integrated circuit did in 1959.

1.2 Microfluidics

1.2.1 A Brief History of Microfluidics

Modern microfluidic chips or Lab on a Chip (LOC) platforms are devices designed to automate and miniaturize a wide range of routine laboratory procedures. The advent of the modern lab on a chip began in 1979 with the construction of a miniaturized gas chromatographic air analyzer. (Terry et al., 1979) This miniature gas chromatography (GC) system achieved a reduction in size of three orders of magnitude compared with traditional GC systems by etching an injection valve and chromatographic column onto a silicon chip. While this represented a major leap forward for efforts in miniaturizing laboratory equipment, silicon and glass etching techniques are technically challenging and time consuming. These challenges caused miniaturization of systems for laboratory analysis to remain a relatively small area of research for several decades.

In 2000 microfluidic chips made using soft lithography and PDMS were reported. (McDonald et al., 2000) The ease of using lithographic techniques to build reusable molds coupled with the ideal optical properties of PDMS lead to an explosion of interest in miniaturized fluidic systems. A number of journals exclusively dedicated to microfluidic systems were subsequently founded, including Lab on a Chip, which had an impact factor of 6.1 in 2014. (Rowe, 2015) A PubMed search for “micro” indicates growing interest in miniaturization over the past 60 years, with a surge in interest immediately following the first reports detailing the use of soft lithography and PDMS for construction of microfluidic devices. (Figure 1)

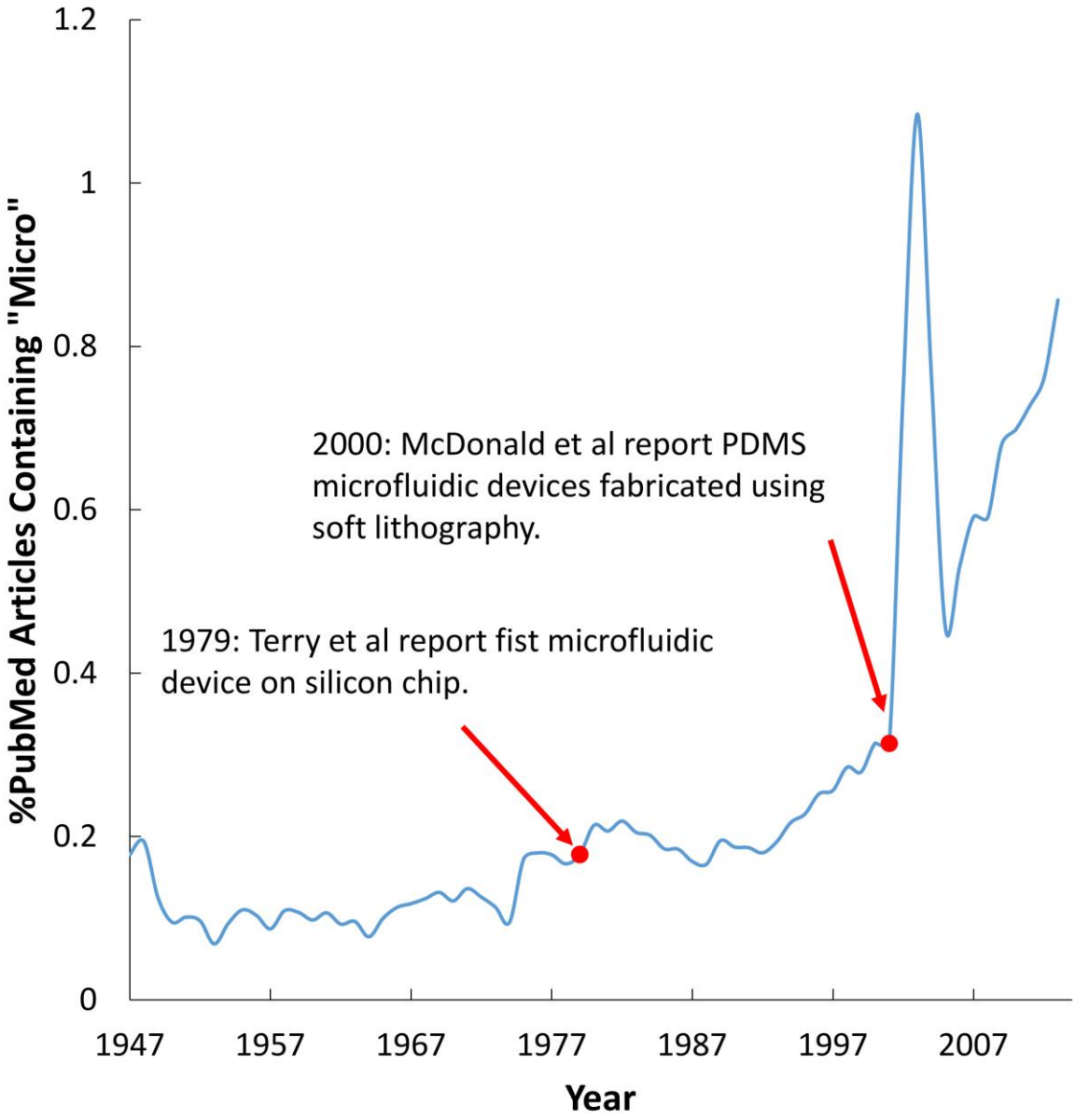

Figure 1: Percent of PubMed records containing the search term “micro” by year. Red points indicate the first report of a chip-based microfluidic device and the first report of use of PDMS for manufacture of chip-based microfluidics by soft lithography. A surge in publications containing the term “micro” accompanies the first report of a PDMS-based microfluidic device. (PubMed, 2015)

1.2.2 **Benefits of Microfluidic Platforms**

A number of aspects of fluidic systems benefit from downscaling. Scaling a fluidic system down allows for handling of smaller reagent and sample volumes. This is especially important in applications where a reagent may be cost-prohibitive in large amounts or in instances where the volume of sample available is limited. For example, *Drosophila melanogaster* is one of the most widely used animal models in genetics, but individual flies only provide 20-200 nanoliters of hemolymph. (Piyankarage et al., 2012) This makes population studies challenging, as samples must often be pooled from multiple individuals to perform analysis using traditional macroscale techniques. Another benefit of working with reduced sample and reagent volumes is decreased waste output, which makes microfluidics a promising technique for green chemistry (AlSuhaimi et al., 2009) and reduces the cost associated with chemical waste disposal.

Geometric features in microfluidic platforms, such as channel widths, are typically between 10 and 200 microns in size. At these length scales diffusion occurs much faster than in traditional fluidic systems, which makes rapid mixing of solutions possible. This allows for precise control over reagent mixing and provides a means of studying reaction kinetics on the millisecond timescale. (Arayanarakool et al., 2013; Hess et al., 2015) It also has implications for the field of chromatography, where enhanced mass transfer between phases provides more efficient separations. Heat transfer on these scales also benefits from enhanced diffusion, making it possible to precisely control on-chip temperatures and easily form temperature gradients. This has a wide range of applications including the use of temperature jumps in a wide variety of areas such as cell electrophysiology (Pennell et al., 2008) and gene expression in live cells. (Velve Casquillas et al., 2011)

Not only are microfluidic chips good for precisely controlling temperature, but the sealed nature of a glass or polymer chip isolates the experiment from the surrounding environment, which lends itself to precisely controlling the internal environment of the device. Virtually any chemical variable such as pH

(Zhou et al., 2014) and oxygen concentration (Brennan et al., 2014) may be carefully controlled on chip. Microfluidics is particularly well-suited for establishing precise concentration gradients, which is especially important in biomimetic systems. (Nguyen et al., 2011)

One final consideration pertains to how fluid flow is controlled on microfluidic platforms. To date, most microfluidic platforms are controlled by the use of external programmable pumps or pressure sources. This, in conjunction with the use of on-chip pressure controlled valves (Kim et al., 2012), has made microfluidic platforms an especially promising means of automating laboratory processes. This saves money spent on labor and could make a significant impact in industry if microfluidic platforms begin being adopted widely. One downside to controlling microfluidic platforms externally using traditional pumps, however, is that many benefits of downsizing fluidic components for incorporation on chip such as decreased laboratory footprint or portability are not realized. Recently, miniaturized pumps have begun being used in many applications requiring portable microfluidic devices. One report demonstrates use of acoustics for programmable pumping of fluids on chip using only a computer speaker and resonating chamber. (Langelier et al., 2009) Another details use of a micro syringe pump to operate a portable microfluidic capillary electrophoresis instrument on the back of a sheep for chemical monitoring of drug metabolites. (Scott et al., 2015) The mechanical properties of PDMS have even allowed for the integration of PDMS membrane-based peristaltic pumping mechanisms. (Jeong et al., 2005) Space required for the optical components of detectors has also traditionally prevented mobility and miniaturization, which is currently being addressed imbedding fiber optics into chip designs. (Liu et al., 2015)

1.3 Review of Droplet Microfluidics

1.3.1 A Brief History of Two-Phase Flow in Chemical Analysis

Two-phase flow techniques utilize two streams of immiscible fluids. One two-phase flow technique involves merging two immiscible fluid streams, such as an aqueous sample stream and air stream, at a junction to form regular segments or "slugs" of either phase in the other. Droplet microfluidics is a subfield of microfluidics centered around isolating discrete nanoliters to picoliter aqueous sample aliquots on chip to prevent diffusive mixing by utilizing two-phase flow. These discrete aliquots may then be stored, handled, and processed separately, similar to the way wells in a well plate are used, for high throughput and automated analysis. Droplet microfluidics borrows many working principles originally developed for another two-phase flow technique called continuous flow analysis (CFA), which handles fluids on the microliter scale.

Continuous flow analysis was invented in 1957 by Leonard Skeggs at Technicon Corporation. The working principle involves segmenting a continuous aqueous sample stream by injecting air bubbles into it at regular intervals (Figure 2). The sample slugs contained between air segments are sufficiently isolated from each other to prevent mixing of adjacent slugs via diffusion. These sample slugs may then be processed entirely online by adding reagents at fluidic junctions, temperature controlled incubation during transit through glass tubing, and spectroscopic detection via flow cell. The Technicon AutoAnalyzer CFA system was capable of handling hundreds of samples per hour, and saw large commercial success after being adopted in clinical and environmental labs throughout the 60's, 70's, and 80's. (Skeggs, 2000)

Despite the success of CFA, sample consumption rates remain a limiting factor for many applications. Traditional CFA systems use glass tubing with millimeter scale diameters. At this scale

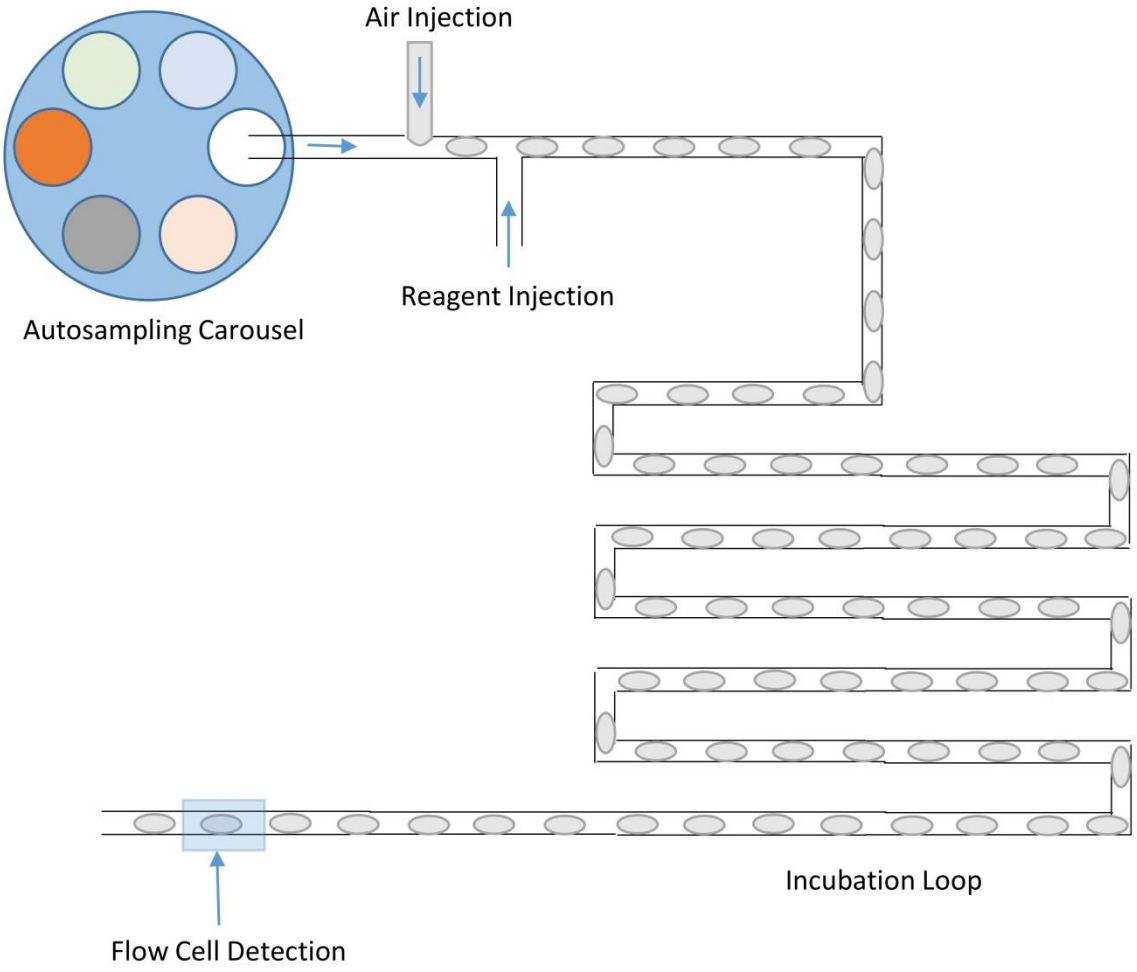

Figure 2: Diagram of a typical workflow used in continuous flow analysis. A sample stream is moved from an autosampling carousel through glass tubing and is segmented by injecting air bubbles into the stream at a junction. Reagents are then added to sample segments at subsequent junctions. Sample is incubates while in transit through an incubation loop, and is then detected via flow cell.

sample and reagent are consumed at rates of milliliters per minute. Technical difficulties associated with scaling down CFA farther, such as difficulty fabricating glass components with sub-millimeter dimensions, have prevented continued improvements in sample and reagent consumption rates. Microfluidic platforms have recently revitalized research into two-phase flow based analysis systems, however. While the use of gas phase for segmenting aqueous sample streams has been demonstrated using microfluidic junctions (Lu et al., 2015), formation of sample slugs or "droplets" in oil on chips with hydrophobic channels is more effective at preventing mixing of adjacent droplets because a wetting layer of oil exists on the surface of channels. This wetting layer prevents and also helps to prevent fouling of the microfluidic surface to some extent. Depending on the content of the droplet and type of oil phase used, mixing of droplet content can still occur via diffusion through the oil phase, especially when surfactants are included in the oil phase. (Pan et al., 2014) This makes proper selection of oil phase an important consideration. The oil phase has the added benefit of not being compressible like a gas is, so flow rates are easier to control as pressure drops across microfluidic channels. For these reasons oil/aqueous droplet microfluidic platforms are much more common than gas/aqueous systems.

1.3.2 **Droplet Production**

Droplet formation is the first step in any droplet-based microfluidic analysis scheme. The simplest and most common means of droplet formation is performed by pumping both an aqueous sample stream and immiscible oil phase through a microfluidic T-junction (Figure 3A). At the point the two streams merge, the aqueous stream breaks up into droplets with extremely regular volumes and frequency. Droplet volume typically varies by less 1%. (Theberge et al., 2010) In order to achieve more consistent droplet breakup the aqueous phase is generally delivered at the branch of the junction perpendicular to droplet flow, while oil is delivered at the branch of the junction parallel to droplet flow. When using microfluidic devices fabricated from hydrophobic materials like PDMS a wetting layer of oil exists

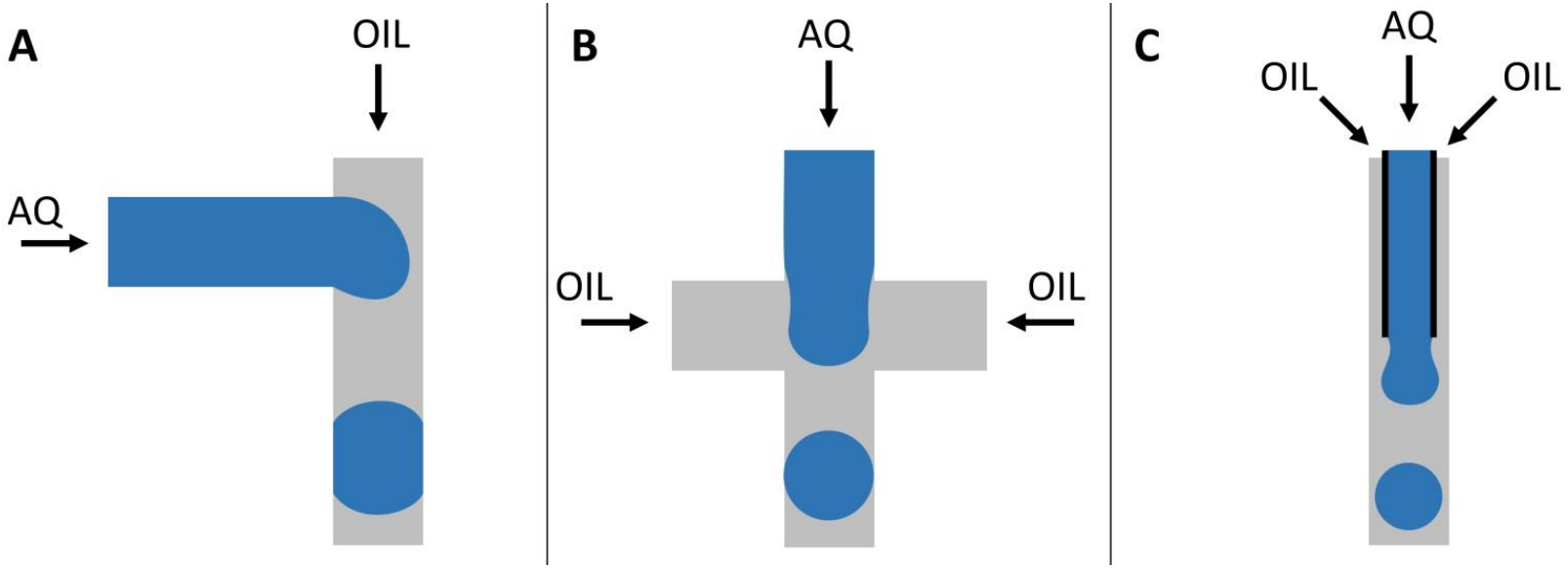

Figure 3: Common methods for droplet formation. (A) Droplets are forged by merging aqueous (AQ) and oil (OIL) streams at a T-junction. (B) Droplets are formed by flow focusing by merging two oil streams with an aqueous stream at a cross junction. (C) Droplets are formed coaxially by inserting tubing into another piece of tubing or channel in a concentric geometry. An aqueous stream is then pumped through the inner tubing while oil is pumped through the outer channel or tubing.

between the aqueous droplet and microfluidic surface. (Tabeling, 2009) This oil layer prevents mixing of adjacent droplets and provides some protection against fouling of the microfluidic device by the sample.

The dynamics of droplet breakup regulate droplet volume, and have been studied extensively. (Garstecki et al., 2006; Baroud et al., 2010) Several forces contribute to droplet breakup. The first is a net Laplace pressure (P_L) oriented in the upstream direction, which grows as the forming droplet elongates and deforms (Figure 4A). This net pressure results from the development of different radii of curvature (R_1 and R_2) for the tip of the forming droplet and back side of the droplet. The difference in the radii of curvature causes differing P_L for the front and rear of the droplet, which results in a net pressure in the upstream direction. The next force which contributes to droplet breakup is caused by shear stress exerted parallel to the aqueous/oil interface by the oil stream. This stress results in a net force, F_γ, parallel to the surface of the droplet in the downstream direction as shown in Figure 4B. The final contributing force involved in droplet breakup in a T-junction results from pressure buildup behind the forming droplet due to constriction of the channel by the forming droplet, as shown in Figure 4C. This pressure buildup exerts a net force, F_R, across the back surface of the droplet in the downstream direction. Geometry of the T-junction effects all three of these forces, and is also an important factor influencing droplet volume.

Capillary number (C_a) is a dimensionless quantity used in fluid dynamics to describe the relative contributions of viscous forces and surface tension to interface formation. Depending on C_a and relative flow rates of the oil and aqueous streams, different factors dominate droplet breakup. For droplet production at a T-junction, this has been found to result in two distinct flow regimes called squeezing and dripping. (Xu et al., 2008) An understanding of the factors contributing to droplet breakup can be used to control droplet volume. Another common methods of droplet formation is called flow focusing (Figure 3B), and is performed by merging two oil streams with

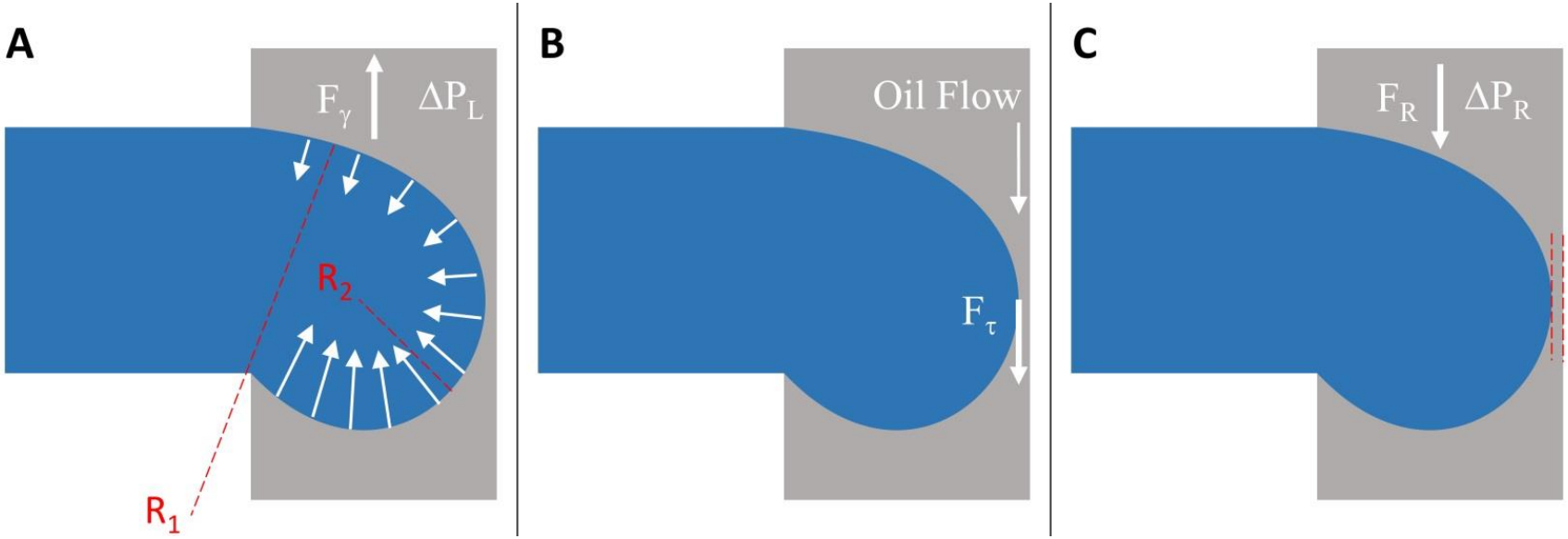

Figure 4: Forces effecting the dynamics of droplet breakup in a T-junction. (A) A net Laplace pressure in the upstream direction due to the development of different radii of curvature for the back side of the droplet and the leading tip. This results in a net force acting on the droplet in the upstream direction. (B) The oil stream exerts shear stress on the phase interface. This causes a net shear force parallel to the droplet surface directed downstream. (C) Constriction of the channel by the forming droplet, as shown by the red dotted lines, results in a pressure drop over the droplet which can be described using Poiseuille's law. This pressure exerts a force on the back surface of the droplet in the downstream direction.

an aqueous stream at a cross junction. (Fu et al., 2012) A less common means of droplet production called co-axial (Figure 3C) involves inserting tubing into a channel in a concentric manner. Oil is pumped through the channel and the aqueous phase is pumped through the tubing. (Baroud et al., 2010) This geometry has been used extensively for the production of double emulsions. (Wang et al., 2014) Each of these geometries has its own distinct flow regimes. Depending on the desired droplet volume and application different geometries may be more convenient to use.

1.3.3 **Droplet Microfluidic Techniques**

A wide variety of techniques for sample handling utilizing microfluidic droplets exist. Additionally, the entirely online nature of most droplet techniques makes them compatible with each other. This makes integration of multiple sequential handling steps into the same device possible. Each droplet can be thought of as a sample aliquot. Reagent addition or dilution is commonly performed at a second T-junctions downstream from the droplet production junction. (Zheng and Ismagilov, 2005) Droplets pass this second T-junction perpendicular to a reagent or diluent stream, as shown in Figure 5A. Some consistent volume of the reagent or diluent is added to the droplet, which then continues on for downstream processing. If the composition of the reagent stream is changed over time a series of droplets with a concentration gradient may be formed. (Zheng et al., 2003) Rapid reagent mixing is aided by advective flow within droplets. Mixing can be enhanced farther by integrating a series of serpentine turns into the microfluidic channel, as shown in Figure 5B. (Song et al., 2003)

Many other sample handling procedures for droplets are described in the literature. Droplet preconcentration has been performed by selective extraction of solvent into the oil phase (Figure 6A). (Ji et al., 2013) Droplet merging has been performed using channel geometry (Figure 6B), (Hung et al., 2006; Bremond et al., 2008) electric fields, (Mazutis et al., 2009) and surface wetting. (Fidalgo et al., 2007) Droplet splitting has been performed using branches in channel geometry (Figure 6C).

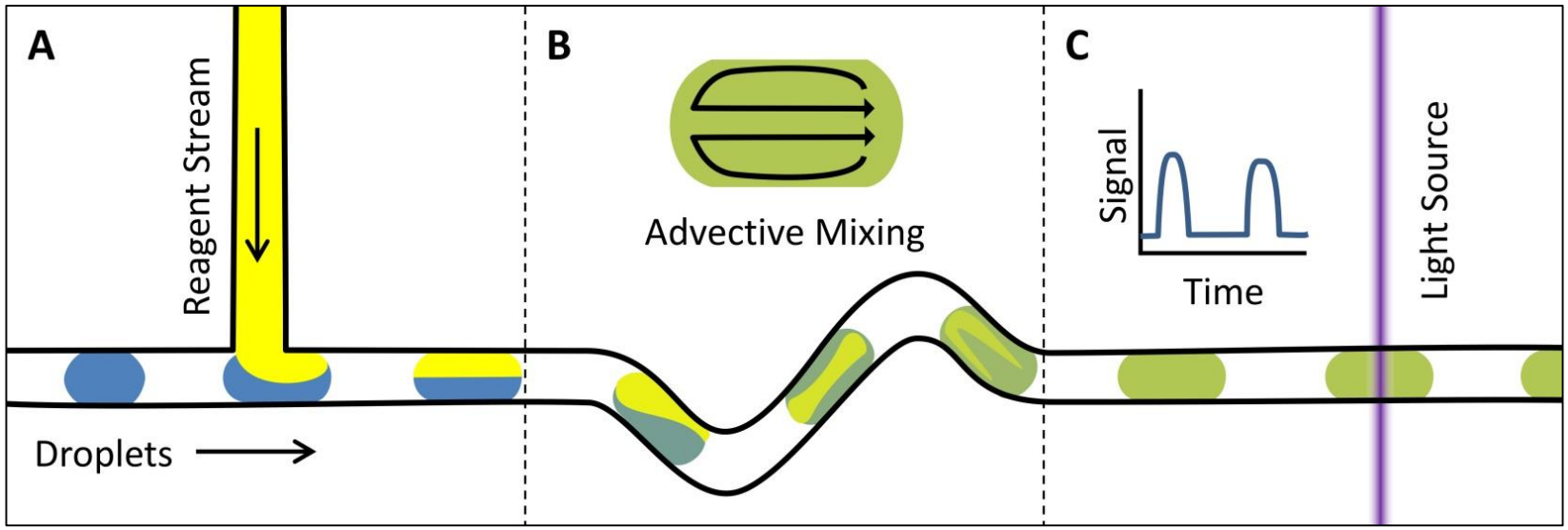

Figure 5: Commonly used techniques for droplet handling and analysis. (A) Reagent is added to a stream of droplets at a T-junction. The amount of reagent added is controlled by changing the reagent stream flow rate. (B) Reagent and sample within droplets is rapidly mixed due to advective mixing which occurs as fluid inside the droplet circulates. Use of serpentine mixing channels accelerates mixing. (C) Droplet detection is commonly performed spectroscopically. A light source, such as an excitation source for LIF detection, is focused through the channel. Signal is detected over time as droplets move in and out of the light source.

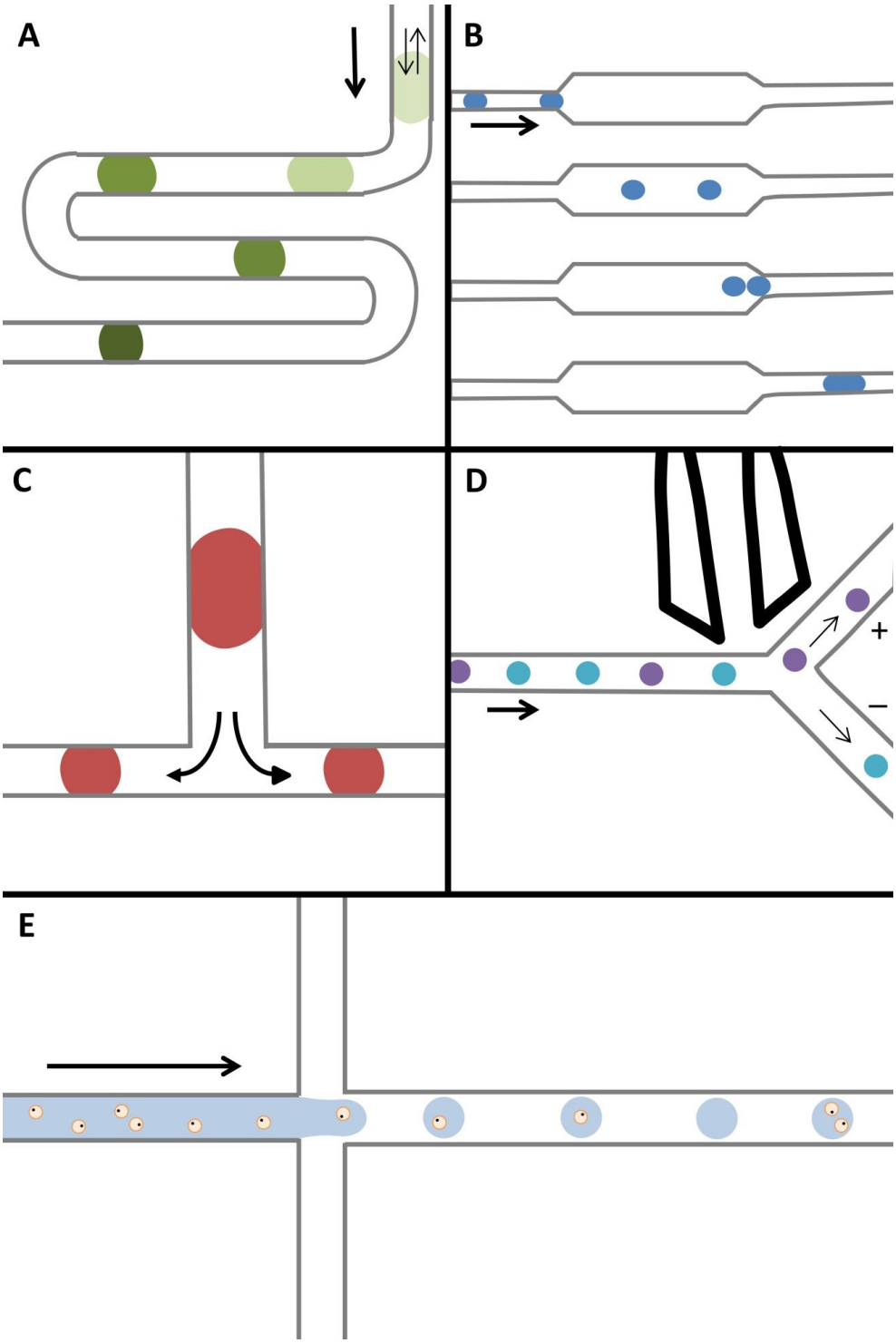

Figure 6: Additional droplet techniques. (A) Droplets are concentrated by extracting solvent into the oil phase, as shown by the small arrows. (Ji et al., 2013) (B) Droplets merge at a geometric constriction in a channel. (Bremond et al., 2008) (C) Droplets are split at a T-junction. (Adamson et al., 2006) (D) Droplets are sorted down different channels using an electric field generated by embedded electrodes (shown in black). (Baret et al., 2009) (E) Single cells, shown in orange, are captured in droplets for single cell analysis. (Joensson and Andersson Svahn, 2012)

(Adamson et al., 2006) Droplet sorting has been achieved using electrical actuation (Figure 6D) (Baret et al., 2009) and magnetic fields. (Ting et al., 2006). Finally, encapsulation of single cells (Figure 6E) for single cell analysis has been widely reported. (Joensson and Andersson Svahn, 2012) Many additional techniques are reported in the literature, but are beyond the scope of this chapter.

The final step in most droplet analysis schemes is usually detection of droplets. To date a wide range of droplet detection methods have been reported. Fluorescence is highly sensitive and is ideal when working with extremely small volumes. (Cole et al., 2015) Other spectroscopic techniques like ultra violet visible (UV-Vis) spectroscopy (Deal and Easley, 2012) have been reported, but are challenging because of low sensitivity associated with extremely small path lengths. Fluorescence and other spectroscopic techniques are generally performed on chip by focusing a light source through the channel. Signal is then collected over time as droplets move in and out of the light source, as seen in Figure 5C. Surface-enhanced Raman spectroscopy has even been reported for use as a spectroscopic detection technique for droplets. (Wu et al., 2014) Another common droplet detection technique is electrospray ionization mass spectrometry (ESI-MS). A large number of different droplet based ESI-MS interfaces have been designed (Kelly et al., 2009; Zhu and Fang, 2010; Ji et al., 2012, 2013; Sun et al., 2012; Smith et al., 2013), but most involve some means of removing oil from the droplet stream prior to moving aqueous sample onto an electrospray emitter. Other droplet detection techniques reported include matrix-assisted laser desorption/ionization MS (MALDI-MS) (Küster et al., 2013), microcoil nuclear magnetic resonance (NMR) spectroscopy (Kautz et al., 2005) and electrochemical techniques such as contactless conductivity. (Cahill et al., 2011) One final droplet technique of note related to detection is the use of droplet microfluidics for signal modulation. Droplets passing a detector at high frequency have recently been demonstrated to be a viable means of optical beam chopping. (Deal and Easley, 2012)

Aside from chemical analysis, droplets have been used extensively as a synthetic tool. Although solvent compatibility is often a concern with traditional microfluidic chips, a related microfluidic droplet

technique termed “digital microfluidics” has been utilized for automating organic reactions. (Shah et al., 2013) In digital microfluidics droplets are moved across an electrode grid using electrowetting. Fluoropolymer insulating layers are typically used between electrodes and liquid droplets, which provides good solvent compatibility for organic reactions. Although digital microfluidic platforms have lower throughput than continuous flow style droplet microfluidic platforms, they allow much more freedom to control the order in which reagent droplets are mixed, merged, and split, thereby providing an extremely valuable level of flexibility in method development. Continuous flow droplet microfluidic platforms, on the other hand, have been demonstrated to be a powerful tool in the synthesis of a wide variety of monodisperse particles. Heterogeneous and homogenous microparticles along with nanocyrstals (Brugarolas et al., 2013; Kim et al., 2014) have been synthesized using droplets. Crystallization of protein solutions for on-chip x-ray diffraction has even been demonstrated using droplet microfluidics. (Zheng et al., 2003; Li and Ismagilov, 2010)

1.4 Selected Analytical Chemistry Applications in Droplet Microfluidics

1.4.1 Microfluidic Rheometry

Rheometry, the measure of fluid flow properties, is perhaps one of the most widely used analytical techniques in manufacturing and engineering. Fluid properties like viscosity arise from intermolecular attractive forces in a sample, and are easily measured using simple flow-based devices. Rheometry is therefore a simple and reliable method for monitoring manufacturing processes (Abuasi et al., 1993) and gaining insight into changes in the molecular structure of a sample. (van Ruymbeke et al., 2014) The rheological properties of a material are also important in engineering and are important to characterize. Rheology is therefore critical to the field of material science.

One of the most common methods traditionally used for rheological characterization of fluids is capillary viscometry. The most widely used capillary viscometer, the common U-Tube viscometer or

"Ostwald" viscometer, uses the time required for a meniscus in a glass tube or capillary to fall under gravimetric flow. This time along with the Hagen-Poiseuille law is then used to determine sample viscosity. The traditional use of simple fluidic systems such as the U-Tube viscometer to measure rheological properties of fluids makes the use of microfluidic chip based systems a logical choice for miniaturizing rheological measurement techniques. For these reasons there have been a large number of microfluidic rheometers reported in the literature. (Srivastava et al., 2005; Lee and Tripathi, 2005; Han et al., 2007; Nguyen et al., 2008; Pipe and McKinley, 2009; Kang et al., 2010; Lan et al., 2010; Schultz and Furst, 2011; Galindo-Rosales et al., 2013; Livak-Dahl et al., 2013; Solomon and Vanapalli, 2014) Surprisingly however, very few droplet-based microfluidic rheometers have been reported, (Schultz and Furst, 2011; Livak-Dahl et al., 2013) making development of new droplet-based techniques for characterizing flow properties especially important. Chapters 2 and 3 describe the development of two droplet-based microfluidic viscometers, and give additional background information on the field of microfluidic rheometry.

1.4.2 **Droplet Content Analysis by Capillary Electrophoresis**

A major drawback when using droplet microfluidic platforms for applications in analytical chemistry is the incompatibility of the oil phase with most separation techniques. For example, CE utilizes strong electric fields to separate analytes in aqueous solution based on their charge and hydrodynamic drag. If the oil phase was injected into a capillary along with the aqueous droplet and a strong electric field was applied, dielectric breakdown of the nonconducting oil phase would immediately occur. Chemical separations play a vital role in quantitative and qualitative analysis, however, especially in bioanalysis where the complex nature of the sample matrix often interferes with other forms of assay. The necessity of separating droplet content for many applications has led to active research in this area, and several injectors have been reported which allow coupling of droplet streams to separation techniques

for analysis of droplet content. (Edgar et al., 2006; Niu et al., 2009; Filla et al., 2011; Wang et al., 2011; Ye et al., 2015)

All of the injectors described in the literature have been designed to analyze droplet content by CE. Aside from being a highly efficient separation technique compatible with small aqueous samples, CE is also easily integrated on microchips because it is controlled using voltages rather than pumps and does not require a stationary phase, making it an ideal separation technique for droplet content analysis. In order to analyze droplet content by CE the oil phase must be removed prior to injection. Two strategies have been developed to accomplish this. The first, termed "desegmentation" (Roman et al., 2008; Filla et al., 2011), utilizes surface patterning on chip to cause droplets to merge at a junction and reform a continuous aqueous stream, as shown in Figure 7A. This stream is then fed to an on-chip CE channel and injected using traditional electrophoretic gating techniques. The other strategy involves directly injecting an aqueous droplet into an electrophoresis buffer stream, as seen in Figure 7B. (Kelly et al., 2009; Zhu and Fang, 2010; Ye et al., 2015) This has been achieved using surface patterning, geometry mediation, and by use of hydrophobic sorbent materials to remove the oil phase. Additional background on analysis of droplet content by CE may be found in Chapter 4, which details a simple injector for analysis of droplet content by CE.

1.5 A Note On Simple Design Principles

Two-phase flow techniques, by their very nature, are more complicated than single phase flow techniques. In the case of droplet microfluidics a number of problems can arise if careful design and operation are not observed. For example, stable droplet motion depends on the maintenance of the oil wetting layer between the droplet and interior surface of the microfluidic device. Any changes to device surface properties which alter wetting can cause droplets to wet the surface and stick. This can in turn

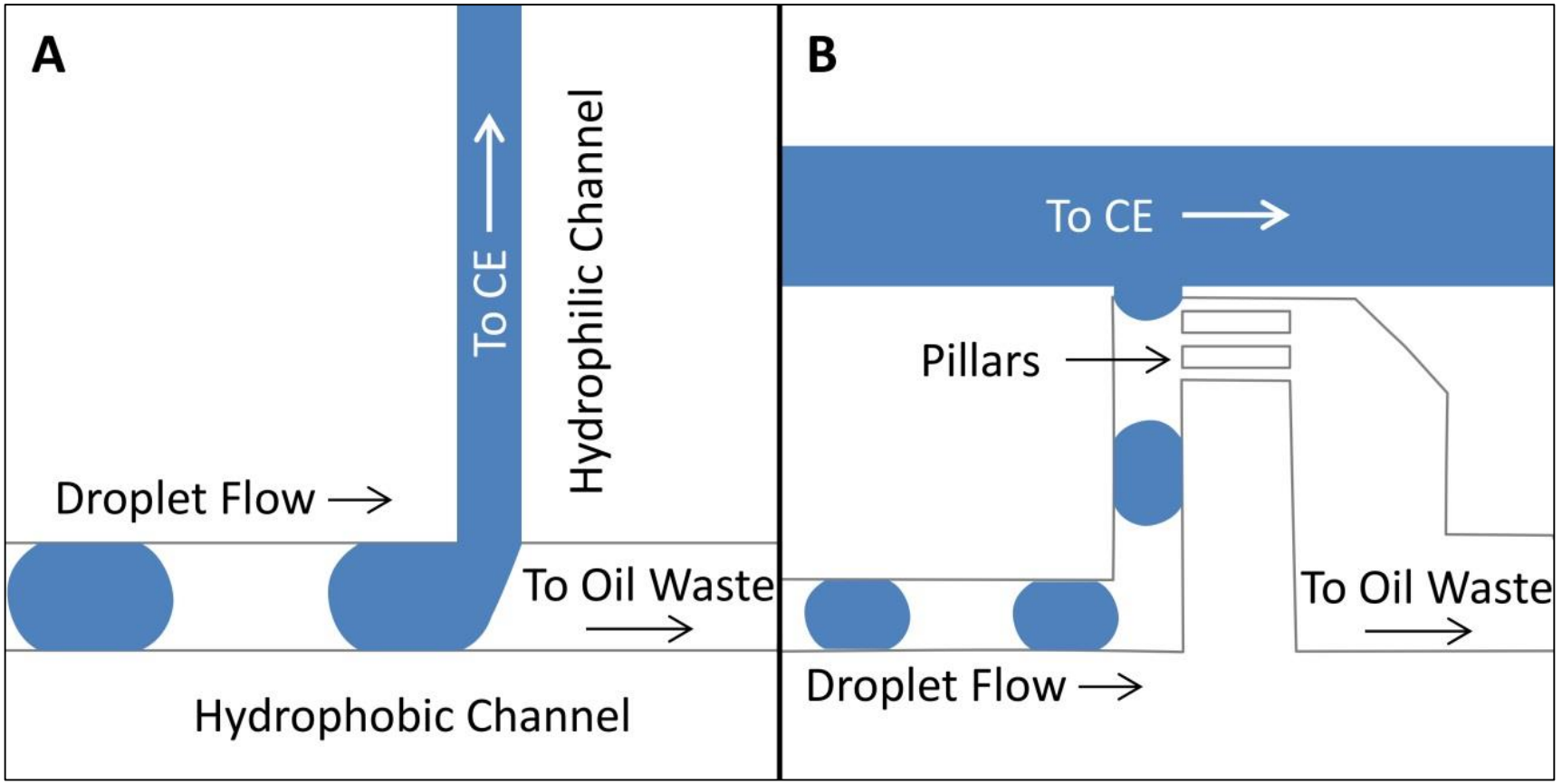

Figure 7: Two common strategies for removing oil prior to droplet analysis by CE. (A) An example of a desegmentation strategy. One branch of a PDMS junction is corona treated, rendering it hydrophilic. This surface patterning causes aqueous droplets to travel up the hydrophilic branch while oil continues on through the hydrophobic channel to a waste reservoir. This technique, termed "desegmentation, reforms a continuous aqueous stream, which can then be injected via electrophoretic gating. (B) An example of direct injection. In this strategy droplets are directly injected into a channel containing a buffer stream. An electric field is then applied over this channel to begin separation by CE. In the example shown here, several hydrophobic pillars are used to direct droplets into the buffer channel while moving oil, which can wet the surface of these pillars and flow around them, to waste. No surface patterning is required for this strategy.

cause problems with droplet merging and irregular flow. Often it is necessary to ensure a uniform homogenous surface by surface treatment of the device prior to use, and samples containing components which adsorb to surfaces such as proteins or surfactants require special consideration prior to use. Another problem common in droplet platforms involves the tendency of droplets to stall out and merge with subsequent droplets at locations where channel geometry constricts. This is particularly problematic at fluidic connections where square channels are interfaced with cylindrical tubing for moving droplets off chip. A final common problem with droplet platforms is the need for extremely stable flow. Droplet frequency and volume are both sensitive to changes in flow rate. This is an issue when pump output fluctuates over time.

Droplet microfluidics has enjoyed remarkable success in academic research labs, but widespread adoption for practical applications in industrial, environmental, and medical laboratories the way CFA was adopted has been slow. Perhaps the largest barriers to widespread use of microfluidic droplet platforms outside of academia are problems with the robustness and ruggedness of many droplet techniques. Working with micro-scale systems already presents many technical challenges, and the extra layer of complexity present when working with two-phase flow systems adds to reliability problems stemming from complicated design. In order for droplet microfluidics to achieve wider success it is especially important for new designs to be built as simply as possible. Adopting simple design principles such as utilizing simple geometries, fewer moving parts, and passive control mechanisms will likely play a key role in making droplet microfluidic platforms reliable enough for practical applications.

1.6 Thesis Structure

The focus of this thesis centers on using simple design principles to develop and characterize new reliable tools for use with droplet microfluidics. Chapter 2 describes a simple droplet based viscometer consisting of only a single microfluidic T-junction which uses the aqueous-to-oil phase flow rate ratio for

determination of viscosity. The theory behind operation of the device is presented, along with a series of experiments designed to validate theoretical arguments made. Analytical performance is characterized, and the device is demonstrated by measuring the viscosity of several samples including aqueous, nonaqueous, and aqueous biological samples. The ability to measure the fluorescence of droplets and simultaneously determine sample viscosity from the fluorescence signal is also demonstrated.

Chapter 3 builds on the work presented in Chapter 2 by presenting a modified T-junction based droplet viscometer. A theoretical foundation for using droplet frequency, rather than the phase flow ratio, for determination of aqueous phase viscosity is presented. A series of experiments designed to validate theoretical arguments made are detailed and the analytical performance of the device is also characterized. The complementary nature of the two viscometers from Chapters 2 and 3 is discussed, and strengths and weaknesses of each are highlighted. Several experiments designed to demonstrate the strengths of the new device are presented including the determination of sample viscosity from a fluorescence trace of droplets obtained after adding reagent with a reagent addition T-junction, as well as the use of fluorinated surfactants in the oil phase to make the viscometer compatible with concentrated aqueous protein solutions.

Chapter 4 describes a simple injector designed to deliver aqueous droplets to a capillary for separation by CE while excluding the oil phase. Analytical performance of the injector is characterized and practical application of the injector is demonstrated by using it to form a calibration curve for assay of riboflavin. Qualitative identification of riboflavin in samples of human urine is also performed as a demonstration of device compatibility with biological samples. A simple means of injecting droplets on demand by hand is also described and used to perform injections reliably.

Chapter 5 details future areas of research relating to the microfluidic droplet viscometers presented in Chapters 2 and 3 and the microfluidic droplet injector presented in Chapter 4. A preliminary

experiment involving use of the viscometer presented in Chapter 2 for analysis of a non-Newtonian fluid at variable flow rate is presented. A scaled up version of the microfluidic injector described in Chapter 4 is also presented which is built entirely by hand rather than with photolithography, which would not be possible were it not for the simple design principles used.

2. Development of a Simple Droplet-Based Microfluidic Capillary Viscometer for Low-Viscosity Newtonian Fluids

2.1 Introduction

Viscosity is an important macroscopic physical property that has been used extensively for gaining insight into the behavior of systems on the molecular level. Because it is easily measured, viscosity is routinely used in many disciplines including proteomics (where a protein solution's viscosity is related to protein hydrodynamic radius), (Richards, 1993) medicine (where elevated blood viscosity is a known risk factor for cardiovascular disease), (Jeong et al., 2010) and the food and beverage industry (for its relevance to product mouthfeel) (Stokes et al., 2013) as well as in a wide range of other fields. Current trends in utilizing microfluidics to miniaturize laboratory instrumentation, which aim to decrease reagent and sample consumption, reduce instrument footprint, allow for easy automation, and enhance heat and mass transfer, have necessitated either the scaling-down of existing measurement techniques or the development of new small-scale measurement techniques. This has driven development of miniaturized viscometers, with a number of microfluidic viscometer designs recently reported in the literature. (Lee and Tripathi, 2005; Srivastava and Burns, 2006; Han et al., 2007; Teh et al., 2008; Banpurkar et al., 2009; Pipe and McKinley, 2009; Kang et al., 2010; Lan et al., 2010; Nelson et al., 2011; Galindo-Rosales et al., 2013; Solomon and Vanapalli, 2014)

One of the largest selling points of microfluidic platforms is their ability to easily integrate multiple sample preparation and measurement techniques into a single device for comprehensive sample processing and analysis. To take advantage of this feature, it has become increasingly important to develop microfluidic techniques with multiple functions, as with droplet microfluidics. Droplet microfluidics aliquots aqueous samples by forming droplets of sample in an immiscible carrier fluid. These droplets can be used for a wide range of common laboratory sample-handling and measurement procedures such as reagent addition, dilution, and spectroscopic analysis. (Teh et al., 2008) Despite this, most microfluidic rheometers previously reported involve entire platforms dedicated exclusively to the measurement of viscosity without the possibility of additional chemical analysis of samples. The use of droplet microfluidics for determination of viscosity would allow a sample's rheological properties to be determined while simultaneously performing a wide range of other preparations and measurements on the sample.

However, surprisingly few droplet-based rheometers have been reported. One reported device utilized multiple particle tracking (MPT) microrheology in conjunction with a droplet train containing a concentration gradient to probe viscosity as a function of concentration. (Schultz and Furst, 2011) Although this device conveniently allows viscosity to be measured as a function of sample composition, limitations are placed on the droplet size because of the need to limit hindrance of the mobility of probe particles by droplet boundaries. Large (3.5 μL) droplets were required to limit hindrance. Additionally, the technique requires droplet motion to be stopped while passive measurements are made, which could inhibit the ability to simultaneously perform other manipulations and measurements on droplets. Lastly, although most viscometers allow for an additive-free measurement, the use of MPT requires fluorescent particles to be added to samples.

The only other droplet rheometer found in the literature measures the velocity of a 30 nL sample droplet flowing through a constriction in a microfluidic channel by tracking the oil/aqueous phase

interface of the droplet with video microscopy and uses velocity to calculate droplet viscosity. (Livak-Dahl et al., 2013) The measurement is nondestructive and could allow for subsequent analysis of droplet content. Spectroscopic or electrochemical techniques could even be used to simultaneously measure droplet velocity and chemical content, but the device requires architecture not typically used in other droplet microfluidic platforms including a long constriction channel. It also requires a precise off-chip pressure control system. The ideal droplet viscometer would allow viscosity measurement without the addition of features not already included in most droplet platforms, which could allow for a more seamless addition of viscometric capabilities to existing droplet platforms.

In this chapter, the development of a droplet-based microfluidic capillary viscometer is reported that encodes information about sample viscosity in the spacing of droplets in a droplet train. The device is capable of processing samples down to 38 nL and can perform measurements on aqueous and nonaqueous liquids. The design requires only a basic T junction, a common means of droplet formation already included in many droplet platforms, which could allow it to be easily incorporated into existing droplet platforms. Furthermore, the ability to measure viscosity using both microscopic imaging and an off-chip fluorescence detector is demonstrated, which could allow for simultaneous determination of sample viscosity and spectroscopic analysis of the sample. Lastly, it is demonstrated that viscosity measurement is unaffected by the pressure applied to move fluids through the device when working with Newtonian fluids, which makes precise control over pressures and flow rates unnecessary for Newtonian samples.

2.2 Theoretical

2.2.1 Calibration

During droplet formation in a microfluidic T junction with cylindrical channels (Figure 8A), assuming laminar flow, fluids flowing through the aqueous and oil inlet channels of the junction obey Poiseuille's law, represented as

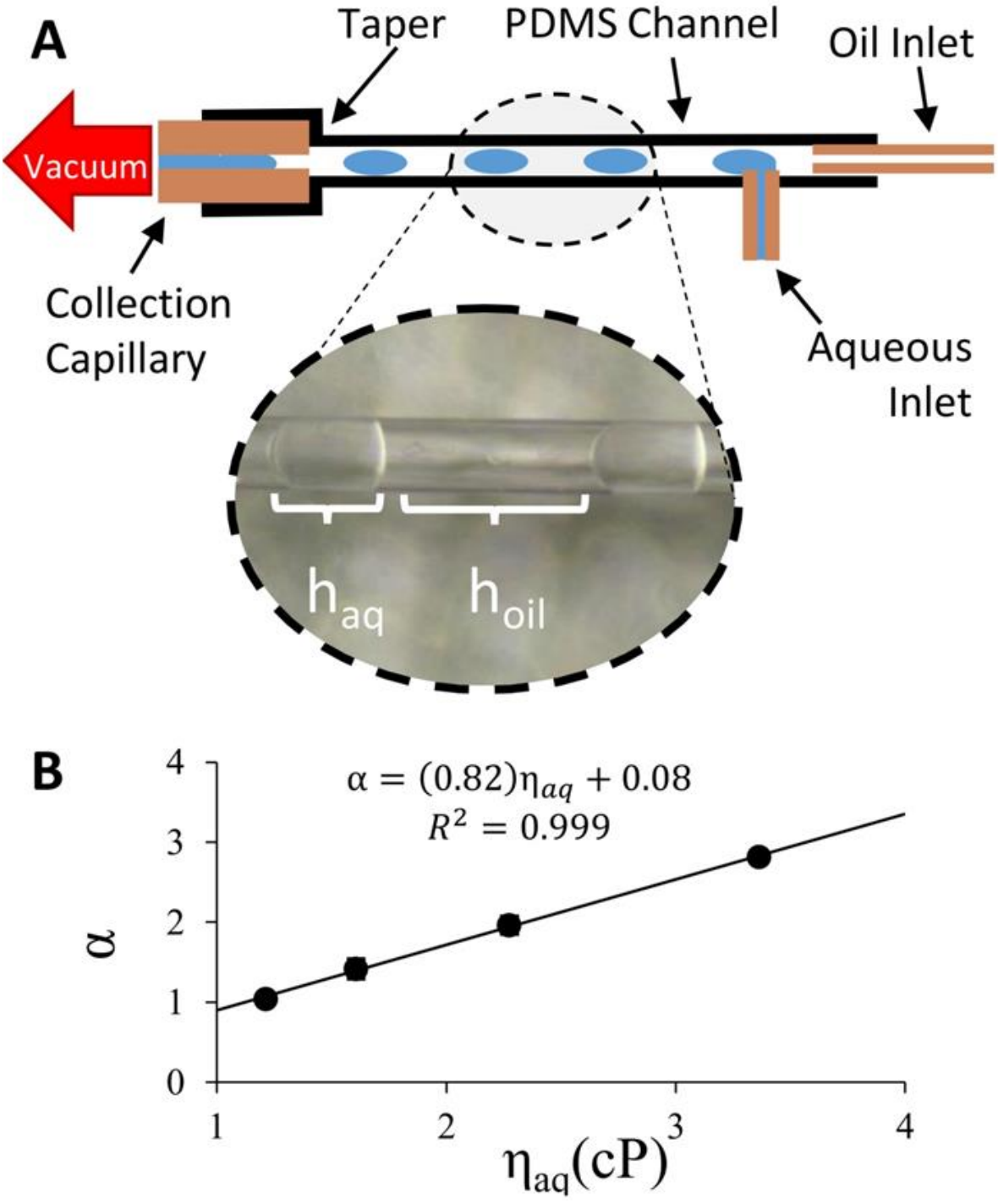

Figure 8: (A) Aqueous sample is withdrawn through a microfluidic viscometer consisting of a PDMS microfluidic T-junction connected to a PFD inlet capillary (oil inlet) and aqueous sample capillary (sample inlet) with known lengths, l, and radii, R, to form droplets of sample in the oil stream. The droplets are then imaged and the heights of the aqueous and oil phase (h_{aq} and h_{oil}) are measured from micrographs. The ratio h_{oil}/h_{aq}, defined as α, is linearly proportional to aqueous viscosity. (B) A device calibration curve constructed using a series of glycerol viscosity standards. Points are the average of 5 measurements. Error bars are included but are covered by the data points.

$$\Phi = \frac{\pi R^4 |\Delta P|}{8\eta l} \tag{2.1}$$

where Φ is the volumetric flow rate of the fluid, R is the radius of the inlet, ΔP is the pressure drop over the inlet, η is the viscosity of the fluid flowing through the inlet, and l is the length of the inlet. Because droplets form at the junction space where the two immiscible fluids merge, the ratio in flow rates of the two phases, defined as α, must equal the ratio of the volume of oil phase between droplets (V_{oil}) to that of the aqueous phase within droplets (V_{aq}). If an aqueous droplet and oil segment are both assumed to be cylindrical with radii equal to the channel radius, then α is also equal to the ratio of cylinder heights, h_{oil} and h_{aq}.

$$\alpha = \frac{\Phi_{oil}}{\Phi_{aq}} = \frac{V_{oil}}{V_{aq}} = \frac{h_{oil}}{h_{aq}} \tag{2.2}$$

Substituting the variables from eq 2.1 into eq 2.2 in place of flow rates provides an equation relating α to the physical dimensions of the inlets, the pressure drops over the two inlets, and the viscosities of the aqueous and oil phases.

$$\alpha = \left(\frac{R_{oil}}{R_{aq}}\right)^4 \left(\frac{|\Delta P_{oil}|}{|\Delta P_{aq}|}\right) \left(\frac{\eta_{aq}}{\eta_{oil}}\right) \left(\frac{l_{aq}}{l_{oil}}\right) \tag{2.3}$$

The device used in this chapter uses a vacuum to apply negative pressure at the T junction outlet, pulling each fluid through the device. Because both inlets open up to the room and terminate at the same location in the junction, their inlet and outlet pressures must be equal. This means the total pressure drop across both inlet capillaries must be equal, as represented by

$$\Delta P_{oil} = \Delta P_{aq} = P_{room} - P_{junction} \tag{2.4}$$

where P_{room} is the room pressure and $P_{junction}$ is the pressure at the location on chip where the two immiscible streams merge.

A model for droplet breakup by Garstecki et al. (Garstecki et al., 2006) considers the pressure drop across the forming droplet interface caused by other factors, including a net P_L in the upstream

direction that develops as the droplet interface is deformed. Assuming ΔP_{aq} and ΔP_{oil} are very large compared with the pressure drops resulting from P_L, should be negligible and the pressure terms in eq 2.3 should cancel. This should be true at high flow rates because ΔP_{aq} and ΔP_{oil} increase with flow rate, whereas P_L depends only on the curvature of the forming droplet interface and the surface tension and should be relatively constant. This results in eq 2.5, represented as

$$\alpha = \left(\frac{R_{oil}}{R_{aq}}\right)^4 \left(\frac{\eta_{aq}}{\eta_{oil}}\right)\left(\frac{l_{aq}}{l_{oil}}\right) \tag{2.5}$$

If the physical dimensions of the device are constant and the same oil phase is used with aqueous phases of varying viscosity, then the parameters that remain constant can be combined into one term, m, and a linear relationship between α and η_{aq} is evident, where *m* is the slope.

$$m = \left(\frac{R_{oil}}{R_{aq}}\right)^4 \left(\frac{1}{\eta_{oil}}\right)\left(\frac{l_{aq}}{l_{oil}}\right) \tag{2.6}$$

$$\alpha = m\eta_{aq} \tag{2.7}$$

By measuring h_{oil} and h_{aq} experimentally, α may be calculated for aqueous viscosity standards and plotted versus η_{aq}. The resulting calibration may be used for determination of aqueous samples with unknown viscosities. Because ΔP_{aq} and ΔP_{oil} do not appear in eq 2.6, there is no need to precisely control or measure driving pressures. Similarly, because only the ratio Φ_{oil}/Φ_{aq} and not the absolute flow rates must be known, there is no need for precise control or measurement of flow rate when using Newtonian fluids. Equations derived for use with rectangular channels, which are more commonly used than cylindrical channels, may be found in the Appendix B.

Single-point calibration is also possible and may be performed by taking the ratio of α values for an aqueous sample, α_{sample}, and an aqueous standard, $\alpha_{standard}$, then substituting the expressions of α in terms of device dimensions (R_{oil}, $R_{aq,}$ l_{aq}, and l_{oil}) and fluid viscosities (η_{aq} and η_{oil}) into the ratio.

$$\frac{\alpha_{sample}}{\alpha_{standard}} = \frac{\left[\left(\frac{R_{oil}}{R_{aq}}\right)^4 \left(\frac{\eta_{aq}}{\eta_{oil}}\right)\left(\frac{l_{aq}}{l_{oil}}\right)\right]_{sample}}{\left[\left(\frac{R_{oil}}{R_{aq}}\right)^4 \left(\frac{\eta_{aq}}{\eta_{oil}}\right)\left(\frac{l_{aq}}{l_{oil}}\right)\right]_{standard}} \quad 2.8$$

Assuming the same device and oil phase are used for all measurements, R_{oil}, R_{aq}, l_{oil}, η_{oil} and l_{aq} are the same for the sample and standard, and all terms cancel except for the aqueous phase viscosities to give

$$\frac{\alpha_{sample}}{\alpha_{standard}} = \frac{\eta_{sample}}{\eta_{standard}} \quad 2.9$$

where η_{sample} and $\eta_{standard}$ are the viscosities of the aqueous sample and aqueous standard respectively. Assuming $\eta_{standard}$ is known, η_{sample} may be calculated using eq 2.9. This saves time by avoiding a multiple point calibration.

2.2.2 **Determination of Oil Phase Viscosity**

Many samples of interest are nonaqueous, which makes determination of the oil phase viscosity important. If the same device is used to measure α for two different oil phases, oil phases 1 and 2 with viscosities $\eta_{oil,1}$ and $\eta_{oil,2}$, respectively, and the same aqueous phase is used, then R_{oil}, R_{aq}, l_{oil}, η_{aq}, and l_{aq} are constant. Taking the ratio of the α values for oil phases 1 and 2 and substituting eq 2.5 into the ratio therefore yields

$$\frac{\alpha_1}{\alpha_2} = \frac{\left(\frac{R_{oil}}{R_{aq}}\right)^4 \left(\frac{\eta_{aq}}{\eta_{oil,1}}\right)\left(\frac{l_{aq}}{l_{oil}}\right)}{\left(\frac{R_{oil}}{R_{aq}}\right)^4 \left(\frac{\eta_{aq}}{\eta_{oil,2}}\right)\left(\frac{l_{aq}}{l_{oil}}\right)} = \frac{\eta_{oil,2}}{\eta_{oil,1}} \quad (2.10)$$

where α_1 and α_2 are the measured phase ratios for oil phases 1 and 2, respectively. Assuming one oil phase viscosity is known, the second may be calculated.

2.2.3 **Measuring and Controlling Shear Rates**

Determining the $\dot{\gamma}$ of a Newtonian fluid moving through a cylindrical tube requires knowledge of the flow rate and radius of the tube and is determined using the following equation.

$$\dot{\gamma} = \frac{4\Phi}{\pi R^3} \tag{2.11}$$

To determine $\dot{\gamma}$ for an aqueous sample, the radius of the aqueous inlet capillary may be used along with the flow rate of the aqueous phase. Aqueous flow rate is easily determined using the volume per droplet (V_{aq}) and droplet generation frequency in droplets per second (*f*) as follows.

$$\Phi_{aq} = (V_{aq})(f) \tag{2.12}$$

Droplet volume and frequency are both affected by flow rate. Controlling $\dot{\gamma}$ by changing flow rate would therefore appear complicated because $\dot{\gamma}$ is in turn related to V_{aq} and f. By substituting eq 2.1 into eq 2.11 and solving for $\dot{\gamma}$, however, the following relationship can be shown.

$$\dot{\gamma} = \frac{R|\Delta P|}{2\eta l} \tag{2.13}$$

This implies that at constant R, η, and l and assuming $P_L \ll \Delta P$ the value of $\dot{\gamma}$ depends linearly on ΔP and should be independent of *f* and V_{aq}. The reason *f* and V_{aq} do not appear in eq 2.13 is the interdependence of *f* and V_{aq}. At a given flow rate, if V_{aq} were increased (for instance by changing the dimensions of the junction space), then *f* would decrease, causing Φ, and therefore $\dot{\gamma}$, to remain constant.

2.3 **Materials and Methods**

2.3.1 **Chemicals**

Adult bovine serum, Sigmacote, 95.5% glycerol, 95% PFD, and 97% trichloro(1H,1H,2H,2H-perfluorooctyl)silane (TCPFOS) were purchased from Sigma-Aldrich (St. Louis, Mo). Sylgard 184 was purchased from Dow Chemical (Midland, MI). Riboflavin was purchased from Acros Organics (New

Jersey). Baby oil was purchased from Walgreens (Deerfield, IL). S3, N4, S6, and N10 white mineral oil reference standards were purchased from SCP Science (Baie-D'Urfé, Quebec). All fused-silica capillaries were purchased from Molex (Phoenix, AZ). Mr. Boston crème de menthe was purchased from Boston Distiller (Owensboro, KY). Water used to prepare all solutions was ultrafiltered with a Millipore Synergy 185 (Billerica, MA) water filtration system.

2.3.2 **Device Construction**

Polydimethylsiloxane (PDMS) T junctions with 150 μm diameter cylindrical channels (Figure 8A) were constructed using a capillary molding technique similar to one reported by Burgoyne et al. (Burgoyne et al., 2010) that was based on encasing capillaries in PDMS and then removing them to leave behind cylindrical channels. A 150/20 μm outer diameter (o.d.) /inner diameter (i.d.) capillary was installed in the plane of the channel at the perpendicular branch of the T junction as an aqueous sample inlet. A 150/50 μm o.d./i.d. capillary was installed at the main channel of the T junction as an oil inlet. One end of the main channel was designed with a taper to allow a 5.5 cm length of 360/75 μm o.d./I.d. capillary (collection capillary) to be installed at the remaining branch of the T junction. Aqueous and oil inlet capillaries had varying lengths depending on the experiment. More details about junction construction and capillary molding can be found in Appendix B.

2.3.3 **Droplet Generation and Measurement**

Droplets were formed from aqueous samples by placing the tip of the aqueous inlet capillary into a vial containing the sample and placing the tip of the oil inlet capillary in a vial of oil. The collection capillary was connected to a side-arm flask using a rubber stopper and tygon tubing to prevent oil from aspirating into the vacuum pump. The arm of the flask was then connected to a Welch 2034 DRYFAST vacuum pump (Welch-Ilmvac, Niles, IL) through a regulator (Squire-Cogswell, Gurnee, IL) and digital pressure gauge (Vacuubrand DVR 2, Wertheim, Germany). Vacuum was applied to pull sample and oil

phase through their respective inlets. Vacuum pressure was adjusted until droplet frequency was between 0.1 and 1 Hz, and flow was allowed to equilibrate for 3 min prior to recording data.

Droplet dimensions (h_{oil} and h_{aq}) were measured from microscope images of droplets either on chip or in the collection capillary during droplet formation using a Nikon SMZ660 stereoscopic dissection microscope interfaced with an AmScope MD35 USB microscope camera (Figure 8A). The average of five measurements was taken for all measurements. Images were loaded into AmScope ToupView, an image-processing program with a measurement tool suite, where droplet dimensions were measured in pixels. These dimensions were then used to determine α. Droplet volume was estimated by assuming droplets were cylindrical in shape and using the width of the channel as a scale bar to determine droplet dimensions in micrometers. The temperature of the room was measured during droplet formation using a thermocouple and Protek 506 digital multimeter so temperature correction to viscosities could be applied.

2.3.4 **Viscosity Corrections for Temperature**

To account for viscosity changes because of daily variations in room temperature regression analysis of viscosity/temperature data available in the literature was carried out for all fluids. More details are provided in Appendix B.

2.3.5 **Calibration and Reproducibility**

A series of four aqueous glycerol solutions with concentrations between 10 and 40% (wt/wt %) were run through the device with PFD to determine α for each solution, which was plotted versus solution viscosity in Microsoft Excel to form a calibration curve. Because the collection capillary has a smaller diameter than the PDMS channel, droplets become elongated in it, which improves precision of droplet height measurements. Droplet merging and bubble formation were sometimes problematic at the PDMS/collection capillary interconnect, so measurement of droplets on chip was more convenient than on capillary. Measurement of droplets on chip also allowed a wider range of α values to be measured

within the field of view of the microscope. To test optimal device reproducibility, three separate devices with 30 cm oil inlets and 10 cm aqueous inlets were constructed, and each device was calibrated three times on the same day by measuring droplet dimensions on capillary. For convenience, all other experiments used droplet measurements carried out on chip.

2.3.6 **Theoretical Validation**

The uncertainty of all measured slopes was determined using the LINEST function of Microsoft Excel. To validate the theoretical prediction that α, and therefore m, is independent of the applied vacuum pressure for Newtonian fluids, calibrations were carried out at varying vacuum pressures. Glycerol standards (67, 50, and 30 wt/wt %) were used with PFD and a device with a 4 cm aqueous inlet and 30 cm oil inlet. Flow was allowed to stabilize for 3 min between pressure adjustments.

On the basis of eq 2.6, m, and therefore sensitivity, can be controlled by changing the physical dimensions of the device (R_{oil}, R_{aq}, l_{aq}, and l_{oil}) or by changing composition of the oil phase to alter η_{oil}. To validate the theory, both l_{oil} and l_{aq} were varied to demonstrate the effect on *m.* To vary l_{oil}, successive calibrations were carried out using glycerol standards (10–40 wt/wt %), PFD, and a 30 cm oil inlet with a 10 cm aqueous inlet. One centimeter was cut from the oil inlet between each successive calibration. Aqueous inlet length was varied similarly by calibrating with a 10 cm aqueous inlet and a 30 cm oil inlet followed by successive calibrations with decreasing aqueous inlet lengths.

Oil phase viscosity was also varied to demonstrate the effect on *m* as predicted by the theory. To achieve this, a device with a 35 cm oil inlet and a 4 cm aqueous inlet was used to perform four calibrations, each using glycerol solutions between 10 and 75% and different oil phases. The four oil

phases used were S3, N4, S6, and N10 white mineral oil reference standards with viscosities of 3.7, 5.6, 8.7, and 18 cP (at 20 °C), respectively.

2.3.7 **Characterization of Working Ranges**

To determine the aqueous viscosity working range, a device with a 4 cm aqueous inlet and a 30 cm oil inlet was tested with 0–80% aqueous glycerol solutions using each of the four white mineral oil standards (S3, N4, S6, and N10) as oil phases. This allowed determination of working range at various oil phase viscosities.

To test the operating ranges for aqueous $\dot{\gamma}$, glycerol solutions with concentrations between 0 and 70% were tested using PFD at variable flow rates. This was achieved by forming droplets of each solution at the maximum vacuum pressure. Pressure was incrementally lowered until droplet formation stalled, and $\dot{\gamma}$ was measured at each pressure.

2.3.8 **Analysis of Crème de Menthe and Baby Oil**

To demonstrate a practical application of the device, the viscosity of a crème de menthe peppermint liquor was determined using a one-point calibration with a 40% glycerol reference solution. A device with a 30 cm oil inlet and a 10 cm aqueous inlet was used along with PFD. The viscosity of baby oil was also determined using a 30 cm oil inlet, a 5 cm aqueous inlet, 67% glycerol as the aqueous phase, and S10 white mineral oil standard as the reference oil. To verify accuracy, viscosity of the crème de menthe and baby oil were also determined using a size 100 U-tube viscometer.

2.3.9 **Viscosity Determination of Human Urine and Bovine Serum**

The viscosities of human urine and bovine serum were determined using one-point calibration. A device with a 10 cm aqueous inlet and a 30 cm oil inlet, a PFD oil phase, and water as the reference standard was used for measurement of human urine and bovine serum. First morning urine was collected

from a human male and refrigerated until analysis the same day. Prior to urine analysis, the PDMS channels were fluorinated by plasma treating them for 2–3 s with an Electro-Technic BD-20 Corona Treater then placing the oil inlet capillary into a vial of TCPFOS. The aqueous inlet was left open to the air and vacuum was turned on to aspirate the TCPFOS through the junction for 1 min. The oil inlet capillary was then placed in a vial of PFD for 30 min to rinse excess TCPFOS from the device.

2.3.10 Use of an Off-Chip Fluorescence Detector for Viscosity Determination

To demonstrate that α can be determined using an off-chip fluorescence detector, the polyimide coating of the collection capillary was burned off over a 5 mm region to form a detection window. The collection capillary was then attached to a Picometrics Zetalif LED 480 fluorescence detector ($\lambda_{excitation}$ = 480 nm). A 5 cm aqueous inlet and a 30 cm oil inlet were used, along with PFD and a series of glycerol standards (60, 50, and 40%) containing 18.9, 22.4, and 26.3 μM riboflavin respectively ($\lambda_{excitation}$ = 447 nm, $\lambda_{emission}$ = 564 nm) (Drössler et al., 2002) to perform a calibration. A fluorescence trace of droplets moving past the detector window was collected during the calibration and used to determine α by taking the area under the baseline-adjusted fluorescence trace and dividing it by the area above the fluorescence trace.

2.4 Results and Discussion

2.4.1 Calibration Performance

Device performance was evaluated by calibrating three separate devices three times each at 1.5 h intervals. Figure 8B shows an example calibration curve. In general, calibrations were very stable and linear, exhibiting only a 0.6% drift in *m* between calibrations, with an average coefficient of linearity of 0.999. Variation between different devices was relatively small as long as they were made from the same capillary rolls, with only a 2% RSD in *m* from device to device. Each four-point calibration took roughly 20 min, but the majority of this time was spent performing manual measurement of droplet dimensions.

Future designs could utilize automated image-analysis algorithms and real-time data processing to allow measurement speed limited only by droplet generation frequency. If photolithography techniques with more exact engineering tolerances were used for construction of devices, then it is even possible that viscosity could be calculated using theory alone, as other groups have achieved, (Livak-Dahl et al., 2013) which would make calibration unnecessary. A waiting period of 80 s between samples was also required to ensure the aqueous inlet capillary had completely filled with the next sample. This waiting period could be reduced by increasing the aqueous flow rate or decreasing the aqueous inlet length.

2.4.2 **Theoretical Validation**

A significant advantage of our device is the independence of *m* from ΔP as predicted by eqs 2.4–2.6, which makes it unnecessary to precisely control or measure pressures on chip. To verify this independence, calibrations carried out at different pressures were used to construct a plot of *m* versus applied vacuum pressure (P_{vac}), as shown in Figure 9A. The plot is essentially a horizontal line with a correlation coefficient of 0.13, which indicates no significant correlation between *m* and vacuum pressure. This is consistent with the theory and lends convincing evidence to its validity.

Using eq 2.6, it can be seen that m, and therefore sensitivity, should be linearly proportional to η_{oil}^{-1}. This is consistent with Figure 9B, which shows a plot of experimentally determined values of *m* versus η_{oil}^{-1} constructed using the series of calibrations carried out with four different white mineral oil viscosity standards. A fit of the experimental data shows a highly linear relationship ($R^2 = 0.998$), which strongly supports the theory. Experimentally determined slopes also fit within a calculated 95% confidence region bound by the dotted lines. This region was determined using eq 2.6 and the partial derivatives method for propagation of uncertainty to account for uncertainty in R_{oil}, R_{aq}, l_{oil}, l_{aq}, and η_{oil}.

Because rolls of capillaries have different beginning and ending radii, there is a large uncertainty in radius if the capillary is cut from the center of the roll. This, in conjunction with the fact that the radii

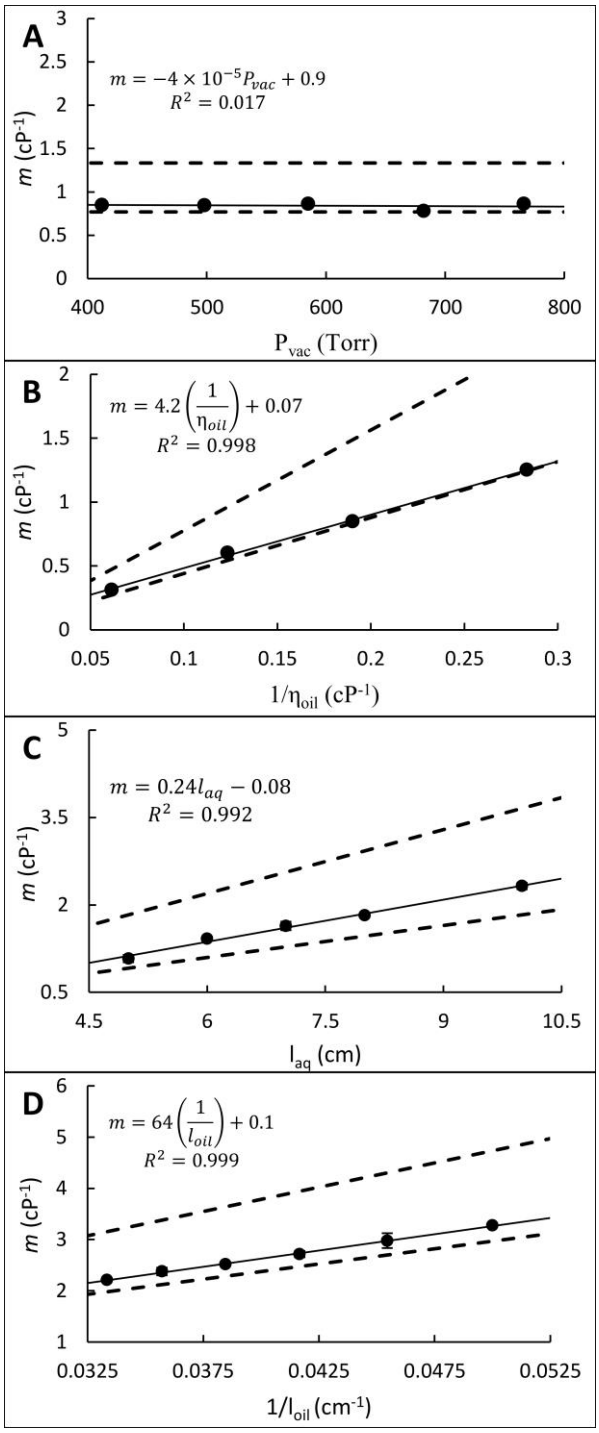

Figure 9: Theory was validated by experimentally verifying the relationship between calibration slope and several variables in eq 6. (A) Slope was found to be independent of the vacuum pressure used to drive flow. (B) Slope was found to be linearly proportional to the inverse of the oil viscosity. (C) Slope was found to be linearly proportional to the length of the aqueous inlet. (D) Slope was found to be linearly proportional to the inverse of the oil inlet length. All slopes were found to be within a calculated 95% confidence region (shown by the dotted lines) calculated using eq 6 and the partial differential method for propagation of uncertainty. Each data point represents a single measured slope.

terms are raised to the fourth power, leads to a large uncertainty in the calculated slope and therefore a large 95% confidence region. Despite the large uncertainty in inlet radii variation between devices was small provided that inlets for different devices were cut from the same part of the same roll.

Linear relationships are similarly predicted between *m* and l_{aq} and between *m* and l_{oil}^{-1} by eq 6. The linear fit of a plot of experimental slopes measured at varying aqueous inlet lengths (Figure 9C) and linear fit of experimental slopes measured at varying oil inlet lengths (Figure 9D) are 0.992 and 0.999, respectively, which indicates highly linear relationships as predicted by the theory. The data points also fit within a 95% confidence regions calculated similarly to those in the oil viscosity experiment, which further supports the theory.

Because the radii terms have such a large effect on m, changes to inlet radii lead to large changes in the phase ratio, which can easily cause the device to operate outside a droplet flow regime. This means experiments that vary R_{aq} or R_{oil} to demonstrate the effect on *m* would need to introduce small changes to radii. Premade fused-silica capillaries with different radii can be purchased, but there is a relatively large difference in the available radii, which makes this experiment impractical without in-house microfabrication capabilities. For this reason, experiments varying R_{aq} and R_{oil} were not carried out.

2.4.3 **Aqueous Viscosity Operating Range**

Operating range for aqueous viscosity is limited by the imaging technique employed. As aqueous viscosity increases droplets become spaced farther apart. At high enough aqueous viscosities two are never simultaneously within the field of view of the microscope. This prevents measurement of h_{oil}. To extend the working range, flow resistance through the oil inlet can be increased, thereby decreasing the distance between droplets for a given aqueous phase. This can be achieved by either decreasing R_{oil} or increasing $l_{oi}l$ and η_{oil}. Extending working range in any of these ways will not only decrease distance between droplets but also decreases the sensitivity of the device by decreasing *m.*

Changing η_{oil} is especially convenient compared with using different viscometers with various inlet radii or lengths for different viscosity ranges and is very effective at extending the working range as shown in Figure 10. As seen in Figure 10, aqueous phases with viscosities between 0.96 and 52 cP can be measured on the same device by simply switching out the oil phase, which changes the working range. The working range could possibly be extended farther either by using oil phases with higher viscosities than those tested or by additionally altering inlet lengths or radii.

2.4.4 **Shear Rate Operating Ranges and Control**

A linear relationship between the $\dot{\gamma}$ and ΔP is predicted by eq 13 for a given aqueous solution with constant viscosity. Figure 11 shows the $\dot{\gamma}$ of glycerol solutions with viscosities between 0.96 and 31 cP measured at varying vacuum pressures. A highly linear relationship is seen between the $\dot{\gamma}$ and vacuum pressure for all solutions, with R^2 values between 0.996 and 0.999. Shear rate for Newtonian fluids could be easily controlled even for samples of unknown viscosity. As long as the sample's $\dot{\gamma}$ is measured at two different vacuum pressures, a linear fit could be used to calculate the vacuum pressure required for any desired $\dot{\gamma}$. The good linearity also suggests that P_L is negligible at the flow rates resulting from all vacuum pressures tested.

One interesting observation is that several lines in Figure 11 appear to cross each other. This would mean that two solutions with different viscosities have the same $\dot{\gamma}$ at the same ΔP, which should not be possible. This can easily be explained by the fact that the pressure drop over the collection capillary, which depends on the number of droplets flowing through it and their viscosity, (Groß, Thyagarajan, Kielpinski, Henkel, & Köhler, 2008) is not the same for each glycerol solution. This means that the actual pressures at the junction space are different, even though the same vacuum pressure is being applied.

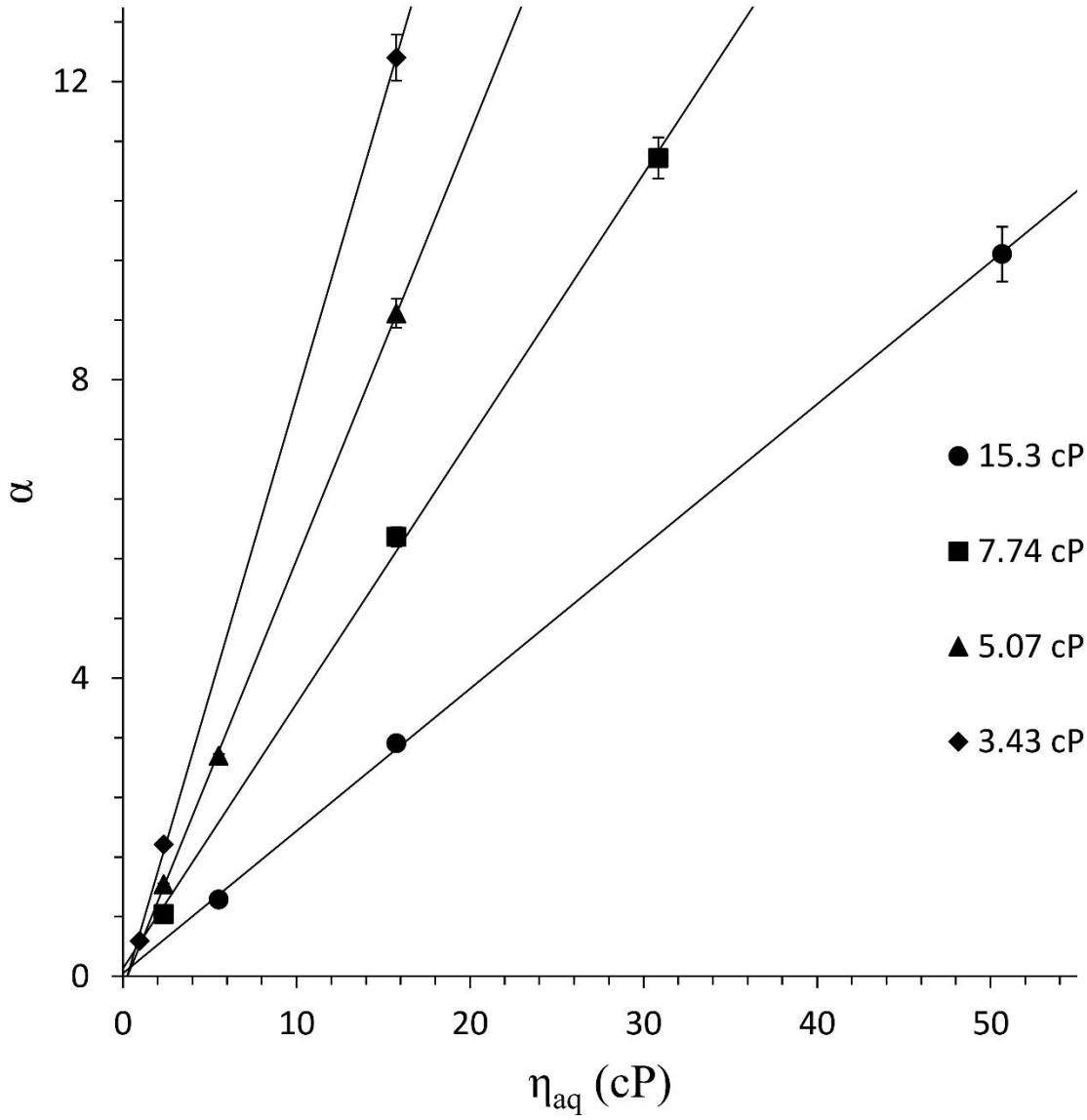

Figure 10: Working range for aqueous viscosity can be altered by using oil phases with varying viscosities. Four calibrations were performed with oil phases of varying viscosity (3.43-15.3 cP) to handle aqueous samples with viscosities between 0.96 and 52 cP. Each data point is the average of 5 measurements.

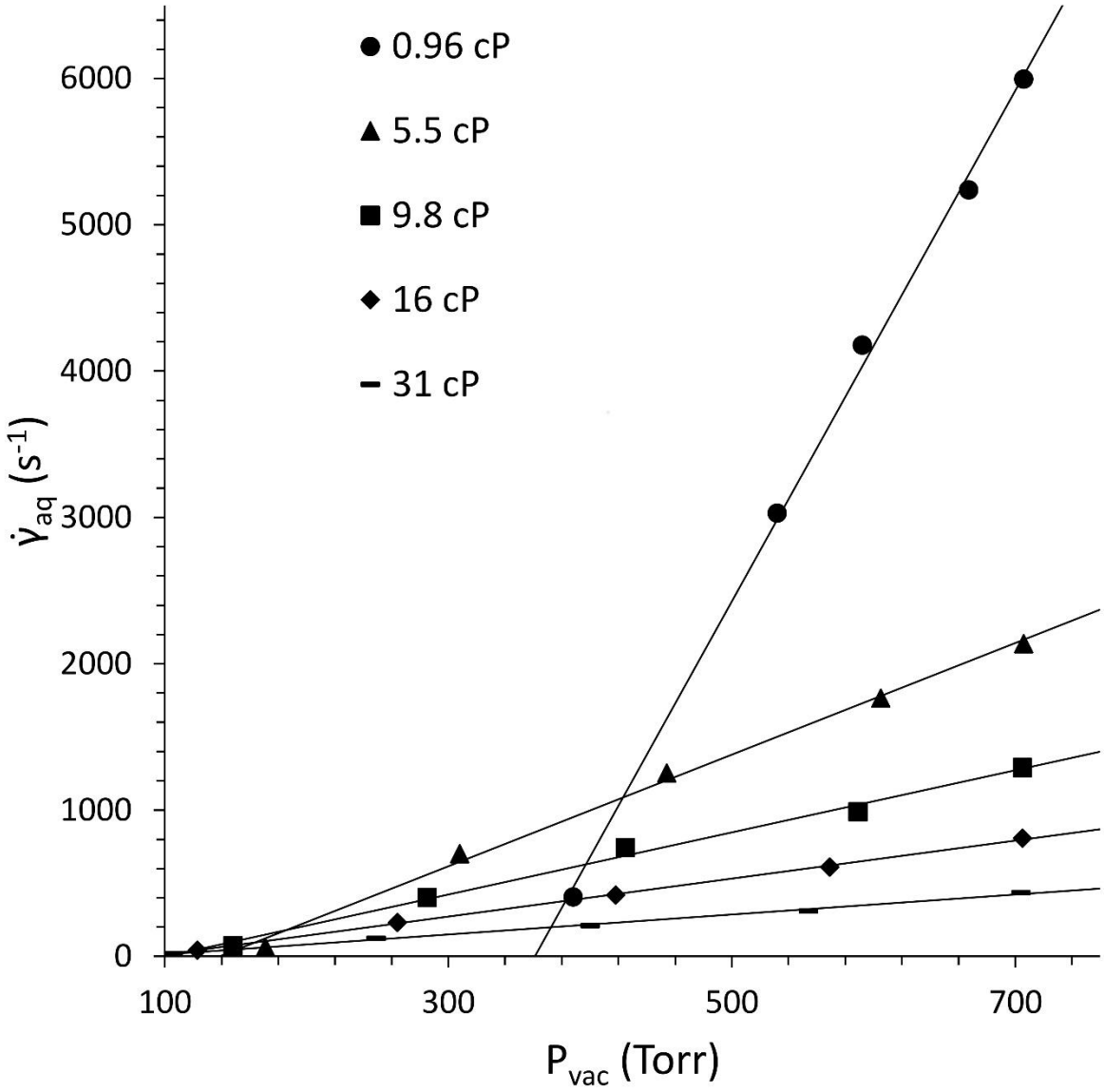

Figure 11: Operating range for $\dot{\gamma}$ was found to depend on the aqueous viscosity. Glycerol standards with various viscosities (0.96-31 cP) were tested to determine minimum and maximum $\dot{\gamma}$ achievable by varying the vacuum pressure. Shear rates as low as 19 s^{-1} and as high as 6.0×10^3 s^{-1} were achieved for the highest and lowest viscosity standards respectively.

Maximum $\dot{\gamma}$ is limited by the maximum flow rate achievable with the vacuum pump, and minimum $\dot{\gamma}$ is limited by droplet production stalling out at low flow rates. Aqueous viscosity itself affects operating range for $\dot{\gamma}$ because higher aqueous viscosities result in lower flow rates and therefore lower shear rates at maximum vacuum pressure. This is seen in Figure 11 because the highest viscosity solution (31 cP) could be operated between 19 and 440 s^{-1}, whereas the lowest viscosity standard (0.96 cP) could be operated between 410 and 6.0×10^3 s^{-1}.

It is possible that these ranges could be extended by changing the radius of the aqueous inlet, which would change the $\dot{\gamma}$ for a given flow rate. The linear relationship between $\dot{\gamma}$ and vacuum pressure predicted by eq 13 and demonstrated in Figure 11 could be used to quickly assess the vacuum pressures required for the new device to operate at the desired $\dot{\gamma}$. Alternatively, the device could be driven by positive pressure rather than vacuum pressure, which would allow higher driving pressures and therefore higher shear rates. As long as the driving pressure of each inlet is kept equal, for instance by using the same pressure reservoir for both inlets, then the pressure terms should still cancel from eq 3.

2.4.5 **Crème de Menthe and Baby Oil Analysis**

Crème de menthe viscosity was found to be 11.7 ± 0.5 cP (n = 10) using a one-point calibration, which was within 1% of the viscosity measured by a U-tube viscometer (11.8 ± 0.3 cP, n = 10). This excellent agreement between methods indicates good accuracy and also indicates that a time-consuming four-point calibration is not necessary. Because of the agreement between methods, it is also likely that crème de menthe exhibits Newtonian behavior even at the high shear rates the measurement was carried out under (1100 s^{-1}). Baby oil was found to have a viscosity of 19.7 ± 0.3 cP (n = 5) using the microfluidic viscometer, which was within 0.1% of the value obtained using the U-tube viscometer (19.7 ± 0.2, n = 3). Accurate determination of baby oil viscosity clearly demonstrates the ability to perform measurements on nonaqueous samples, which greatly expands the practical utility of the device.

One prominent advantage of microfluidic systems is decreased sample consumption. Before the first measurement can be carried out, the 29 nL aqueous inlet capillary must fill and then two droplets must be formed. Considering that crème de menthe sample droplets were found to be 4.1 ± 0.1 nL (n = 10), the first measurement requires 38 nL of sample. Each subsequent measurement requires only an additional 4.1 nL of the sample. For 10 measurements, an average of only 8 nL per measurement is needed, which is considerably smaller than previous reports (Srivastava et al., 2005; Schultz and Furst, 2011) and could be decreased farther by shortening the length of the aqueous inlet capillary or using geometries that form smaller sample droplets.

2.4.6 **Urine and Bovine Serum Analysis**

One important consideration when evaluating the usefulness of an analytical technique is its compatibility with sample components. Poor compatibility with sample components that alter surfaces such as proteins or organic solvents is one major problem for PDMS devices. This is often addressed by diluting samples, removing proteins by digestion (Ye et al., 2015) or separation, adding surfactant to the oil phase, (Roach et al., 2005) or working with fluorinated surfaces such as Teflon. (Srinivasan et al., 2004) First attempts at urine analysis with a native PDMS device saw irreversible changes to the PDMS surface within 1 min that caused inconsistent droplet formation and merging on chip. To address this, the interior surface of the PDMS channel was fluorinated with TCPFOS. This allowed droplets of urine to be formed without any observed changes to the PDMS surface properties, even after periods of time exceeding 3 h. The viscosity of urine was found to be 1.01 ± 0.03 cP (1.00 ± 0.03 cSt, n = 10), which agreed to within 0.1% of the value obtained via U-tube viscometer (1.001 ± 0.005 cSt, n = 10) and fell within normal urinary viscosity values available in the literature. (Inman et al., 2013)

To test the feasibility of analyzing blood serum the viscosity of bovine serum was measured. Bovine serum was found to be 1.97±0.04 cP, (n = 10), which was 17% different than the value determined by U-tube viscometer (1.682±0.007 cP, n = 3). Bovine serum has a protein content of 70

mg/mL (Alberghina et al., 2011), which is significantly higher than that of urine (2.39 mg/mL). (Marshall and Williams, 2000) The large difference between techniques may be due to protein adsorption to the interior surface of the glass inlet capillary, which could cause denaturation or aggregate formation. Future work with high protein samples will likely require fluorination of the interior of the aqueous inlet to avoid sample adsorption.

2.4.7 **Viscosity Determination Using Off-Chip Fluorescence**

Many devices utilize pressure-driven flow to form droplets. (Ward et al., 2005; Deal and Easley, 2012; Brouzes et al., 2015; Isgor et al., 2015) As long as the driving pressures for the aqueous and oil solutions are equal, then the theory behind the device presented could be used to turn any pressure-driven droplet platform using T-junction geometry into a viscometer without any major structural changes. Determination of droplet dimensions using microscopic imaging could be inconvenient for routine viscosity measurements however. Many devices also utilize some sort of technique for droplet analysis such as conductivity, (Cahill et al., 2011) UV–vis spectroscopy (Deal and Easley, 2012) Raman spectroscopy, (Wu et al., 2014) fluorescence, (Gu et al., 2015) or mass spectrometry (MS) (Kelly et al., 2009) that detects signal over time as droplets pass either by or through the detector. If the phase ratio could be extracted from the signal collected over time, then viscosity could be determined without the need for imaging microscopy, which would be more convenient and easier to automate.

Because α is equal to the ratio of V_{oil}/V_{aq}, it should also be equal to the ratio t_{oil}/t_{aq} where t_{oil} and t_{aq} are the durations of time that the detection window of an off-chip fluorescence detector connected to the collection capillary is occupied by either phase over a given interval of time. The area under the curve of a fluorescence trace (Figure 12A) of droplets passing the detector (A_{aq}) should be proportional to t_{aq}, and the area above the curve (A_{oil}) should be proportional to t_{oil}. A_{aq} and A_{oil} were determined after baseline-adjusting the signal and using the average maximum fluorescence signal of each droplet as the

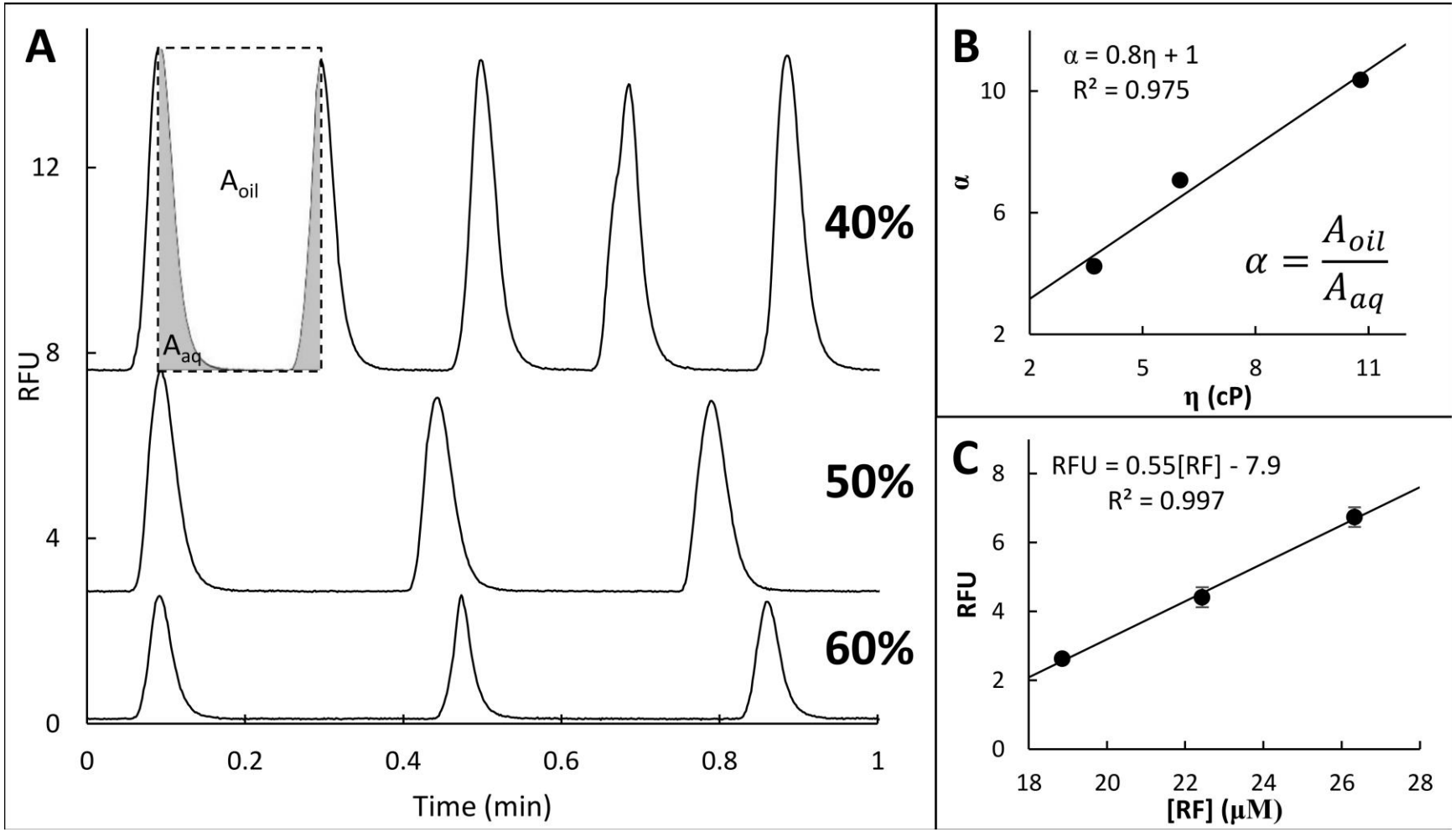

Figure 12: Droplets containing varying concentrations of glycerol (60%, 50%, and 40%) and varying concentrations of riboflavin (18.9, 22.4, and 26.3 μM respectively) were detected using a fluorescence detector connected to the collection capillary. (A) A fluorescence trace of droplets as they moved in and out of the detection window. The area under the curve, A_{aq}, and area above the curve, A_{oil}, were determined as shown by the grey (A_{aq}) and white (A_{oil}) regions inside the dotted box. (B) A_{aq} and A_{oil} were used to approximate α, which was then used with the viscosity of the glycerol solutions to construct a calibration curve. (C) The droplet peak height from the fluorescence trace was used to simultaneously construct a calibration for riboflavin concentration. Each data point for calibrations is the average of 5 measurements.

upper bounds for A_{oil}, as shown by the region outlined with a dotted line in Figure 12A. Using these areas to calculate α allowed for a calibration curve to be constructed (Figure 12B), which was relatively linear ($R^2 = 0.975$). Because each glycerol solution contained a different known riboflavin concentration, concentration information could simultaneously be extracted from the height of each droplet's fluorescence trace, as shown in Figure 12C.

The detection window is simultaneously occupied by both phases for a period of time while a droplet is entering or exiting it. If the volume of the detection window is comparable to the droplet volume, then this period of time is a significantly large fraction of the time interval data is collected over. This is likely the reason droplets are detected as a peak rather than plateau region in the fluorescent trace (Figure 12A). Refraction of the fluorescence source off the aqueous/oil interface during this period of time likely contributes some error to α, which could cause poor linearity in the viscosity calibration. It is possible that better linearity could be achieved if the volume of the detection window (about 1 nL) was made to be significantly smaller than the 4 nL droplet volume. This could be achieved by using a more focused excitation source or using a collection capillary with a smaller inner diameter.

2.5 Conclusions

In this report, a droplet-based microfluidic capillary viscometer is demonstrated with a design consisting of only a simple T junction along with a theoretical basis for device operation. Although single-phase rheometry techniques may be more suitable for many fluids, the design simplicity in conjunction with widespread use of the T-junction motif in droplet platforms makes our technique extremely useful for addition of viscometric capabilities to existing droplet platforms. The ability to measure viscosity with a fluorescence detector is also demonstrated, which implies that existing detection methods used in droplet analysis could be simultaneously used for viscosity determination.

The device is currently capable of analyzing samples down to 38 nL in volume, exhibits stable calibration with only 0.6% drift in slope from run to run, handles aqueous and nonaqueous samples, was shown to be compatible with a biological sample, and was demonstrated to be accurate within 0.1%. Operating range for aqueous viscosity was determined to be 0.96–52 cP. Variable $\dot{\gamma}$ was also possible, with rates between 19 and 6.0×10^3 s^{-1} accessible. On the basis of the presented theory, it can be argued that it should be possible to extend working ranges for both viscosity and $\dot{\gamma}$ by making modifications to the device dimensions or adjusting the oil phase viscosity. Future experiments will assess the suitability of this technique for analyzing non-Newtonian fluids as a function of $\dot{\gamma}$.

Although current manual measurements take several minutes, future devices could utilize automated data processing, allowing for real-time measurements at speeds only limited by droplet generation frequency. A key advantage of the device presented is the ability to measure the viscosity of Newtonian fluids without precise control or measurement of flow rates and pressures. This makes the use of syringe pumps, pressure control devices, flow meters, and pressure sensors unnecessary and greatly simplifies device operation. A final interesting feature of the device is that it encodes information about the relative flow rates of the sample stream and reference stream in the dimensions of the droplet train, which could allow the stream to be stopped, stored, and analyzed at a later time to determine viscosity. This type of handling has been shown to be integral when working with large droplet libraries (Trivedi et al., 2010) or when using droplet formation as a time-resolved sample collection technique. (Wang et al., 2011)

3. A Droplet-Based Microfluidic Capillary Viscometer With On-Chip Reagent Addition For Analysis of Protein Viscosity

3.1 Introduction

Viscosity is an important rheological property arising from molecular interactions which is observable and easily measured on the macroscopic level, which has led to its extensive use for gaining insight into chemical systems and for monitoring subtle chemical changes in systems. The sensitivity of viscosity to changes happening at the molecular level makes it an especially powerful tool in medical screening, where abnormal viscosity of biological fluids including blood, (Sloop, 1996; Kang et al., 2010; Salazar Vázquez et al., 2010) urine, (Inman et al., 2013) and semen, (Stefan Stephanus du Plessis, Sheila Gokul, 2013; Flint et al., 2014) could indicate an underlying medical problem. It is similarly used in quality control testing, especially in the polymer industry(Mould et al., 2011) and food industry, (Bahram-Parvar, 2015) where changes to product viscosity often signify problems at some point in the production line.

Rheological measurements of protein solutions are particularly interesting because the shape and size of proteins significantly impacts solution viscosity. This makes measurement of viscosity an easy way of monitoring protein binding specificity, (Shagawa et al., 2015) conformational changes, (Kamiyama et al., 2008) and aggregation. (Amin et al., 2014) Recently there has been an increased interested in performing rheological measurements on proteins because of applications related to protein aggregation in biopharmaceutical products such as therapeutic monoclonal antibodies. Such aggregation has been shown to cause significant risk of immunogenesis. (Filipe et al., 2012; Bessa et al., 2015)

Over the last decade droplet microfluidics has become a powerful means for high-throughput and automated analysis in proteomics. A wide variety of droplet techniques for protein analysis have been

developed over the past decade. Available droplet techniques for protein analysis include digestion, (Ji et al., 2012) preconcentration, (Ji et al., 2013) separation, (Xiao et al., 2012; Ye et al., 2015) spectroscopic analysis, (Cole et al., 2015; Hess et al., 2015) MS, (Zhu and Fang, 2010; Sun et al., 2012; Ji et al., 2013; Küster et al., 2013; Smith et al., 2013) and even crystallization of proteins for on-chip x-ray diffraction. (Zheng et al., 2004) Because droplet techniques are easily coupled together they have the potential of revolutionizing micro total analysis systems for proteomic applications. (Culbertson et al., 2014) Considering the growing importance of rheological measurements relating to proteins it seems as if a droplet-based rheometer for protein analysis which could be easily coupled to other existing droplet techniques would represent a significant contribution to droplet proteomics. While there have been many microfluidic rheometers reported in the literature (Srivastava and Burns, 2006; Shalliker et al., 2007; Han et al., 2007; Guillot et al., 2008; Nguyen et al., 2008; Pipe and McKinley, 2009; Choi and Park, 2010; Kang et al., 2010; Lan et al., 2010; Nelson et al., 2011; Schultz and Furst, 2011; Solomon and Vanapalli, 2014; McDonnell et al., 2015), aside from the one reported in Chapter 2 there have been surprisingly few based on droplet microfluidics. (Livak-Dahl et al., 2013; Solomon and Vanapalli, 2014) Of these only two operate via continuous droplet formation for entirely online sample processing and high-throughput analysis.

One of these designs uses the velocity of a droplet moving through a constriction in a microfluidic channel to determine droplet viscosity. (Livak-Dahl et al., 2013) This design was capable of accurately and continuously measurement fluid viscosity, and could likely be coupled to many existing droplet analysis techniques, but it was only demonstrated with glycerol standards and was not shown to be compatible with proteins. Furthermore reagent addition upstream of where droplet velocity is measured would alter the measured viscosity. This means the addition of many other droplet techniques would need to be done downstream of viscosity measurement. The other design was one by our group (see Chapter 2) based on measurement of the oil to aqueous phase ratio of a droplets stream. This design

is simple and was also shown to require no precise control over or knowledge of fluid flow rates or pressure drops on chip. Additionally, as seen in Chapter 2, the ability to simultaneously use detection of droplet fluorescence to measure viscosity and concentration was demonstrated, and surface modification was utilized to render the device compatible with samples of human urine.

One limitation of the viscometer presented in Chapter 2, however, is the dependence of device calibration on the oil phase viscosity. This complicates device operation if oil phase viscosity changes, as could occur when using non-Newtonian oil phases such as fluorous surfactant solutions or during the course of variable temperature experiments. Use of fluorous surfactants is especially important in preventing protein adsorption to phase interfaces in droplet microfluidics (Roach et al., 2005), which can cause irreversible changes to the surface properties of devices. Another limitation of the viscometer described in Chapter 2 is the inability to perform droplet-based reagent addition upstream of where viscosity is measured. Reagent addition is required in many applications, such fluorogenic labeling, which would make it impossible to simultaneously measure the viscosity and fluorescence signal of analytes which are not natively fluorescent with the viscometer presented in Chapter 2.

In this chapter, a new means of measuring viscosity is demonstrated using a simple droplet microfluidic platform consisting of only a T-junction. This device uses droplet frequency, rather than the aqueous to oil phase ratio, for determination of sample viscosity. The sensitivity of this device is independent of oil phase viscosity, which permitted the use of non-Newtonian oil phases such as surfactants solutions. This made the device compatible with aqueous protein solutions with concentrations as high as 26 mg/mL. The design also allows for reagent addition upstream of where droplet frequency is measured, which could be useful for coupling multiple droplet techniques for future applications in micro total analysis platforms.

3.2 Theoretical

As discussed in Chapter 2.2.3, the flow rate through the aqueous inlet of a T-junction, Φ_{aq}, during droplet formation is related to the droplet volume, V_{aq}, and the droplet generation frequency, *f*, as shown in equation 2.12.

$$\Phi_{aq} = V_{aq} \times f \tag{2.12}$$

Assuming laminar flow, the flow rate through the aqueous inlet of a junction with cylindrical channels may be determined using Poiseuille's law, as described in Chapter 2.2.1

$$\Phi_{aq} = \frac{\pi R^4 |\Delta P|}{8 \eta l} \tag{2.1}$$

where R is the radius of the aqueous inlet, ΔP is the pressure drop over the aqueous inlet, η is the aqueous viscosity, and l is the length of the aqueous inlet. Substituting eq 2.1 into eq 2.12 and solving for 1/*f* provides the following equation relating the droplet frequency to the dimension of the device (l and R), the operating pressure, and aqueous droplet volume.

$$\frac{1}{f} = \frac{V 8 l}{\pi R^4 |\Delta P|} \times \eta \tag{3.1}$$

When droplets form in a T-junction under conditions where C_a is between 10^{-4} and 0.002, droplet formation is via the squeezing mechanism. (Xu et al., 2008) It has been found that V_{aq} approaches a minimum as the oil flow rate, Φ_{oil}, becomes increasingly larger than the aqueous flow rate, Φ_{aq}. (Garstecki et al., 2006) This minimum volume is dictated largely by junction geometry and is largely independent of shear stress or interfacial stresses because the pressure drop over the droplet dominates shear stress and P_L. The implication of this is that V_{aq} is relatively constant with changes to the viscosity of either phase or changes to the flow rate of either phase as long as $\Phi_{oil} > \Phi_{aq}$ and $10^{-4} < C_a < 0.002$.

If the same device is used with the same driving pressure to form droplets of several viscosity standards with known viscosities and conditions are such that V_{aq} is constant as described above, V_{aq}, l, R, and ΔP are constant and a linear relationship between $1/f$ and η exists where the slope, m, is as follows.

$$m = \frac{V8l}{\pi R^4 |\Delta P|} \tag{3.2}$$

This allows *f* to be measured and used for analysis of aqueous samples of unknown viscosity. It should be noted that large changes in Φ_{oil} could change shear stresses enough to cause small changes in V, thereby altering *m.* Similarly, large changes to the viscosity of either phase will alter surface tension, which could significantly alter shear stresses and P_L. This could affect V_{aq} and lead to nonlinearity. As long as $\Phi_{oil}>\Phi_{aq}$ and $10^{-4}<C_a<0.002$ these effects are expected to be minimal, however. Shear rate for the aqueous phase flowing through the inlet of a droplet generation T-junction may be determined using eq 2.11, as described in Chapter 2.2.3.

3.3 Experimental

3.3.1 Chemicals

Fraction V BSA, 95.5% glycerol,, and 97% 1H,1H,2H,2H-perfluoro-1-octanol (PFO) were purchased from Sigma Aldrich (St. Louis, Mo). KCl was purchased from Fisher Scientific (Waltham, MA). All other chemicals and supplies were obtained as stated in Chapter 2.3.1.

3.3.2 T-Junction Construction

T-junctions with 150 μm i.d. cylindrical channels were constructed in PDMS similar to devices described in Chapter 2.3.2 and Appendix B with some alterations. The first alteration was the addition of 360 μm tapers to both ends of the main T-junction channel rather than only the droplet outlet end. This was achieved by threading two pieces of fused silica capillary (360/170 μm o.d./i.d.) roughly 1 cm in length were threaded over opposite ends of a 1.5 cm length of 150/5 μm o.d./i.d. fused silica capillary.

The second alteration was the inclusion of a 360 μm, rather than 150 μm, T-junction side channel. This was achieved by laying a 1.5 cm piece of 360/50 μm o.d./i.d. capillary with one end sanded to a point down perpendicular to the 150 μm capillary with the sharp point touching the 150 μm capillary. A small amount of epoxy was applied at the point of the 360/50 μm capillary to make a connection between the side branch and main channel.

3.3.3 **Polydimethylsiloxane Surface Treatment**

One large challenge when using PDMS devices is adsorption of sample components such as proteins to the surface. This can render the surface hydrophilic, which causes unstable droplet formation. To prevent this, the interior surface of all devices was fluorinated with TCPFOS as described in Chapter 2.4.6

3.3.4 **Experimental Assembly**

A pressure bomb was constructed using a design obtained from the University of Washington's Proteomic Resource. (MacCose, 2013) This pressure bomb was used to drive aqueous flow during droplet formation, as shown in Figure 13A. The pressure bomb was connected to a helium tank through a Matheson 1L-580 (Matheson, Basking Ridge, NJ) regulator and 3-way ball valve. The aqueous inlet capillary was threaded through a ferrule in the lid of the bomb and the end was submerged in a centrifuge vial containing the aqueous standard or sample. Various driving pressures between 10 and 75 psi were used depending on the experiment.

The tips of aqueous inlet capillaries with 360 μm o.d.'s and various lengths and i.d.'s were sanded to a point and threated up the perpendicular branch of the T-junction, as shown in Figure 13B and 1C. A 100 cm length of 360/50 μm o.d./i.d. capillary was interfaced with one of the tapered ends of the junction

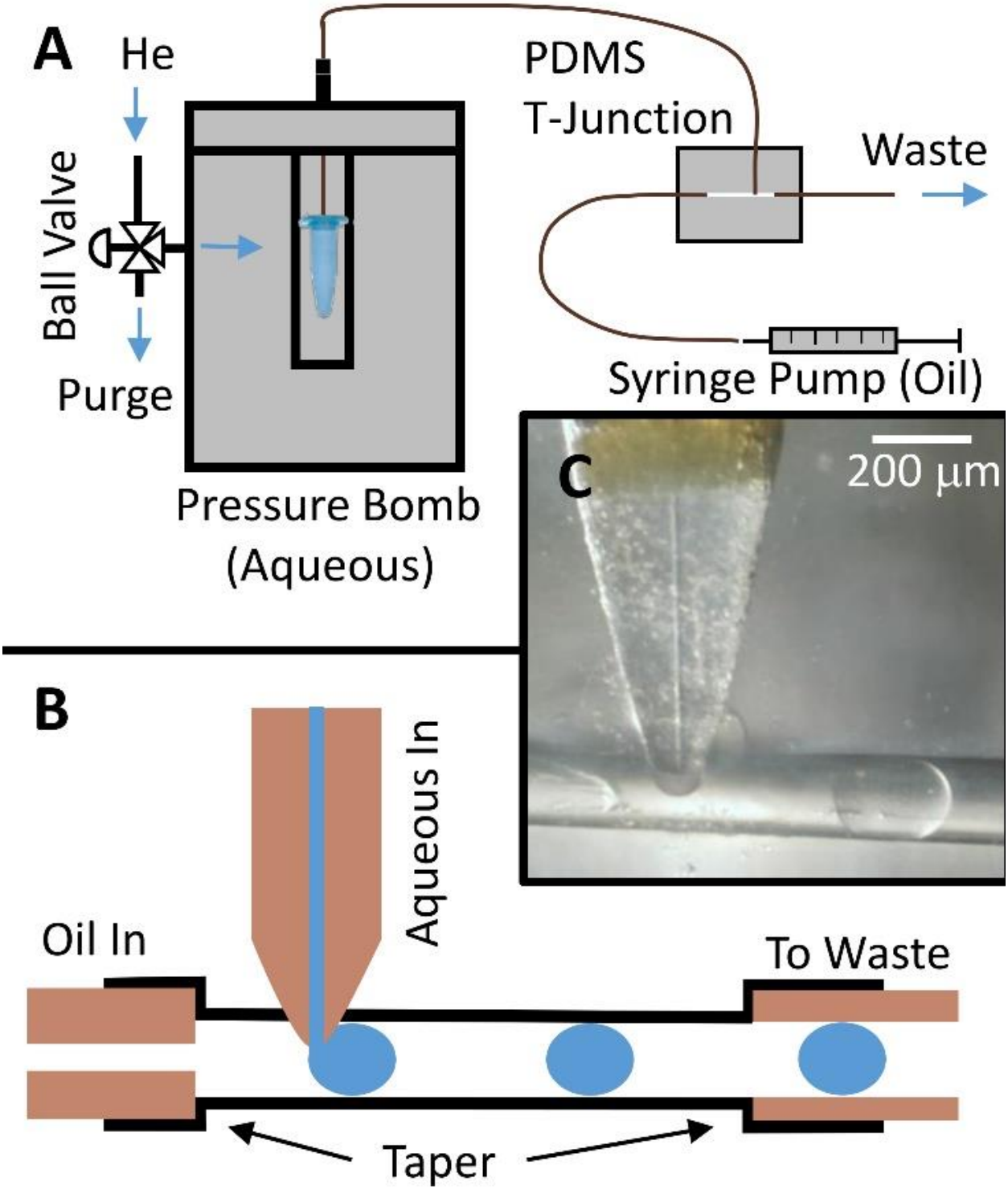

Figure 13: (A) Droplets are formed using a PDMS T-junction. Fluid flow on chip is driven by a pressure bomb (aqueous) and syringe pump (oil). (B) A close up the T-junction architecture. Fused silica capillaries are inserted up tapered channels to form world to chip connections in the plane of the channels. (C) An image of droplet formation at the T-junction showing the sanded tip of the aqueous inlet capillary, the cylindrical PDMS channel, and a droplet of glycerol standard.

and connected to a 500 µL Hamilton Gastight syringe containing 2% wt/wt PFO in PFD, which was used as the oil phase in all experiments. This syringe was connected to a PHD 2000 syringe pump (Harvard Apparatus, Hollistan MA), which was operated at various flow rates depending on the experiment. A 10 cm length of 360/150 µm o.d./i.d. capillary (outlet capillary) was interfaced at the other tapered end of the junction to move droplets off chip to a waste container. The interior surface of this capillary was also fluorinated with TCPFOS.

3.3.5 **Frequency, Volume, and Shear Rate Determination**

Video of droplet formation was obtained using an AmScope SE303-PZ-E binocular microscope interfaced with an MD35 USB microscope camera at 30 frames per second. Droplet frequency was determined by loading video of droplet formation into Icy, an open source microscope image and video tool suite. (de Chaumont et al., 2012) Frames where droplets detached from the aqueous inlet were identified and time data from these frames was extracted using the TimeStamp Overlay plugin. This time data was used to determine the time required to form each droplet, which is $1/f$. All frequency measurements were taken as the average of 4 measurements.

Droplet widths and lengths in pixels were measured using the integrated ImageJ (Schneider et al., 2012) toolbar in Icy. Droplets were assumed to be capsule-shaped with hemispherical ends. Droplet volumes were calculated using the measured dimensions and the formula for the volume of a capsule with hemispherical ends. The width of the channel was used as a scale bar for determination of droplet volumes in nanoliters. Placement of the aqueous inlet capillary seemed to significantly affect the volume and shape of droplets. This caused some devices to produce droplets which were more closely approximated as ellipsoidal, in which case the formula for the volume of an ellipsoid was used instead. Calculated droplet volumes and frequencies were used in conjunction with eq 2.12 to determine Φ_{aq}. This, along with the known diameter of the aqueous inlet, was used to calculate the aqueous $\dot{\gamma}$ using eq. 2.11.

3.3.6 **Theoretical Validation**

The uncertainty of all measured slopes was determined using the LINEST function of Microsoft Excel. To test the theoretical prediction that droplet volume, and therefore m, is independent of Φ_{oil}, calibrations were performed at oil flow rates between 100 and 1000 nL/min using aqueous glycerol solutions with concentrations between 0% and 30% wt/wt. Oil phase flow rates were chosen to keep $\Phi_{oil}/\Phi_{aq}>2$ for the lowest viscosity standards. According to eq 3.2 the slope of the calibration should be linearly proportional to the length of the aqueous inlet. To verify this, calibrations were performed using with aqueous glycerol standards (0%-30% wt/wt) and a 24 cm aqueous inlet. After the first calibration was performed 2 cm was cut from the aqueous inlet and the device was recalibrated. This process was repeated to collect a series of calibrations at 5 different aqueous inlet lengths. Similarly, eq 3.2 predicts a linear relationship between the slope of the calibration and $1/\Delta P$. To explore this, a series of calibrations were performed at different driving pressures using aqueous glycerol solutions between 0% and 85% wt/wt.

The slope of a calibration plays an important role in determining the sensitivity of the measurement as well as the working range. Large slopes result in a large change in droplet frequency for a smaller change in viscosity, and are ideal when a high sensitivity is required. A large slope, however, will lead to excessively low frequencies for higher viscosity samples. If frequencies are low enough the time required to perform measurements becomes prohibitively long. If a large operating range is desired a small slope is acceptable. By using devices with different R, l, and ΔP, the slope can be tailored to a specific application. To demonstrate the maximum sensitivity achievable with the current configuration, a calibration was performed using a device designed to maximize the slope. To test the maximal operating range of the current configuration a calibration was performed using a device designed to minimize slope.

3.3.7 **Viscosity Temperature Adjustment**

Viscosity is highly sensitive to temperature. Because of this calibration standards must either be used under strict temperature control or their viscosities must be adjusted to account for ambient room temperature. As described in Chapter 2.3.4, third order polynomial fits of viscosity data for aqueous glycerol solutions at different temperatures available in the literature (Segur and Oberstar, 1951) were performed using the LINEST function of Excel. These fits were used to predict glycerol solution viscosity at room temperature. These adjusted viscosities were then used in all calibrations. Fit parameters may be found in the Appendix B.

3.3.8 **Demonstration of Reagent Addition Capabilities and Protein Compatibility**

A double T-junction was fabricated for the purpose of reagent addition. This T-junction was identical to all other T-junctions used, with the exception that it included an additional side branch for reagent addition intersecting the main channel at a 90° angle downstream of the aqueous sample inlet branch (reagent inlet). A 20 cm of 360/20 μm o.d./i.d. capillary was used as the aqueous sample inlet, and 80 cm of 360/20 μm o.d./i.d. capillary was installed at the reagent inlet. The interior of the aqueous inlet capillary was fluorinated with TCPFOS to avoid protein adsorption. To prevent protein adsorption to the exterior of the aqueous inlet tip, the tip was sanded flat rather than to a point followed by fluorination. On installing the aqueous inlet, it was pulled back so that it did not protrude into the main channel. The tip of the reagent addition capillary was installed in this manner also. The [PFO] in the oil phase was also increased from 2% to 3.8% (wt/wt) to help prevent protein adsorption.

A lid for the pressure bomb with two ferules was fabricated so that the same pressure bomb could be used to simultaneously drive the aqueous sample and reagent streams through the aqueous inlet and reagent inlet capillaries using 16 psi He. An aqueous riboflavin solution (2.34 μM) was used as a fluorescent tracer and delivered through the reagent inlet to simulate reagent addition to droplets of 0%-

30% glycerol. Droplet frequency was measured on chip upstream from reagent addition via video and off chip downstream of reagent addition via fluorescent detection of droplets through a window burned into the outlet capillary as described in 2.3.10. To demonstrate the ability to perform measurements on samples containing concentrated proteins, the viscosity of a 26 mg/mL BSA solution prepared in 0.01 M KCl was also measured on chip and independently using a size 100 U-tube viscometer.

3.4 Results and Discussion

3.4.1 Device Performance and Operating Ranges

Calibrations were very linear, with R^2 values as high as 0.9999, as seen in Figure 14. Quadruplicate measurements of solution viscosity always consistently yielded RSD values of less than 1%, and successive calibrations of the same device yielded less than a 1% RSD in the slope (n=3), providing the device was not moved during experiments. Moving devices resulted in noticeable changes in droplet volume, which resulted in up to 15% changes in slope. This observed change in droplet volume likely resulted from flexing of the PDMS channel, which moved the imbedded aqueous inlet capillary and slightly changed its positioning at the junction space. Because the slope is dependent on droplet volume, which, in turn, depends on device geometry, this resulted in changes to device calibration.

Unsurprisingly device to device variation was quite large with a 12% RSD in slopes across three devices. This was also likely due to differences in aqueous inlet placement. Differences in droplet volumes between devices of up to 16% were observed. These large device to device variations and instabilities in calibration would likely not be problematic if devices were manufactured using traditional T-junctions without imbedded capillaries. It should also be noted that calibration of the viscometer described in Chapter 2 is independent of droplet volume, which allowed for more rugged operation.

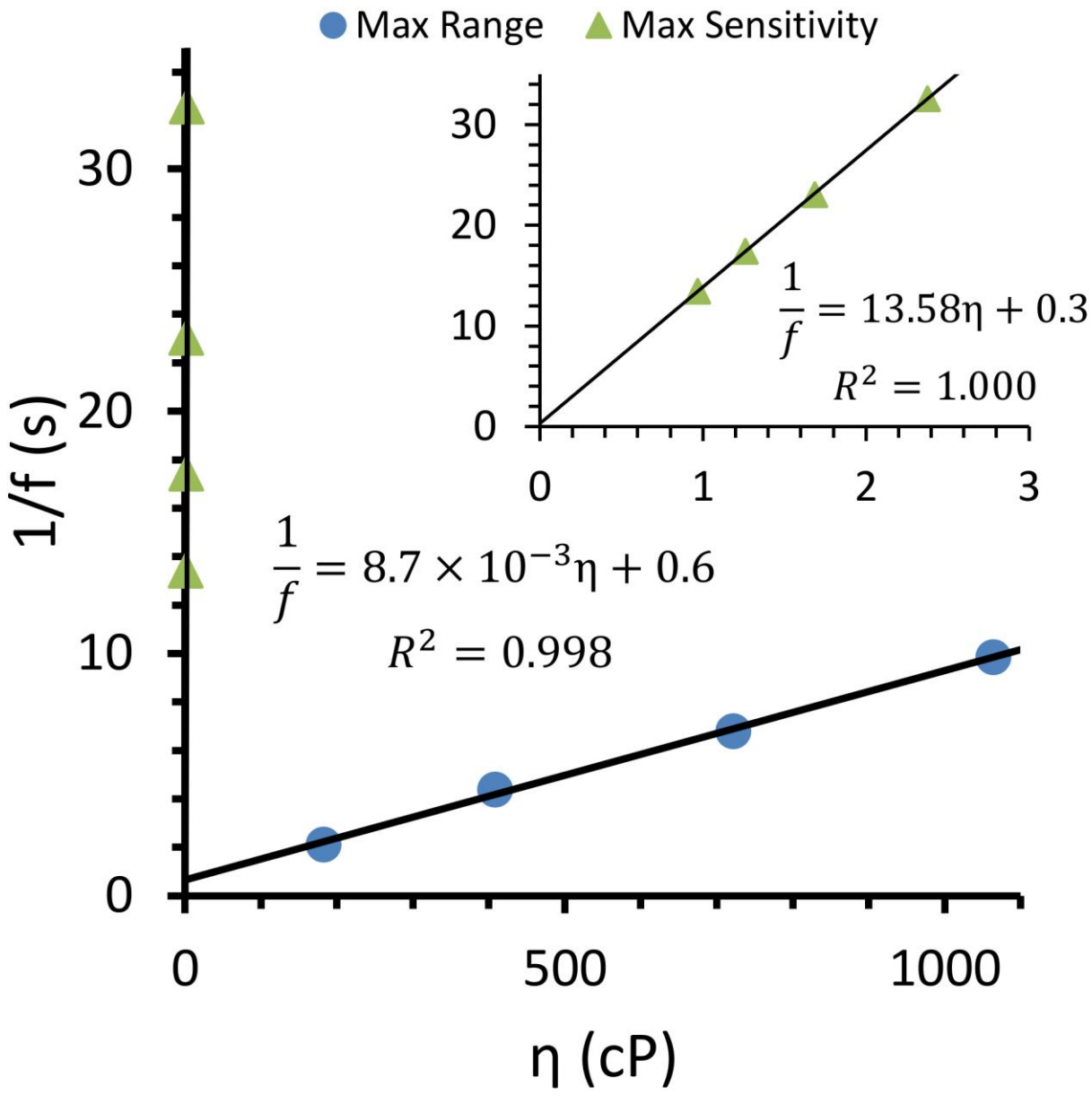

Figure 14: Calibrations of devices designed for maximum sensitivity or maximum operating range. A calibration performed using a 10 μm I.D 25 cm aqueous inlet, 20 psi He, 200 nL/min oil flow rate, and aqueous glycerol solutions between 0% and 30% wt/wt provided a large slope and therefore exceptional sensitivity for low viscosity samples, as shown in the inset graph. A calibration performed using a 50 μm I.D 16 cm aqueous inlet, 40 psi He, 400 nL/min oil flow rate, and aqueous glycerol solutions between 90% and 100% wt/wt. had a very small slope, which extended the working range up to 1000 cP. All frequency measurements were performed in quadruplicate. Error bars are covered by data point graphics.

The volume of the aqueous inlet capillary is roughly 13 nL. This inlet must fill with sample and a minimum of two droplets (approximately 3 nL each) must be formed to perform the first measurement. A minimum sample volume of 19 nL is therefore required for the first measurement. Each subsequent measurement then only requires 3 nL of additional sample. This volume is half the volume required for the viscometer presented in Chapter 2, and would likely be negligible compared with the available volume of most samples. In this way it could be treated as a nondestructive measurement technique, even if droplets were not used for subsequent analysis and sample was simply moved to waste.

The working range of the current instrument design was limited by the time required to form droplets at higher aqueous viscosities and the need to operate at increasingly high oil flow rates to ensure $\Phi_{oil}>\Phi_{aq}$ at lower aqueous viscosities. To explore the upper bounds of the measurement range, a device was designed with a short aqueous inlet of large diameter. This design was made such that the aqueous inlet had a very low flow resistance and provided sufficiently high droplet frequencies even for high viscosity standards. As shown in Figure 14, it was possible to easily measure fluids with viscosities up to 1000 cP (the viscosity of 100% glycerol at the ambient lab temperature) using this design. Viscosities above that of 100% glycerol were not tested, but considering 100% glycerol droplets only required 10 seconds to form it is reasonable to expect even higher viscosities could be measured without prohibitively long measurement times. This marks a nearly two order of magnitude increase in the operating range as compared with The viscometer presented in Chapter 2.

To explore maximum sensitivity possible for the current device, a viscometer was designed with a long aqueous inlet of small diameter. This design was made to maximize the slope. Using the system response for 10% glycerol, the analytical sensitivity for this device was calculated to be 160 cP^{-1}, which makes it roughly 3 times as sensitive as the viscometer presented in Chapter 2.

3.4.2 **Theoretical Validation**

One theoretical prediction of particular interest is the independence of the slope of the calibration from the oil phase flow rate. This independence should make calibration much more rugged under conditions where the oil phase flow rate is unstable or fluctuates, as is the case with oscillations in syringe pump output. As seen in Figure 15A, varying the oil phase flow rate by an order of magnitude only lead to a 21% decrease in slope, indicating it is relatively insensitive to changes in oil flow. The average droplet volume at each of these oil flow rates was also measured, and was found to decrease 16% with an order of magnitude increase in flow rate, which is also shown in Figure 15A. This suggests that shear stress exerted on the droplet by the oil phase plays a small roll in droplet breakup, and confirms that operation is largely in the squeezing regime.

A linear relationship between V_{aq} and *m* is predicted based on eq 3.2. To verify this relationship the slope resulting from each oil flow rate was plotted vs. the resulting droplet volume for each oil phase flow rate as shown in Figure 15B. The plot is linear as expected, and fits within a 95% confidence region which was calculated using eq 3.2, the uncertainties in l, R, V_{aq}, and ΔP, and the partial derivatives method for propagation of uncertainty. The confidence region is large because R is raised to the fourth power in eq 3.2, which causes small uncertainties in it to be amplified. This plot is consistent with theoretical predictions, and also lends evidence to the assumption that the observed dependence of *m* on Φ_{oil} is due to changes in droplet volume.

The viscometer described in Chapter 2 used vacuum pressure to drive oil flow and had a calibration which depended on the viscosity of the oil phase. This became problematic when utilizing non-Newtonian oil phases, such as fluorous surfactant. Fluorous surfactants are often added to the oil phase in droplet microfluidics to stabilize droplet formation and prevent adsorption of sample components to the interior surface of the device. Use of fluorous surfactants made the slope of the calibration highly sensitive to fluctuations or changes in the oil phase flow rate. An interesting implication of the ability to

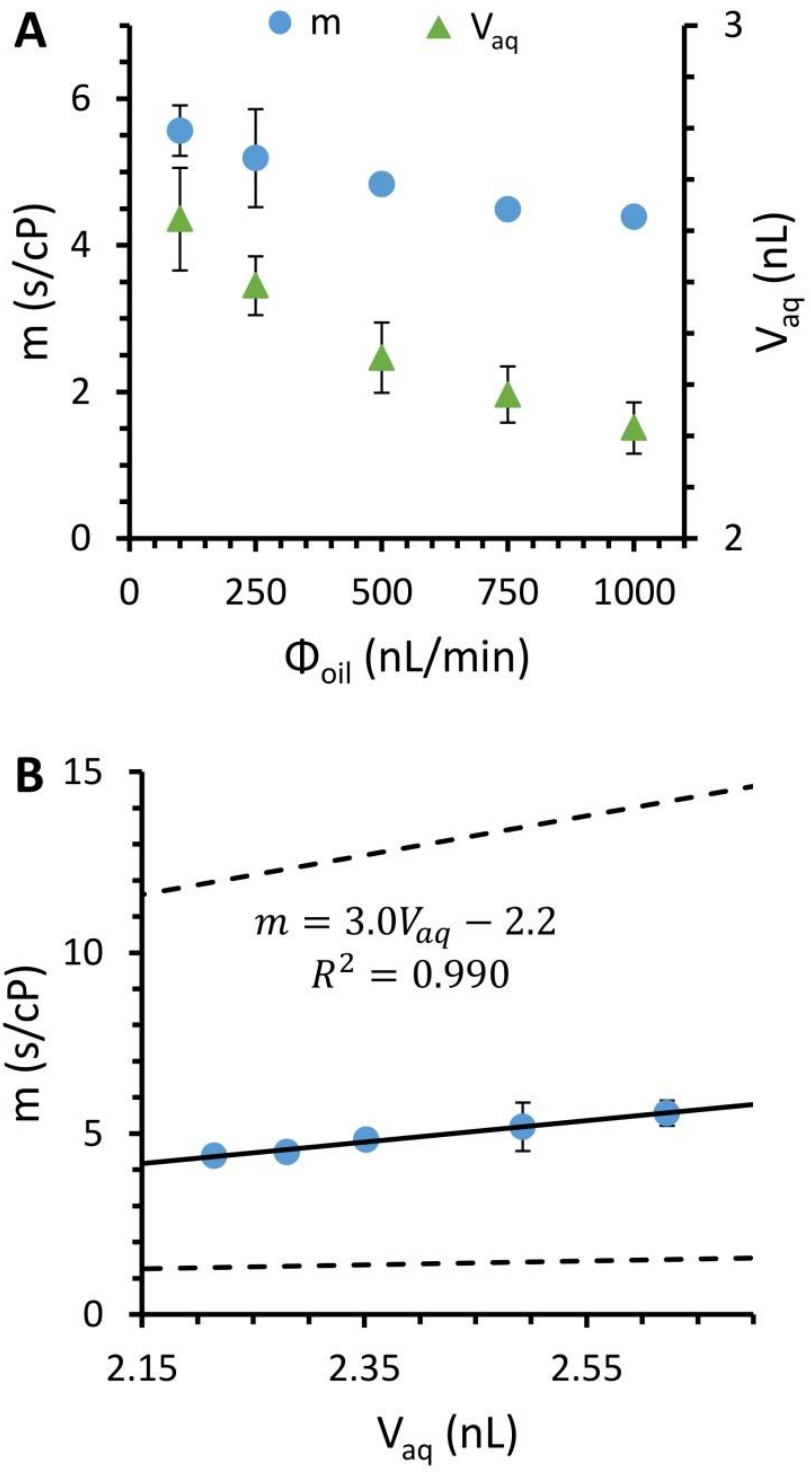

Figure 15: (A) Oil phase flow rate was found to have a small effect on droplet volume, and therefore the slope of the calibration, as is predicted for the squeezing regime when $\Phi_{oil}>\Phi_{aq}$. Calibrations were performed using a 10 µ, I.D. 25.7 cm aqueous inlet, 31 psi He, and aqueous glycerol standards measured in triplicate (B) As predicted by the theory, the slope was found to be linearly related to the observed droplet volumes at varying Φ_{oil}. Each data point represents one measured slope.

utilize a syringe pump to work at a constant oil phase flow, as demonstrated with our new operating mode, is that surfactants such as PFO may be used without having any effect on the slope of the calibration.

A linear relationship between *m* and the length of the aqueous inlet is predicted by eq 3.2. Figure 16A shows the slopes of a series of calibrations taken with different aqueous inlet lengths. The slope is linear as predicted by the theory and also fits within a 95% calculated confidence region. Similarly, eq 3.2 predicts a linear relationship between *m* and $1/\Delta P$. Figure 16B shows a plot of slopes experimentally measured at different driving pressures. The resulting plot is linear as expected and fits within a calculated 95% confidence region. Both of these experiments lend evidence to the theory behind device operation, and also demonstrate the ability to manipulate device sensitivity by altering the inlet length and driving pressure.

Because there is a pressure drop over the outlet capillary, the pressure at the junction where the aqueous inlet capillary terminates is not actually equal to atmospheric pressure. This complicates determination of the pressure drop over the aqueous inlet. If the pressure drop over the 150 μm outlet capillary is assumed to be very small compared with the pressure drop over the smaller diameter aqueous inlet capillary, however, the pressure at the junction can be approximated as atmospheric pressure. In this case, the pressure drop over the aqueous capillary is simply the pressure displayed on the regulator. The fact that measured slopes in Figure 15B fit within the calculated 95% confidence region lends support to this assumption. Also, droplets of different viscosity would result in different pressure drops over the outlet capillary for each standard of a calibration curve. If the outlet capillary pressure drop was significant compared with the pressure drop over the aqueous inlet capillary a different ΔP, and therefore different slope, would exist for each calibration standard. This would lead to nonlinearity in the calibration which was not observed.

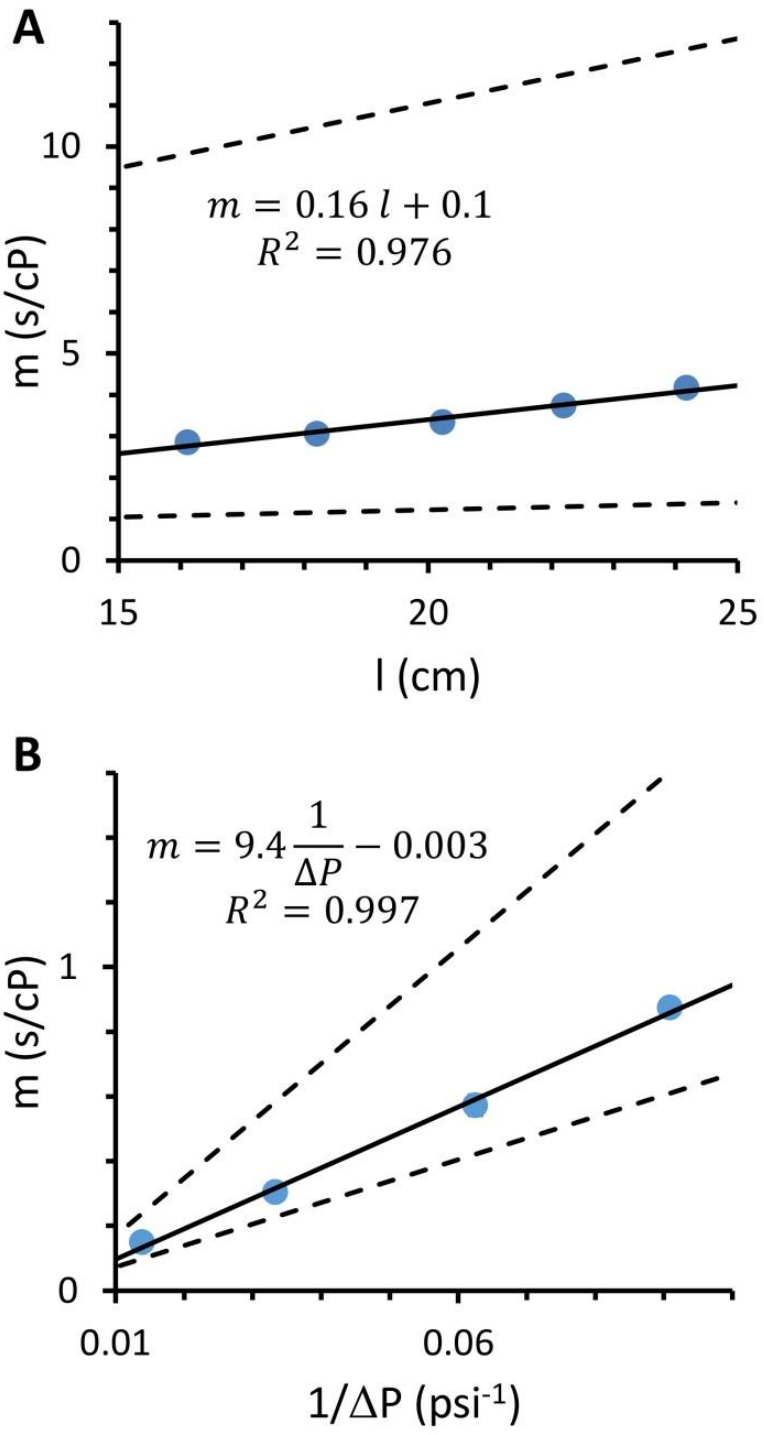

Figure 16: (A) The slope was found to be linearly proportional to the length of the aqueous inlet, as predicted by theory. Calibrations were performed using a 10 µm I.D. aqueous inlet with varying lengths, 60 psi He, an oil flow rate of 200 nL/min, and aqueous glycerol standards measured in triplicate. (B) A linear relationship between slope and 1/ΔP, as predicted by theory. Calibrations were performed using a 20 µm I.D. 20 cm aqueous inlet, 500 nL/min oil flow rate, and glycerol solutions measured in triplicate. Each data point represents a single measured slope.

In Chapter 2 viscosity was measured at varying shear rate by altering the driving pressure of the device. Because the operating mode presented here has a calibration that depends on the driving pressure, controlling $\dot{\gamma}$ by altering ΔP would require recalibration at each pressure, which would be impractical. For this reason, variable shear experiments were not preformed and are better suited for the design presented in Chapter 2. To estimate the range of shear rates the device operates under, however, observed shear rates were calculated using eq 2.11 for experiments were shear was likely to be highest and lowest. Small R, l, and η in conjunction with a high ΔP will result in higher shear rates. Of all experiments the first calibration standard of the "max sensitivity" design presented in Figure 14 should have the highest $\dot{\gamma}$, and was found to operate at a shear rate of $1.4\times10^4\ s^{-1}$. Lower shear rates should be observed at large values of R, l, and η in conjunction with a low ΔP. Of all the experiments the last calibration standard of the "max range" design presented in Figure 14 had the lowest $\dot{\gamma}$ at $10\ s^{-1}$. This marks a nearly order of magnitude increase in the range of operating shear rates as compared with the viscometer from Chapter 2.

3.4.3 **Viscosity Determination Downstream of Reagent Addition**

As long as the reagent flow rate is lower than that of the aqueous sample inlet budding droplets of reagent are cleaved off by incoming aqueous sample droplets before they ever break off to form independent droplets. The frequency of this process is limited by the frequency of the incoming sample droplets, the droplet frequency before and after the reagent addition T must be equal. This means viscosity calibration could be performed before or after reagent addition without effecting the measurement.

Figure 17A shows a fluorescence trace of droplets of different glycerol solutions collected off chip and downstream of reagent addition. The frequency of droplet generation can be determined from these fluorescence traces by measuring the time between peaks in the trace. Figure 17B shows an overlay of calibration curves made by determining the frequency via video on chip prior to reagent addition and by using peak heights from the fluorescent trace to determine droplet frequency off chip and downstream

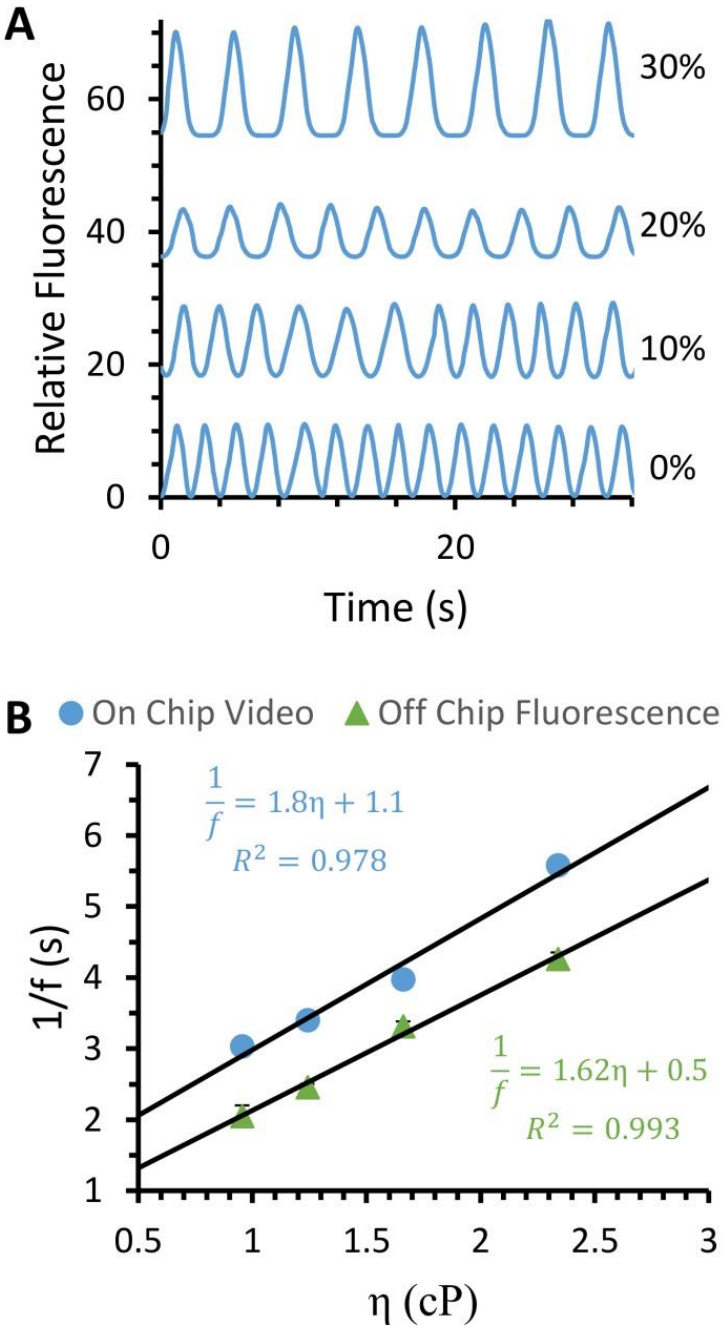

Figure 17: (A) An example fluorescence trace of droplets of 0-30% wt/wt glycerol moving through the waste capillary past a fluorescence detection window. Higher viscosity standards exhibit smaller droplet frequencies, which is seen in the number of peaks over a given period of time. (B) Average droplet frequency for each standard was determined using time points for the first four peaks in the fluorescence trace and by using video on chip. These frequencies were used to construct two calibrations. These calibrations are slightly different, which is likely due to timing differences between the National Instruments data acquisition board used for fluorescence signal collection and the Amscope microscope USB camera (n=4 for each frequency).

of reagent addition. As is seen in Figure 17B both methods provide a linear calibration with similar observed frequency values for each glycerol standard. The slight difference between the two calibrations may be due to an inaccuracy in the timer on the chipset of the USB video camera or data acquisition card for the fluorescence detector. The viscometer described in Chapter 2 also demonstrated the ability to perform a calibration utilizing a fluorescence trace, however problems with refraction of the excitation source off the droplet interface caused nonlinearity in the calibration. Detecting droplet frequency rather than oil to aqueous phase ratio has the benefit of being unaffected by refraction of the excitation source off phase boundaries, which allows for a much more linear calibration.

3.4.4 **Device compatibility with concentrated protein solutions**

The viscometer in Chapter 2.4.6 was incompatible with the high concentration present in bovine serum. On fluorinating the interior of the aqueous inlet along with the PDMS channels and outlet capillary, concentrated BSA solutions up to 26 mg/mL did not lead to any observed changes to droplet formation on chip. This indicates no significant adsorption of proteins to the PDMS surface or aqueous inlet capillary. This exceeds the protein content of cerebrospinal fluid (0.35 mg/mL) but is slightly lower than the protein content of blood (70 mg/mL) (Siegel et al., 1999), indicating the device may be capable of analyzing high-protein content biological samples. The viscosity of a 26 mg/mL BSA solution was determined to be 1.02±0.02 cP (n=3) via calibration on chip, which was the same within error as a value obtained via U-Tube viscometer (1.01±0.02 cP, n=3). This close agreement also indicates minimal adsorption of proteins from the sample to the interior of the aqueous inlet. Measurement of BSA off chip was not possible because protein adsorption to the interior surface of the glass outlet capillary caused droplet merging problems. This caused irregular peak frequencies in the fluorescence trace, but did not affect upstream droplet formation. Future devices may require better surface treatment of the outlet capillary to render it more completely fluorinated, or could use Teflon tubing to move droplets off chip rather than a fused silica capillary.

3.5 Conclusions

In this chapter theory and demonstration of a capillary viscometer is presented which uses the frequency of droplet production at a simple microfluidic T-junction to determine fluid viscosity. The device is capable of highly precise measurements with %RSD values below 1% and was also found to be accurate to within 1% for a concentrated BSA solution. Device operation was demonstrated to be relatively robust and rugged with respect to the oil phase flow rate, with observed changes to slope of only 21% with an order of magnitude change in oil flow rate. This indicates that small fluctuations in the syringe pump output or intentional changes in oil phase flow rate should not appreciably effect device operation. A nearly two order of magnitude expansion of the working range for viscosity, an order of magnitude increase in working range for $\dot{\gamma}$, and a threefold increase in sensitivity is demonstrated compared with the droplet viscometer described in Chapter 2.

A significant advantage of the device is its compatibility with oil phase surfactants such as PFO. This was used to prevent protein adsorption, which allowed viscometric measurements of a concentrated protein solution without adverse effects of protein adsorption to device surfaces. Additionally, the ability to measure viscosity utilizing off chip fluorescence detection of droplets is demonstrated downstream of a reagent addition T. This feature could allow our viscometer to be more easily coupled to other droplet-based proteomic techniques for addition of viscometric measurement capabilities to droplet-based micro total analysis platforms.

4. Development of a Simplified Microfluidic Injector for Analysis of Droplet Content via Capillary Electrophoresis

Reprinted with permission from M. DeLaMarre and S. Shippy, *Development of a Simplified Microfluidic Injector for Analysis of Droplet Content via Capillary Electrophoresis*, Analytical Chemistry, 2014. 86(20): p. 10193-10200. Copyright 2014 American Chemical Society. (See Appendix A)

4.1 Introduction

The field of droplet-based microfluidics has gained increasing popularity over the past decade, seeing rapid expansion and even commercial success. Droplet-based platforms encapsulate an aqueous sample droplet in an immiscible carrier fluid, such as a fluorous oil, and can be used to perform many routine laboratory sample handling procedures such as aliquoting, sample storage, and reagent addition (Song et al., 2006; Theberge et al., 2010; Desmarais et al., 2012; Schneider et al., 2013) on a highly miniaturized scale. Scaling these operations down minimizes reagent consumption and associated cost, improves mass and heat transfer, reduces laboratory footprint, and allows for automated high-throughput analysis. Chemical analysis of droplet content can present a challenge, however, as the fluorous phase is often incompatible with assay techniques.

One interesting application of droplet platforms is in the prevention of zone diffusion in flow streams, which is especially important in separation techniques such as liquid chromatography (LC) and CE and also in time-resolved sampling techniques such as microdialysis. Formation of a droplet train from a flow stream encapsulates sample zones and prevents them from mixing. This allows sample to be stored without any zone diffusion. Droplet-based platforms have recently been reported

which utilize this concept to preserve separation resolution (Edgar et al., 2009) in separation techniques and temporal resolution in time-resolved sample collection. (Slaney et al., 2011)

Because the carrier phase must be removed prior to assay techniques involving a separation, droplet content analysis has largely been performed with optical spectroscopy techniques like fluorescence, while other techniques that provide more chemical information such as CE or LC are largely inaccessible. The importance of separations to the fields of chemistry and biology, paired with the significant benefits droplet platforms provide, makes it particularly important to develop simple and reliable methods of delivering droplet content to a separation technique while excluding the immiscible carrier phase.

Previously successful methods have achieved analysis of droplet content by CE using a desegmentation process (Roman et al., 2008; Wang et al., 2009; Pei et al., 2010; Filla et al., 2011; Rogers et al., 2011) in which droplets are merged and reform a continuous aqueous stream and are then injected by traditional means such as electrokinetic gating. Desegmentation provides the benefit of passively merging droplets so automation can be easily built in but reintroduces diffusive mixing between zones and also couples the droplet merging frequency to injection frequency, which limits the length of time available for analysis. Other reported designs demonstrate the capability of merging a single aqueous droplet with a continuous aqueous stream for delivery to MS or CE without desegmentation. (Edgar et al., 2006; Roman et al., 2008; Kelly et al., 2009; Niu et al., 2009, 2013) These designs avoid reintroduction of zone diffusion, and because droplets do not need to be passively merged, introduction of sample for analysis can be performed “on-demand” if desired, which places no limit on the time available for analysis. Although not as easily automated, technologies for computer-controlled fine manipulation of droplets exist (Langelier et al., 2009) and could be used to bring automation to these techniques as well.

One barrier to faster expansion of research and application of droplet analysis by CE is likely the complicated microfluidic architectures required to transfer droplets to an electrophoresis channel, which

require sophisticated microfabrication techniques such as photolithography and also causes problems with robustness and ruggedness. The first reports (Edgar et al., 2006) of droplet analysis by CE benefited from a simple T-junction design but suffered from poor separation quality due to the immiscible carrier phase leaking into the separation channel. This problem was solved by use of a 2-layered extraction bridge design (Pei et al., 2010), which has demonstrated very reproducible and high quality separations but required elaborate fabrication techniques including glass etching and laminar-flow surface patterning. A later design (Filla et al., 2011) introduced an extremely convenient surface-patterning technique using water to guard a channel against corona discharge, which allowed the use of PDMS. This development simplified the fabrication process compared with glass chips, but the specific design used introduced mixing via desegmentation. Most recently, an even simpler PDMS device which delivers droplets to CE without desegmentation has been demonstrated. (Niu et al., 2013) This device benefits from one of the simplest designs yet, but requires hydrophobic foam to soak up the immiscible carrier fluid and could be further simplified.

In this chapter, a microfluidic device is presented capable of injecting 750 pL sample droplets into a channel for separation by CE on-demand while excluding the fluorous carrier phase. This device consists of only two straight PDMS channels and, to our knowledge, is one of the simplest designs reported to date. As a proof-of-concept and to characterize device performance, samples containing riboflavin, an important micronutrient, were formed into droplet trains, stored in a freezer, and then thawed for injection and analysis by CE.

4.2 Materials and Methods

4.2.1 Chemicals

All chemicals used were of analytical grade or better. Sodium tetraborate was purchased from Sigma-Aldrich (St. Louis, Mo). Su-8 negative photoresist was purchased from MicroChem Corporation

(Newton, MA). Sodium hydroxide was purchased from Fisher Scientific (Fair Lawn, NJ). All other chemicals and materials were obtained as stated in Chapter 2.3.1.

4.2.2 **Device Fabrication**

Silicon masters were fabricated in SU-8 negative photoresist on a silicon wafer patterned by UV exposure through a high-resolution printed photomask. All channels in both droplet formation and injection devices described had varying widths and were 75 μm tall.

4.2.3 **Droplet Formation Device**

Sample droplets were formed with a PDMS microfluidic T-junction (Figure 18) with a 50 μm wide aqueous inlet channel intersecting a 75 μm wide oil channel at a 90° angle. All capillaries were interfaced with the chip in the plane of the channels by pushing them up the channel from the edge of the chip. The tips of all capillaries were sanded to a point to reduce dead volume and prevent damage to the channel on installation of the capillary. A 2.5 cm length of 20 μm (i.d.)/150 μm (o.d.) capillary (aqueous inlet capillary) was installed at the aqueous inlet branch of the T-junction and was pushed up the channel until the tip just barely protruded into the junction space. A 15 cm length of 50 μm (i.d.)/150 μm (o.d.) capillary (oil inlet capillary) was connected to the oil channel. Silicon vacuum grease was applied to both capillaries at the edge of the chip to prevent air from leaking into the channel.

Sample droplets were collected in a 6.5 cm length of 75 μm (i.d.)/360 μm (o.d.) capillary (collection capillary). The collection capillary had a 1 cm piece of 178 μm (i.d.)/366 μm (o.d.) stainless steel hypodermic tubing (Small Parts Inc., Miramar, FL) that was epoxied over the end, which served as an adapter for connecting the device to a vacuum pump. The collection capillary was treated for 30 s with Sigmacote to render the interior surface silanized. This collection capillary was installed at the branch of the T-junction opposite the oil inlet.

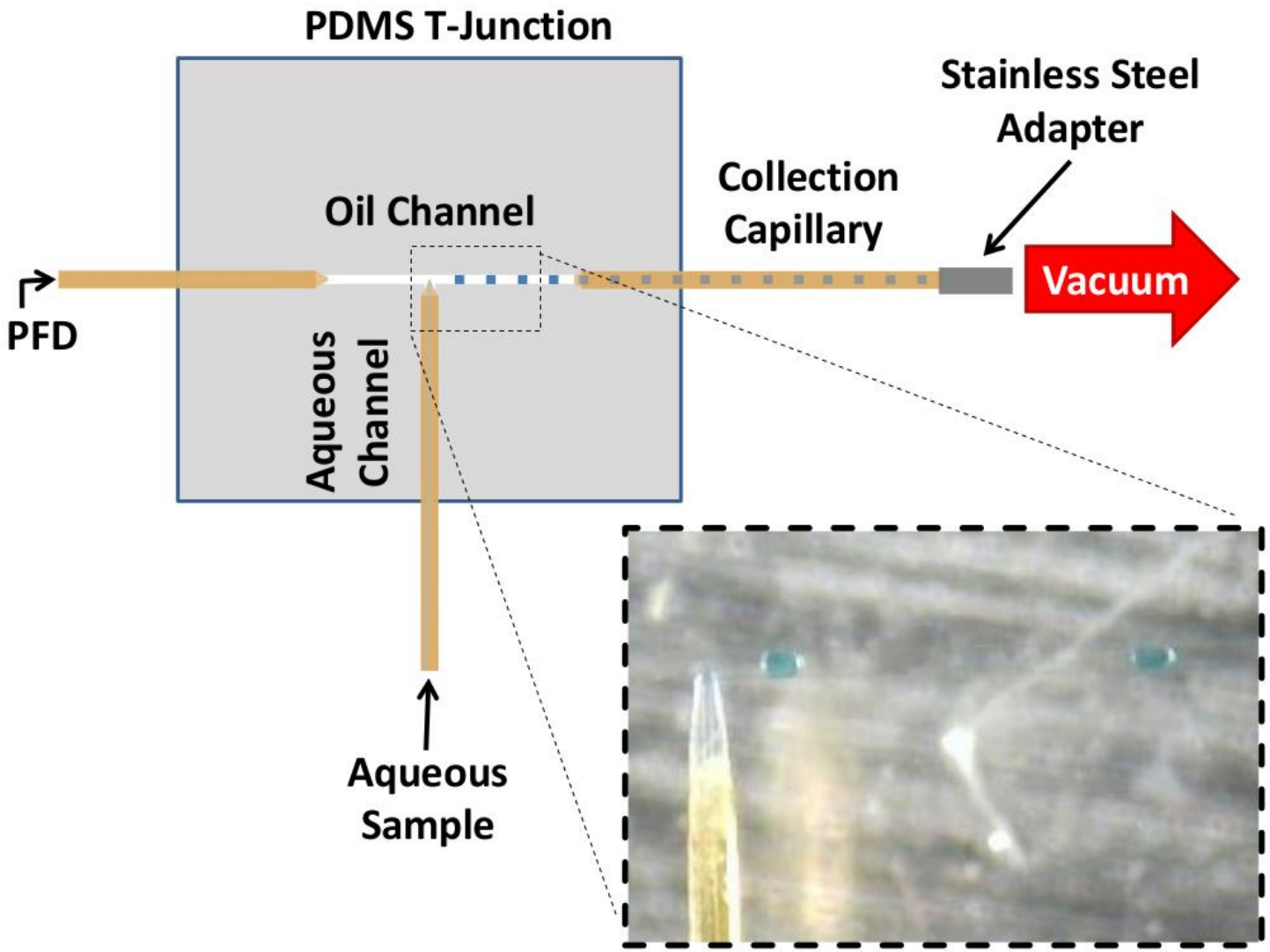

Figure 18: A PDMS T-junction used for preparation of droplet trains. The Aqueous inlet capillary is pushed up the aqueous inlet channel until the tip extends into the junction space. Vacuum is applied to the end of the Collection capillary to pull fluid through the chip, allowing for aqueous sample collection and storage.

4.2.4 **Injector Device**

The injector consisted of two channels intersecting out of plane with a cross geometry (Figure 19A). This was achieved by forming each channel on separate slabs of PDMS and then bonding the two pieces with the patterned sides facing each other after manually aligning the channels. The bottom channel (droplet channel) was 75 μm wide, and the top channel (separation channel) was 30 μm wide at the junction but tapered up to 75 μm wide at the edge of the chip. A reservoir hole was punched at one end of each channel, with the other end of each channel ending at the edge of the chip. The end of a 60 cm length of 50 μm (i.d.)/360 μm (o.d.) capillary (separation capillary) was installed at the end of the separation channel by pushing it up the tapered end of the separation channel until the tip just reached the end of the taper and was then glued to the chip using epoxy. A 3.5 mm detection window was burned 14 cm from the end of the separation capillary using a nichrome wire coil.

4.2.5 **Sample Collection and Storage**

Riboflavin was used as a fluorescent standard to characterize injections. Aqueous riboflavin standards were prepared by serial dilution of riboflavin stock solution. Glycerol was added to each standard as a viscosity modifier (55 wt %/wt). A blank solution consisting of 55% (w/w) aqueous glycerol solution was also prepared. The reported riboflavin concentrations account for dilution due to glycerol addition.

The stainless steel adapter of the collection capillary was connected to a 1/32 in. tygon tube leading to a Welch 2034 DRYFAST vacuum pump (Welch-Ilmvac, Niles, IL) through a regulator (Squire-cogswell, Gurnee, IL) and digital pressure gauge (Vacuubrand DVR 2, Wertheim, Germany). The end of the aqueous inlet capillary was placed in a vial containing blank solution; the end of the oil inlet capillary was placed in a vial containing PFD, and vacuum pressure was initiated and adjusted until stable

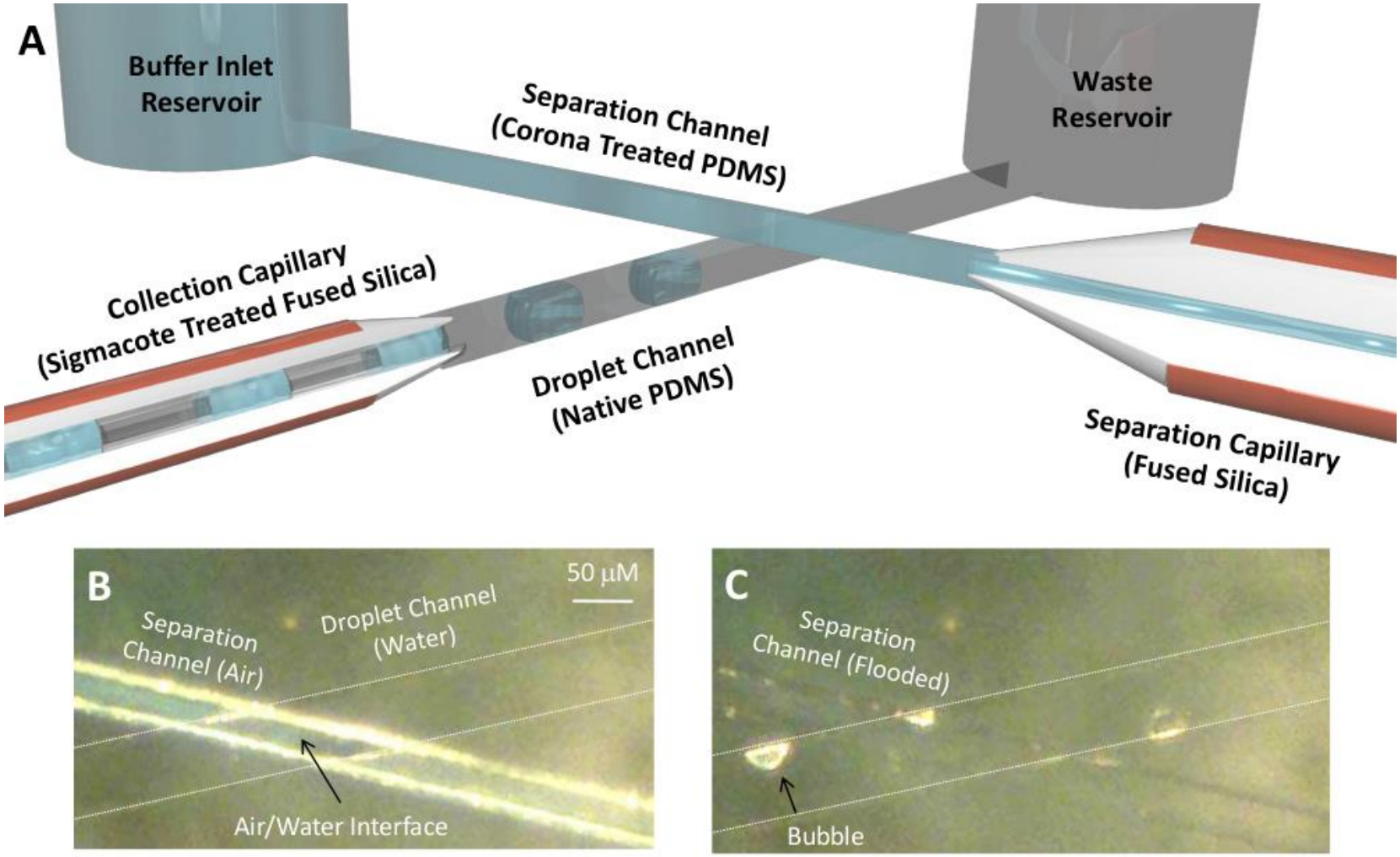

Figure 19: A simple microfluidic droplet injector that utilizes selective hydrophilic surface patterning by protection of one channel with water prior to corona treatment of the other channel. (A) A conceptual diagram of the injector. (B) An image of the corona treatment process showing the droplet channel filled with water while the separation channel is open to air and ready for corona treatment. (C) Flooding of the separation channel after corona treatment. Bubble formation after treatment is apparent.

droplet formation between 0.1 and 0.4 Hz was observed, at which point flow rates were equilibrated by forming droplets for 5 min.

After equilibration, the blank vial was switched out for vials containing each riboflavin standard solution. Vial switching was timed so as to collect 8–10 droplets of each standard, and vials were switched fast enough to avoid withdrawal of air up the aqueous inlet capillary. Roughly, 35 droplets were collected after switching to the final riboflavin standard to ensure droplets containing each standard had moved off the chip and onto the collection capillary. Special care was taken during sample collection to avoid riboflavin photolysis, which is discussed in more detail below. As soon as collection was finished, the vacuum tube was disconnected and the collection capillary containing the droplet train was removed and stored in a freezer at −30 °C until analysis.

4.2.6 **Direct Fluorescence of Droplets**

In order to assess the extent of droplet mixing prior to injection, a 5 mm detection window was made at the end of the collection capillary of a droplet formation device. Droplet fluorescence was measured directly through the collection capillary as droplets were formed using the procedures described for sample collection and the same fluorescence detection protocol described in Chapter 2.3.10. Inlet vials were switched between 15.4 and 7.64 μM riboflavin standards while forming droplets between 0.1 and 0.4 Hz.

4.2.7 **Injection and Electrophoresis**

The separation channel of the injector junction was selectively corona treated to render it hydrophilic while leaving the bottom channel hydrophobic by using a technique similar to one developed by Filla et al. (Filla et al., 2011) that uses water to guard one channel against corona treatment. Water was placed in the reservoir at the end of the droplet channel (waste reservoir), and vacuum pressure was applied at the other end of the droplet channel by pressing a tube connected to the house vacuum against

the edge of the chip. This caused water to fill the droplet channel, but because of high flow resistance, the narrow hydrophobic separation channel remained filled with air (Figure 19B). A wire leading to a BD-20ACV Laboratory Corona Treater, 230 V (Electro-technic products, Chicago, IL), was placed in the reservoir at the end of the separation channel (buffer inlet reservoir), and the corona treater was turned on. As soon as an electric arc went up the separation channel, it was rendered hydrophilic and flooded with water (Figure 19C). This typically happened within one second of turning on the corona treater. At this point, the corona treater was turned off and the junction was emptied of water using the house vacuum. This surface treatment procedure was extremely convenient, could be performed in less than 5 min, and only required a hand-held corona treater, which is readily available to many facilities which fabricate PDMS devices.

The hydrophilic separation channel was filled with 15 mM (pH 8.8) sodium tetraborate background electrolyte (BGE) while leaving the hydrophobic droplet channel empty by applying moderate pressure to a BGE-filled syringe connected to the end of the separation capillary. The droplet channel was then filled with PFD by placing several drops of it in the waste reservoir, which immediately caused the hydrophobic droplet channel to flood with PFD. Platinum electrodes were placed in the buffer inlet reservoir and in a buffer outlet vial located at the end of the separation capillary. The buffer inlet reservoir electrode was grounded, and the buffer outlet vial electrode was connected to a Spellman CZE 1000R high voltage power supply purchased from Spellman High Voltage Electronics (Hauppauge, New York).

The thawed collection capillary was installed at the droplet inlet branch of the injector junction (Figure 21A). The stainless steel adapter was connected to 1/32 in. tygon tube which lead to a pressure reservoir made from a side arm flask and two-hole rubber stopper. The arm of the flask was connected to house air and one of the stopper holes was connected to the tygon tube, with the other stopper hole left open. The side arm flask was filled with enough water to allow the end of the tygon tube to be below the

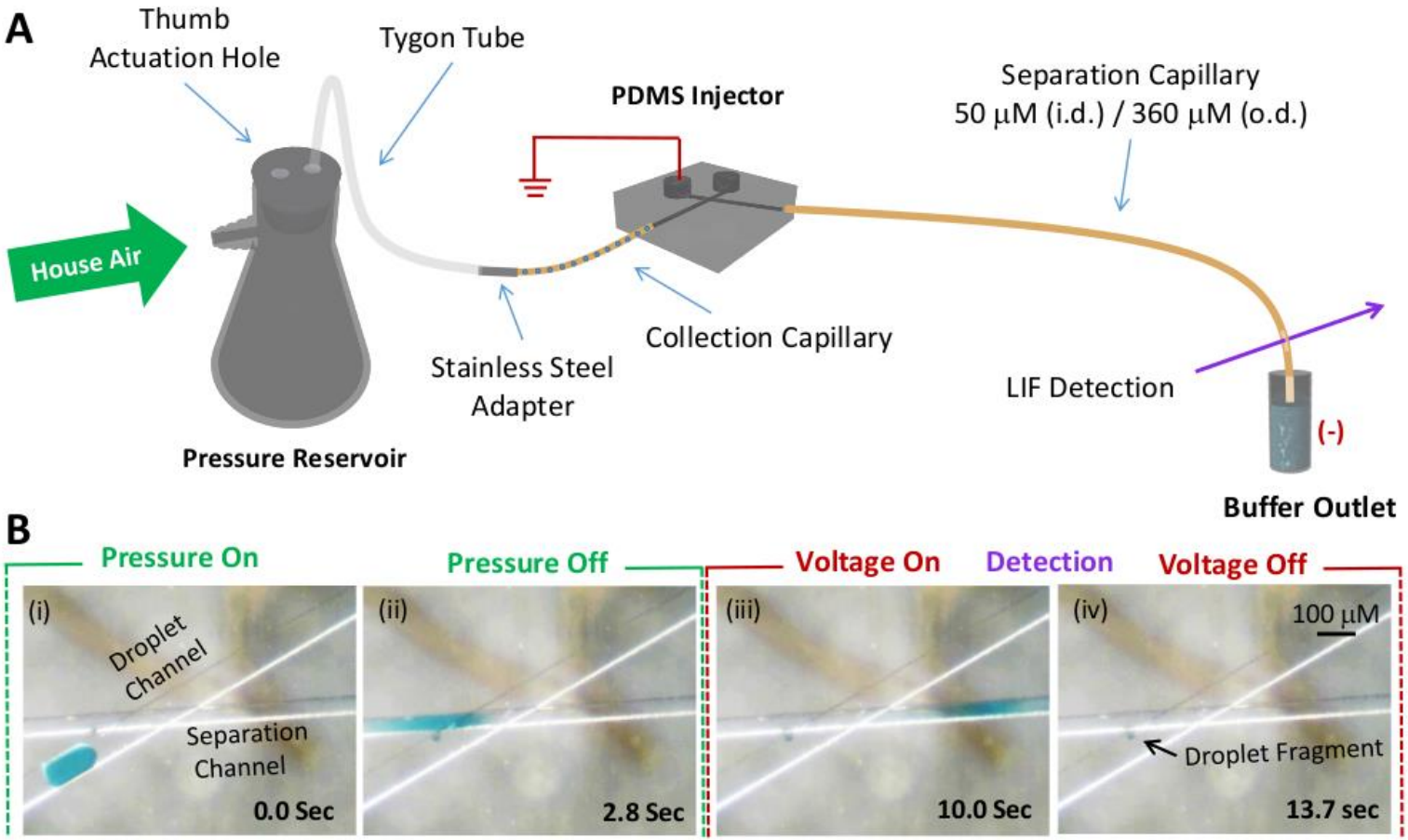

Figure 20: On-demand injections of individual droplets are made by moving the droplet train with a pressure reservoir made from a side-arm flask. The pressure reservoir has a thumb-actuation hole which allows the droplet train to be started and stopped with no noticeable drift in flow. (A) A schematic of the injector interfaced with the pressure reservoir, separation capillary, and LIF detector. (B) Time-lapse images of a droplet (died blue) being injection into the separation channel and mobilized onto the separation capillary. (i) Pressure is applied and the droplet approaches the separation channel. (ii) The droplet reaches the separation channel and enters it, leaving a visible blue injection zone. Pressure is turned off to stop the droplet train. (iii) Voltage is turned on and the injection zone begins to move towards the separation capillary. Data acquisition for LIF detection is started. (iv) The injection zone leaves the field of view and enters the capillary. A fragment of the injected droplet is visible. After the 3.5 minute separation is complete voltage is turned off, data acquisition is ended, and the next droplet may be injected.

water level. This allowed pressure to be applied and cut off rapidly by placing a thumb over the open hole, allowing the droplet train to be started and stopped manually with no noticeable drift in flow. This allowed droplets to be pushed from the collection capillary into the injector junction one at a time.

As droplets were pushed into the junction, the hydrophilic surface of the separation channel pulled them out of the oil stream and into the separation channel while excluding the PFD phase. Despite the imprecise pressure control afforded by the manually actuated pressure reservoir, oil entering the separation channel of properly treated devices was never observed. This indicates that the surface treatment paired with the channel size difference provided a highly selective means of extracting droplets from the oil stream. Droplets were injected one at a time by stopping the droplet train after each injection, and a negative voltage of 27 kV was applied over the separation capillary to mobilize the injected droplet down the separation capillary. Detection through the detection window was performed using a home-built laser-induced fluorescence (LIF) detector described previously. (Piyankarage et al., 2008) After each droplet had been detected, the voltage was turned off and the next droplet was injected for subsequent analysis (Figure 21B,i–iv).

4.2.8 **Analysis of a Photolyzed Urine Sample**

A urine sample was assayed to demonstrate chemical compatibility of the injector with a biological sample and the capability of performing a chemical separation. Urine that had been previously collected for educational purposes was used in this study. Appendix A includes human testing exemption documentation. The urine collected was the first of the morning and from a subject who consumed a B-100 brand vitamin tablet containing 100 mg of riboflavin on the evening prior. Prior to droplet formation, the urine sample was left under a 150 watt microscope light to form riboflavin photolysis products. Gravimetric injections of this urine sample were performed periodically to monitor the formation of photolysis products. These injections were performed by holding the separation capillary in the urine sample and raising the urine vial to a height of 21 cm for 5 seconds.

The photolyzed urine was then mixed with 55% glycerol, and the same procedure for forming droplets of riboflavin standards was used to form a droplet train containing urine sample droplets followed by droplets of a 77.9 μM riboflavin standard, which was used for riboflavin peak identification in urine electropherograms. Droplets were injected using the same injection protocol used for riboflavin standards.

4.2.9 **Data Analysis**

Raw data was imported to Microsoft Excel for plotting of electropherograms and calibration curves, to perform linear regression, and to perform calculations relating to theoretical plates and limits of detection. Because of significant peak asymmetry, theoretical plates were calculated using the Foley-Dorsey equation. (Foley and Dorsey, 1983) To measure droplet volume, video of droplets passing through the collection capillary was captured and loaded into Toupview, an image analysis program with a pixel measurement tool. Using the o.d. of the collection capillary as a scale, dimensions measured in pixels were converted to micrometers. The volume of each droplet was then calculated approximating the droplet shape as cylindrical.

4.3 Results and Discussion

4.3.1 **Viscosity Modification**

Initial attempts at forming droplets from pure aqueous samples of riboflavin without the addition of a viscosity modifier resulted in unstable droplet formation. Droplet formation would be possible in the beginning stages of the experiment, but as the collection capillary filled with droplets, the frequency of droplet formation would slow dramatically until it eventually halted. The vacuum pressure was ramped up as the collection capillary was filling with droplets in an attempt to prevent droplets from stalling, but the full intensity of the vacuum pump (730 Torr) was not sufficient to prevent the eventual stalling of the flow. Because driving pressures exceeding atmospheric pressure cannot be achieved using only vacuum,

this places a fundamental limitation on scaling droplet platforms down when using vacuum-driven flow alone.

It has been reported in the literature that droplets traveling in a flow stream contribute significantly to flow resistance and drastically increase flow-based pressure drops across a capillary. (Groß et al., 2008) The increase in pressure due to the presence of droplets in the flow stream depends on the number of droplets, their viscosity, the flow rate, and the i.d. of the capillary. It has been found that this increase in flow resistance is due in part to circulation of the fluid within droplets, which can be limited by increasing the viscosity of the aqueous phase. Surprisingly, this means increasing the viscosity of the aqueous phase actually decreases the flow-based pressure drop across the capillary containing the droplet train, which helps to stabilize droplet formation frequency as the capillary fills with droplets. After 55% (wt/wt) glycerol was added to the riboflavin standards to increase their viscosity, highly regular droplet formation was observed and could be sustained for periods of time exceeding 1 h.

4.3.2 **Injection Volume and Precision**

Because the droplet-based injector presented does not desegment prior to injecting droplets, the injection volume and reproducibility depends on the volume and standard deviation of droplets formed by the T-junction. The average droplet volume generated by the device was found to be 750 pL with a 2% RSD. This variance in droplet volume becomes the variance in injection volume after the droplet is injected and is similar to previous reports. (Theberge et al., 2010)

4.3.3 **Injection Visualization**

In order to ensure injection volumes were entirely delivered to the electrophoresis channel for separation without mixing, which is necessary for optimal detectability and temporal resolution, injections were visualized by forming droplets of blue food coloring and injecting them using the same injection procedure developed for riboflavin samples. Figure 21B, i–iv shows images taken from a video of

injections. From the video it is apparent that aqueous sample flows around the corners of the junction space where surface area and therefore wetting is maximized. To prevent droplets from flowing over the right and left corners simultaneously, which would split the injection zone in half and leave a region of run buffer between the two injected zones, the droplet and separation channels were angled slightly off from a 90° intersection. This caused each droplet to reach one corner before the other, at which point injection occurred entirely through that corner to form a single injection zone. This is evident in the video, as the injection zone appears toward the side of the junction with the corner closest to the incoming droplet train.

After droplets were injected, the voltage was turned on to visualize electromigration of the injected zone while uninjected droplets remained stationary. The video also revealed a small fragment of the droplet breaking off and staying in the droplet channel after injection and electromigration (visible in Figure 21iv). This phenomenon was observed consistently in all devices as a small blue patch left behind at the corner where the droplet injected through and is potentially a source of droplet mixing. The likely cause of droplet breakup is inconsistent surface patterning near the boundary where the two channels intersect. As shown in Figure 19B, bubble formation is typically seen in the junction after corona treatment. This indicates water guarding the droplet channel from corona treatment may boil in the junction, which could allow corona treatment to reach the droplet channel, rendering parts of it hydrophilic.

As the injection zone passes under the oil channel, it also appears to become slightly deformed and dispersed. This may indicate that the oil/water interface between the channels protrudes slightly into the separation channel, which would cause a slight constriction in the channel directly under the droplet channel. It may also be due to a rapid separation of the negative Brilliant Blue FCF dye molecules from the neutral glycerol zone, which is visible due to a refractive index difference between the relatively high concentration of glycerol and the run buffer.

4.3.4 **Riboflavin Photolysis**

To ensure riboflavin photolysis, a riboflavin solution was left out under a microscope light and gravimetric injections were performed periodically to monitor the formation of photolysis products. Figure 22 shows a series of electropherograms taken at 10 minute time intervals. In these electropherograms a single large peak, presumably riboflavin, decreases in intensity with exposure to light as two other peaks, most likely photolysis products, increase in intensity. Multiple peaks were also present in electropherograms of riboflavin standards injected using the droplet injector (Figure 23) when droplet formation was performed under the 150 watt microscope light. This is not surprising considering the photolysis of riboflavin. Riboflavin photodegrades when exposed to visible light to form formylmethylflavin, carboxymethylflavin, lumiflavin, and lumichrome, (Ahmad and Rapson, 1990) which along with riboflavin explains the five peak pattern observed.

At the pH of the BGE run buffer (8.8) carboxymethylflavin is charged, but riboflavin and the other photolysis products are neutral. The separation of these neutral compounds is possibly due to formation of charged borate complexes (Ahmad et al., 2008) similar to carbohydrate separations. To prevent photolysis of riboflavin standards the room lights were turned off, red light filters were placed over the microscope light, and the intensity was kept as dim as possible. After taking these precautions a single large peak was observed in the electropherograms of injected riboflavin standards as seen in Figure 24, indicating sufficient prevention of riboflavin photodegradation.

4.3.5 **System Calibration and Determination of Temporal Resolution**

Calibration of the system and estimation of temporal resolution capabilities were performed simultaneously by using the droplet trains containing a series of step changes in riboflavin concentration

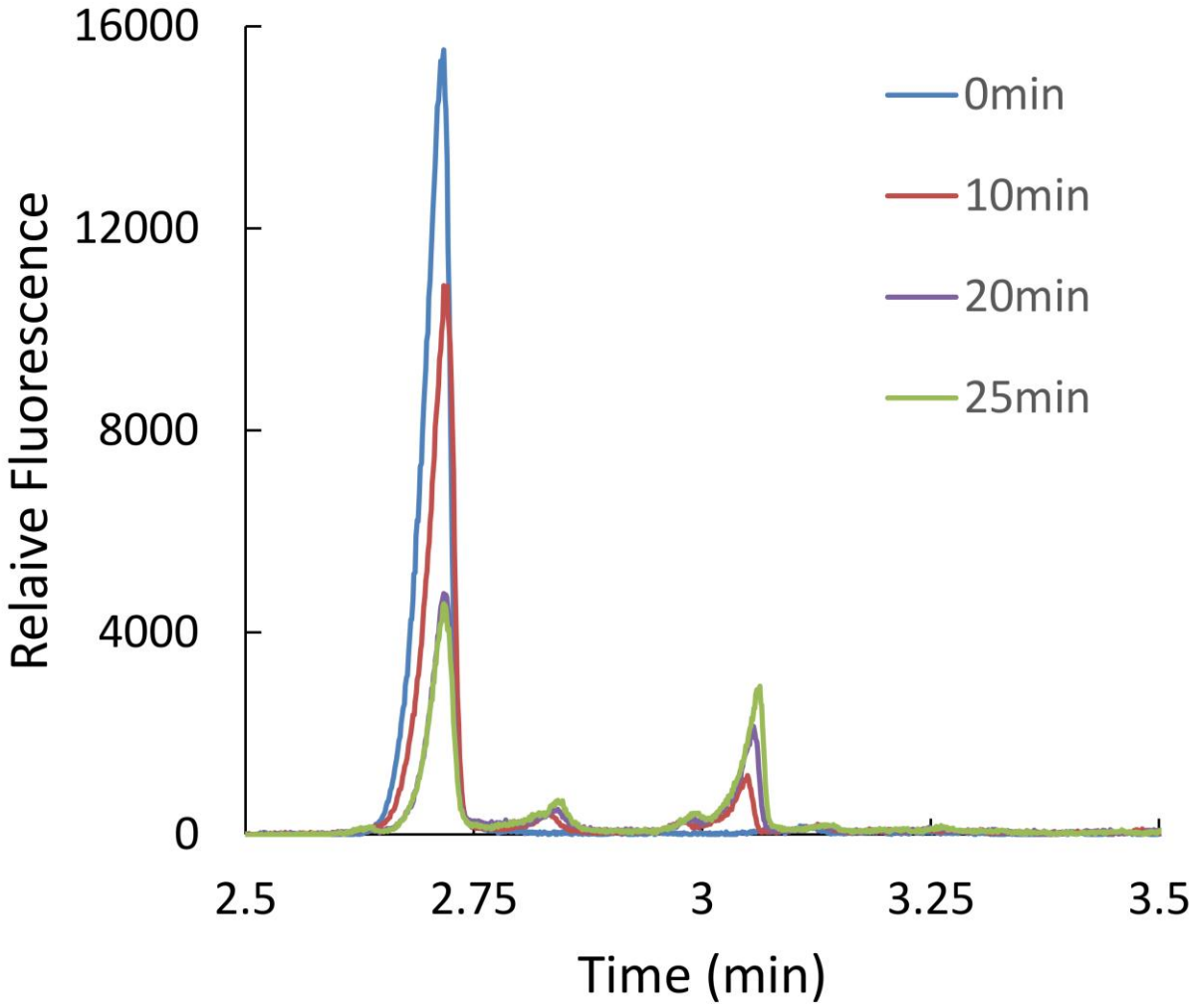

Figure 22: Electropherograms of a urine sample taken periodically during photolysis under a 150 watt microscope light. A large peak initially present, presumably riboflavin, decreases in intensity as photolysis products increase in intensity. The separation was done on a 60 cm long fused silica capillary (46 cm to detection window) with a 50 μm i.d. and 360 μm o.d. using 15 mM (pH=9.0) borate as a BGE and a 433 v/cm field strength, using gravimetric injection.

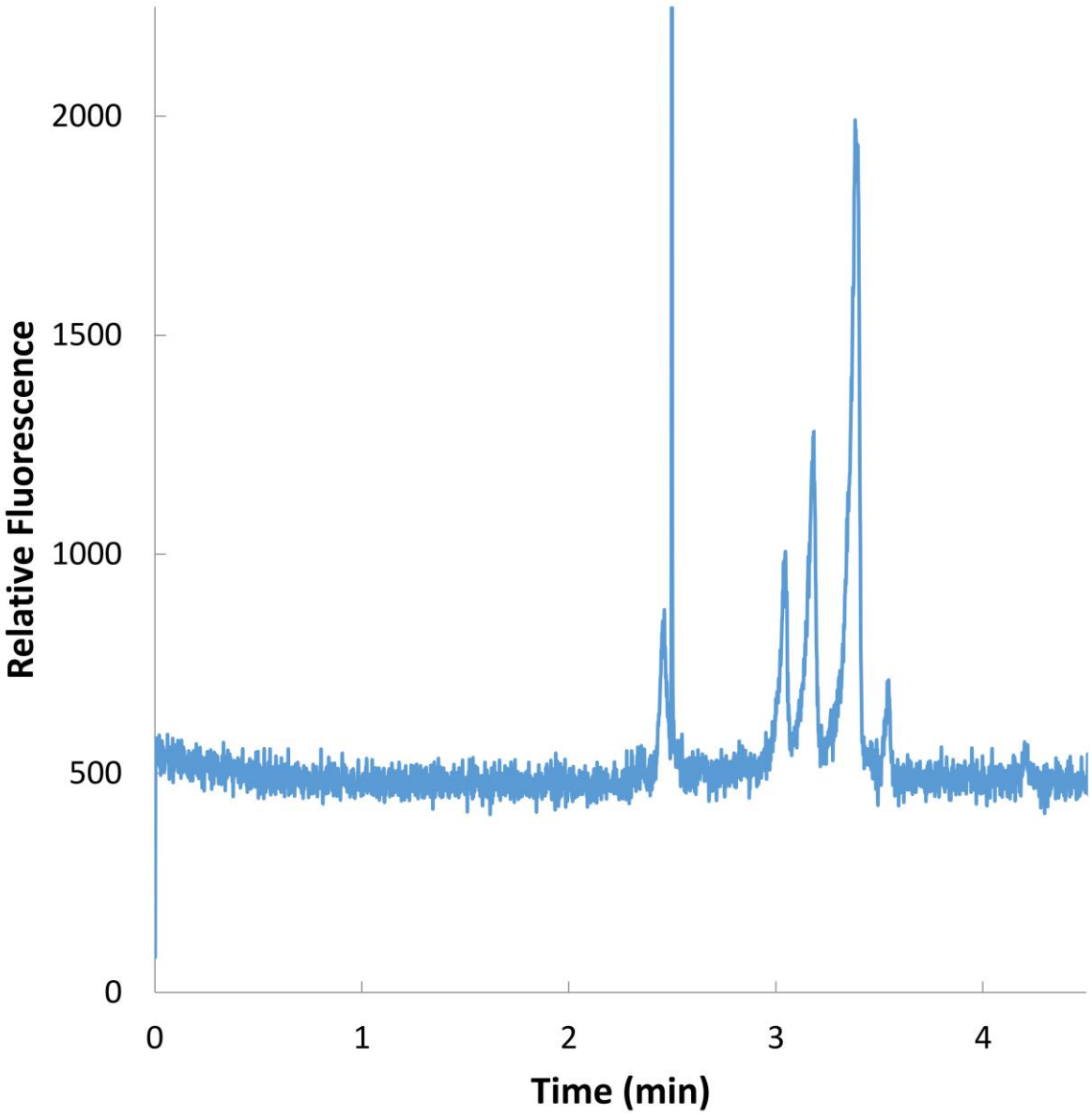

Figure 23: An electropherogram of an injected riboflavin droplet degraded by the intense microscope light. The separation was done on a 60 cm long fused silica capillary (46 cm to detection window) with a 50 μm i.d. and 360 μm o.d. using 20 mM (pH=9.0) borate as a BGE and a 433 v/cm field strength. Multiple peaks are likely due to the presence of photolysis products.

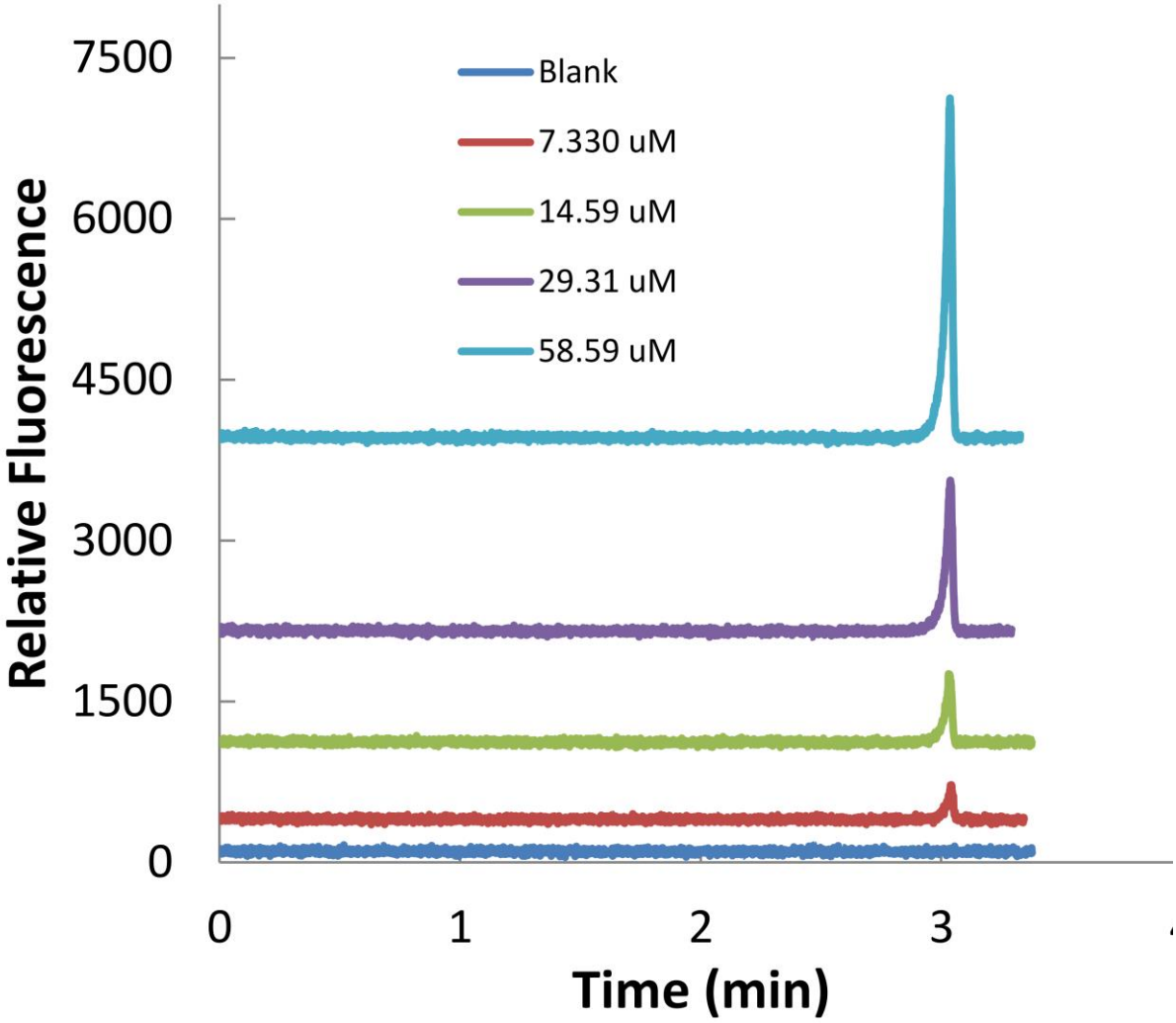

Figure 24: Representative electropherograms of injected droplets containing riboflavin standards. Separations were done in a 60 cm long fused silica capillary (46 cm to detection window) with a 50 μm i.d. and 360 μm o.d. using 15 mM (pH=8.8) borate as a BGE and a 450 v/cm field strength.

which had been prepared and frozen previously. Droplets containing each riboflavin standard were identified by first determining the riboflavin peak height corresponding to individual droplet electropherograms, as shown by the representative electropherogram in Figure 24. The peak heights of riboflavin standards injected with three separate injectors exhibited %RSD values between 4.4% and 4.8%, which is acceptable considering the variance contributed by the 2% variability in injection volume.

Next, riboflavin peak height was plotted vs the relative time of droplet formation, as shown in Figure 25A. These data clearly show regions for each standard concentration with similar riboflavin peak heights. These regions or "steps" were identified by looking at the plot, and the mean riboflavin peak height for each step was calculated. Droplets between steps exhibited intermediate riboflavin peak heights, most likely due to diffusive mixing of riboflavin standards in the aqueous inlet capillary prior to droplet formation and also because of the droplet fragment left behind after each injection. An average of 1.8 ± 0.5 ($n = 8$) intermediate droplets existed between steps. These intermediate data points were excluded from the mean riboflavin peak height calculation of the nearest step if the riboflavin peak height was more than two standard deviations away from the average peak height of the step.

To demonstrate a proof-of-concept for the riboflavin assay, a calibration curve for riboflavin was made by plotting the riboflavin concentration of each step vs the mean riboflavin peak height for that step (Figure 25B). The plot showed very good linearity with coefficients of determination between 0.998 and 0.999. The limit of detection (LOD, defined as a signal-to-noise ratio of 3) for riboflavin was determined to be (2 ± 1) μM at the 95% confidence interval ($n = 3$), which corresponds with detection of 2 femtomoles of riboflavin. This is significantly higher than previous reports, (Hu et al., 2007) which report LODs as low as 9 attomoles. This can be attributed to a shorter optical path length for excitation (50 μm vs. 100 μm) and the fact that our excitation laser (λ_{max}=405 nm) is not optimal for excitation of riboflavin (λ_{max} 447 nm). (Drössler et al., 2002) Regardless, riboflavin was

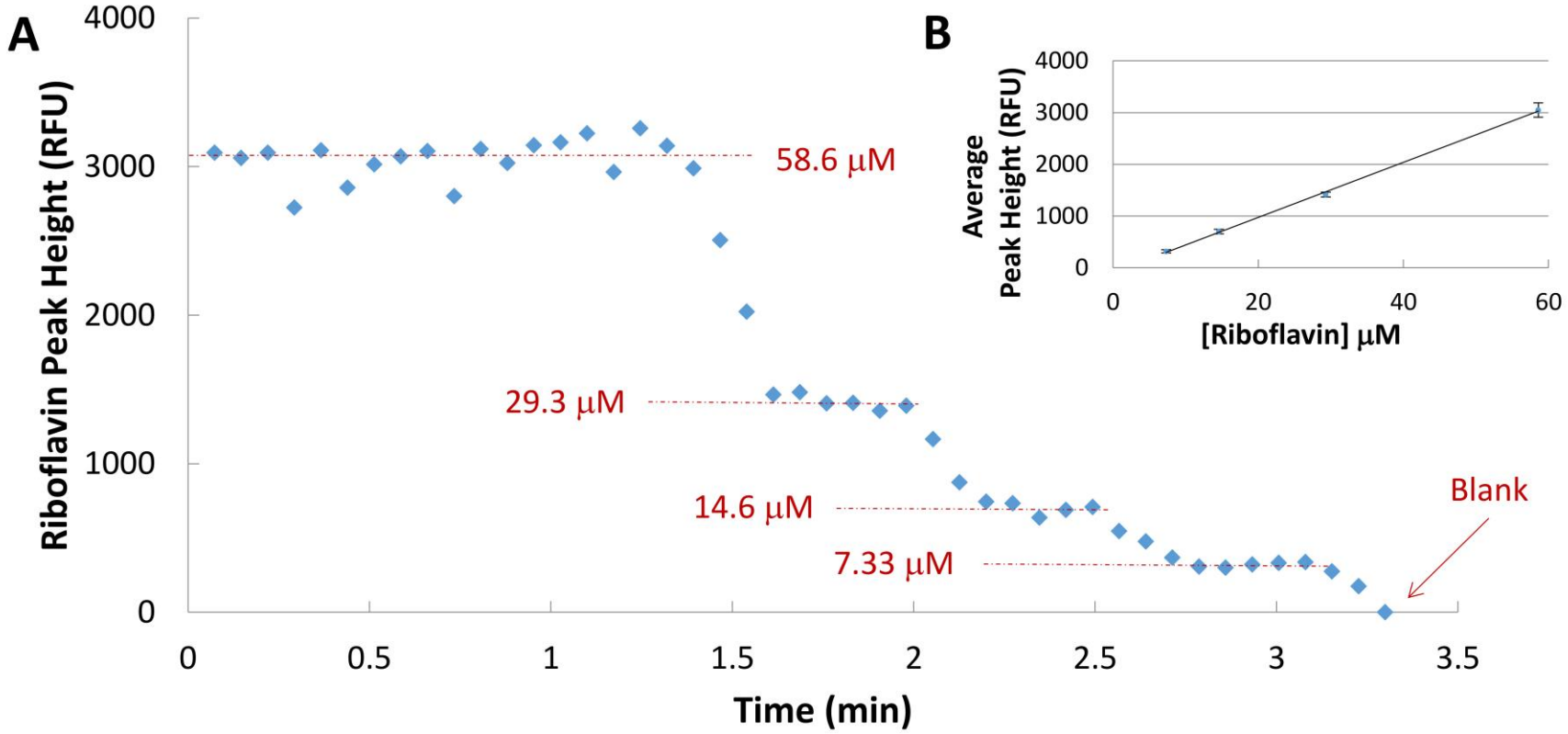

Figure 25: Switching the riboflavin standard vial at the aqueous inlet capillary during droplet generation forms regions in the droplet train containing droplets of each standard. (A) A representative plot of the riboflavin peak height in each droplet's electropherogram vs. the relative time the droplet was formed at exhibits a "step" for the region of droplets for a given standard. B) The average riboflavin peak height for each step (indicated by dashed lines in A) can be used in conjunction with the concentration of each standard to form a riboflavin calibration curve. Three different droplet trains were processed to generate three separate calibration curves. The calibration curve shown is representative. Each data point in the calibration represents the average of all points available from each step change in concentration.

a convenient standard to characterize injections because it was readily available and natively fluorescent, and demonstrates the ability to assay a biologically relevant molecule.

The calibration data may also be used to evaluate preservation of temporal resolution by formation of the droplet stream. Temporal resolution depends not only on the droplet generation frequency but also on the number of droplets over which a full change in signal is observed. To determine this, the percent change in signal between each droplet and the next droplet was calculated by finding the difference in riboflavin peak heights and dividing it by the difference in mean riboflavin peak heights of the two closest steps. A total of 3 droplets were required to see an (86% ± %4) change in signal (95% CI, n = 9) from one step to the next. The average droplet formation frequency was 0.2 Hz, which corresponds to a rise time of 15 s if a change in signal from 10% to 90% requires 3 droplets and is similar to previous reports. (Wang et al., 2009; Filla et al., 2011)

To assess how significant was the loss in temporal resolution due to droplet carry-over, the maximum size of a droplet fragment (Figure 21iv) was estimated using microscope images by comparing the cross sectional area of fragments to that of droplets and was found to be 40 pL. This assumes the droplet fragment spans the entire height of the channel, which overestimates its volume. Using a modified dilution equation, it was determined that 40 pL of mixing between 750 pL droplets would only cause a 5% loss in signal rise between droplets. If this was the only source of mixing between standards prior to injection, a full rise in signal should therefore be observed over one droplet. Considering a full rise in signal is observed over three droplets, other sources of mixing such as diffusion prior to droplet formation likely reduce temporal resolution more significantly than droplet carry-over.

To test the hypothesis that droplet mixing was primarily due to diffusive mixing of sample zones in the aqueous inlet capillary prior to droplet formation, and not due to the injection process itself, direct fluorescence detection of droplets was performed as they moved through the collection capillary of the droplet formation device (Figure 26). Using this approach, an average of 2.2 ± 0.8 (n = 9) intermediate

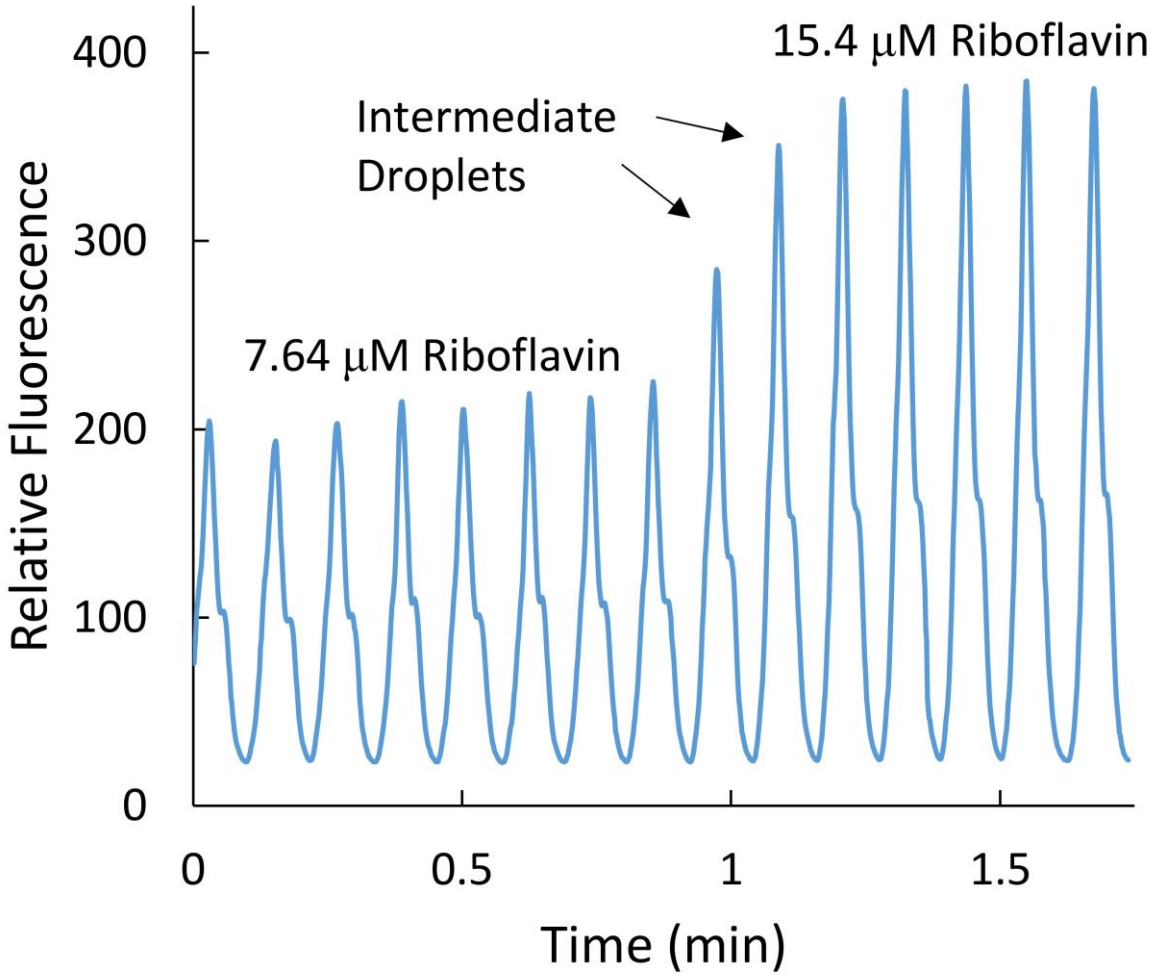

Figure 26: Direct fluorescence of riboflavin standard droplets was performed through the collection capillary during droplet formation. The number of intermediate peaks was used to characterize the extent of mixing prior to injection. The results indicate an average of 2.2 ± 0.8 (n = 9) intermediate droplets between riboflavin standard concentration step changes.

droplets were found between steps in concentration. This result is not statistically different at the 90% confidence level from the number of intermediate droplets observed during injection of droplet trains and is consistent with the premise that no significant droplet mixing occurs during the injection process.

Improvements to temporal resolution must therefore be achieved by limiting mixing prior to droplet formation. An increased sampling frequency would increase the linear velocity of sample in the aqueous inlet and reduce the time available for diffusive mixing prior to droplet formation. In addition, this would increase the sampling rate, which also improves temporal resolution. Decreasing the length of the aqueous inlet capillary would also decrease the amount of time available for diffusive mixing prior to droplet formation, which would improve temporal resolution further.

4.3.6 **System Efficiency and Reproducibility**

One concern with previously reported devices (Edgar et al., 2006; Roman et al., 2008; Filla et al., 2011) is low separation efficiency, which contributes to poor peak resolution. This can be particularly problematic when analyzing biological samples containing many detectable matrix components. Low separation efficiency is common for separations on PDMS chips, which often suffer from analyte adsorption and variable electroosmotic flow due to unstable surface properties. Wang et al. managed to achieve high efficiency by use of a glass chip. (Wang et al., 2009) PDMS devices are often more convenient to fabricate than glass devices, however, which require time-consuming chemical etching. To use PDMS while still allowing for higher separation efficiencies, a fused silica capillary was interfaced with the injector to do separation on-capillary, which has been reported in the literature previously. (Niu et al., 2013) This allowed easy and rapid fabrication of PDMS devices while still allowing separations with up to 27,000 theoretical plates for the riboflavin standards injected, which is superior to typical separations on PDMS surfaces (Vickers et al., 2006) but lower than typical separations performed on fused silica capillaries. (Lauer and McManigill, 1986)

When one looks at the electropherograms of injected riboflavin standards (Figure 24), significant peak fronting is evident, which is likely the largest contributor to low separation efficiency. Peak fronting, a problem with peak symmetry where the front of a peak is wider than the back of the peak, is likely due to electromigration dispersion, as the sample injection zone contains no ions and therefore is very different from the run buffer in ionic strength. Addition of an ionic strength buffer to the sample would likely prevent electromigration dispersion and allow for more efficient separations. Another contributing factor to zone dispersion may be dead volume between the 30 × 75 μm square separation channel and the 50 μm (i.d.) separation capillary. Decreasing dead volume between the separation channel and separation capillary by matching their dimensions more closely may further improve separation efficiencies in future designs. One final contributor to poor separation efficiency may be the large disparity in the viscosity of the run buffer and injection zone. This has been shown to cause band broadening in chromatographic separations in the form of viscous fingring, a form of mixing that occurs at an unstable interface between two fluids of different viscosities. (Shalliker et al., 2007) Designing geometries of future droplet formation devices to alleviate backpressure during sampling could eliminate the need for addition of viscosity modifiers to samples.

Reproducibility is one concern with complicated architectures, as more intricate designs contain more working parts which can malfunction. The simplicity of this device design led to a very reproducible injection process, and although manual injection of each droplet is somewhat inconvenient, techniques exist for automated control of droplet motion (Langelier et al., 2009) and could easily be adopted for automated processing in future designs. Our design provided reproducible enough operation to allow three riboflavin calibrations involving up to 50 consecutive injections each to be performed with three separate devices on three separate days.

4.3.7 **Injection of Human Urine**

To fully demonstrate this sampling approach with a biological sample, riboflavin peaks were identified in the electropherograms of injected urine droplets by taking advantage of the fact that sample mixing occurs prior to droplet formation. Figure 27 shows the electropherograms of an injected riboflavin standard droplet and a urine droplet from the same collection capillary, along with one of the intermediate droplets from between the two samples. This intermediate droplet is effectively a urine sample spiked with a riboflavin standard and can be used for identification of the riboflavin peak in the urine electropherogram. Figure 27 also shows the successful baseline separation (R_s = 2.3) of riboflavin from a photolysis product, which was also seen in gravimetric injections of urine (Figure 22).

One large concern when surface properties of a device are important for operation is fouling by components within samples. This can alter surface properties and adversely affect device operation, limiting practical usefulness. Urine samples were successfully injected using our device without any adverse effect, which demonstrates the potential for practical use of our injector with some biological samples. Samples containing high levels of proteins may prove more challenging with respect to surface fouling and will likely require additional surface modification, such as surface fluorination.

4.4 Conclusions

In this report, a proof-of-concept for a new droplet injector is demonstrated capable of delivering droplets from a droplet train into a capillary for electrophoretic analysis without desegmentation. This design performs similar to previously reported designs but is made from only two straight PDMS channels, uses a convenient surface-patterning technique, and requires no additional working parts such as valves or membranes which previous devices require. This greatly simplifies the fabrication process and allows for very consistent, robust, and rugged operation, as fewer design steps and working parts reduces the number of problems likely to occur during fabrication and use of the device. A method of

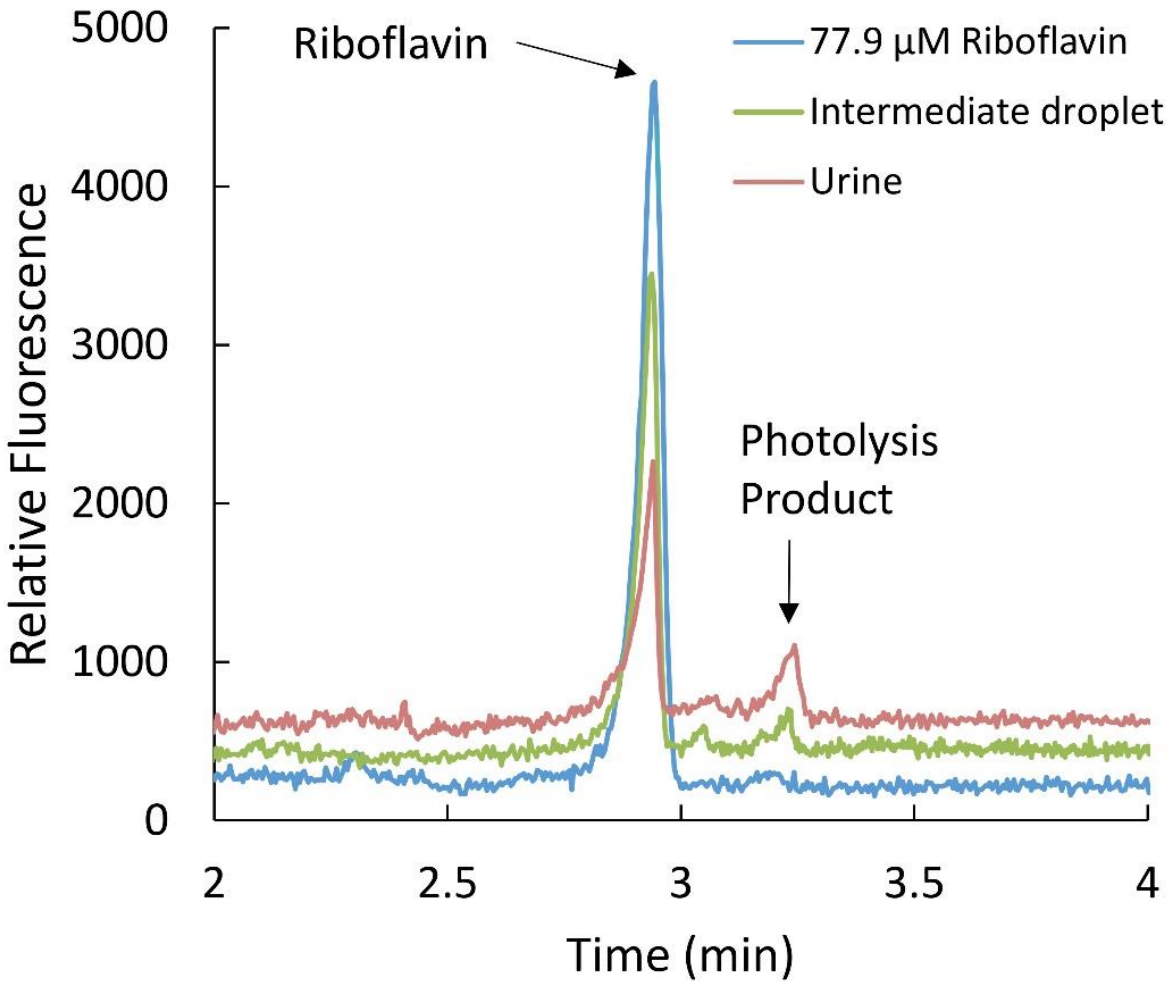

Figure 28: Representative electropherograms from a droplet train containing droplets of photolyzed human urine and droplets of riboflavin standard. Intermediate droplets were used as an effective spike for riboflavin peak identification.

reducing the backpressure over microfluidic chip platforms is also presented which uses viscosity modification. This method could help extend pressure-based limitations on downscaling devices. Although the current design requires manual injection of each droplet, future systems could be automated to require less user-intervention. The simplicity of the design could also allow for injectors to be built using nontraditional fabrication techniques similar to reports (Burgoyne et al., 2010) that use fused silica capillaries as molds to form channels in PDMS without photolithography. Fabrication by nontraditional means could help expand their use and will be a topic of future research.

5. Future Directions

5.1 Measuring Viscosity of non-Newtonian Fluids at Variable Shear Rate

The viscosity of many substances is not constant with $\dot{\gamma}$. These fluids are termed non-Newtonian. Non-Newtonian fluids can either be shear thickening, where viscosity increases with $\dot{\gamma}$, or shear thinning, where it decreases with $\dot{\gamma}$. In either case changes in viscosity that occur with variations in $\dot{\gamma}$ are caused by changes in structures occurring at the molecular level. For example, surfactant solutions often exhibit non-Newtonian behavior because micelles have the potential to deform under shear stress, which in turn changes system viscosity. (Rogers et al., 2014) Shear has also been shown to affect the quaternary structure of proteins, causing irreversible aggregate formation. (Maa and Hsu, 1997) Because many fluids exhibit non-Newtonian viscosity, measuring the shear-dependence of fluid viscosity is especially important when characterizing a material or system.

To demonstrate the ability to perform variable $\dot{\gamma}$ experiments with the viscometer presented in Chapter 2.3.2, the viscosity of a 3% (%wt/wt) PFO solution in PFD was measured at varying shear rates. As stated in Chapter 3.4.2, this viscometer is more suitable for variable shear experiments because the calibration is independent of the absolute oil and aqueous flow rates. This allows for viscosity to be measured at variable flow rate without the need for recalibration between each change in flow rate. A viscometer with a 30 cm oil inlet and 10 cm aqueous inlet was used and $\dot{\gamma}$ was varied by the same method used for measuring α at variable vacuum pressures described in Chapter 2.3.6. Viscosity at each $\dot{\gamma}$ was determined by measuring α for pure PFD and for the 3% PFO solution while using the same glycerol solution (40%) for both α measurements. Given the known viscosity of PFD, the viscosity of the 3% PFO phase could then be calculated for each $\dot{\gamma}$ using eq 2.10.

A plot of the viscosity of 3% PFO in PFD (wt/wt) vs. $\dot{\gamma}$ (Figure 29) indicates non-Newtonian behavior. From the plot it is evident that the viscosity of a 3% PFO solution increases with shear rate (shear thickening), which is known to occur in solutions containing wormlike micelles. (Castillo-Tejas et al., 2011) The experiment was repeated three times, and a decrease in viscosity around $\dot{\gamma} = 300\ s^{-1}$ was seen in all experiments. This feature may be caused by shear stress-induced changes in micellar structure. Stable droplet formation was possible with oil phase shear rates between 100 and 900 s^{-1}. Figure 29 also demonstrates the importance of using a Newtonian fluid as the oil phase when measuring aqueous phase viscosity. The observed change in oil phase viscosity with changes in $\dot{\gamma}$ means the slope of the calibration, which depends on oil viscosity, would change with $\dot{\gamma}$. The viscometer presented in Chapter 3 has a calibration which is independent of the oil phase viscosity, making it much more suitable for applications requiring a non-Newtonian oil phase. Future works will explore the potential of the viscometer for additional applications in characterization of non-Newtonian fluids and will also investigate accuracy and precision of the design when working with non-Newtonian fluids.

5.2 Droplet Injector as an Interface for Comprehensive Two-Dimensional Separations

5.2.1 Introduction

The complex nature of some samples often makes comprehensive characterization extremely challenging. Biological samples, for example, can easily contain more than 10,000 unique compounds. The polymeric nature of many classes of biomolecules such as nucleic acids, proteins, and carbohydrates adds an additional challenge to sample characterization because all molecules of a given class have very similar physical properties. This means a powerful separation technique is often required to isolate individual sample components before detection. Consequentially, two-dimensional separations are routinely used in proteomics, genomics, metabolomics, and other fields where complete characterization of a biological sample is desired.

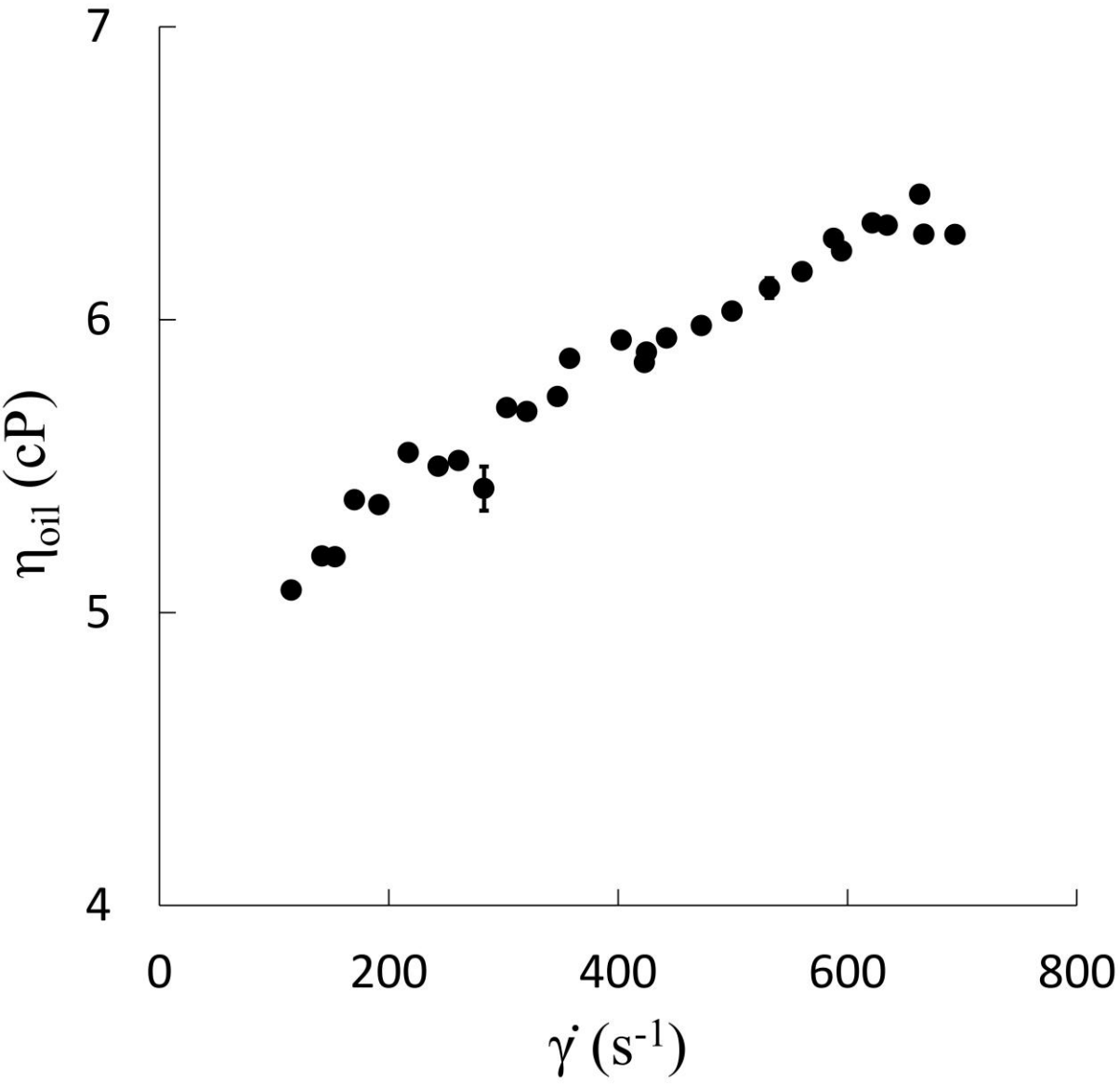

Figure 29: The viscosity of a 3% PFO solution in PFD (wt/wt) measured at varying shear rates. Measurements were performed at 26 °C. The 3% PFO solution is non-Newtonian and appears to exhibit shear thickening behavior. Each viscosity was measured in triplicate. A dip in viscosity around 300^{-1} was observed in all trials (n=3) and is possibly indicative of a shear-induced phase transition in micelle structure. Each viscosity measurement represents the average of 5 measurements.

In a two-dimensional separation two orthogonal separation techniques, such as LC and CE, are used in sequence to greatly improve peak capacity. Ideally, sample components which are separated poorly in the first dimension are separated based on a different mechanism in the second dimension. Assuming the methods are entirely orthogonal, the peak capacity is the product of the individual peak capacities of the two dimensions. If the second dimension separation is fast enough to be performed online then the overall separation requires no more time than the first dimension separation. This permits improvements in peak capacity of orders of magnitude without increasing analysis time.

Coupling separation techniques online presents some challenges, however. Often separation efficiency in the second dimension is sacrificed because of time constraints placed on it by the first dimension. One means of decreasing second dimension separation time without sacrificing too much efficiency is by scaling the separation down. This enhances efficiency by improving mass transfer in chromatographic separations and allows for higher field strengths without excessive joule heating in electrophoretic separations. Scaling a separation technique down, however, requires injection volume to be scaled down. This is necessary to avoid peak broadening associated with injection volumes large in comparison to the total column volume. Because the second dimension must be the faster of the two dimensions in an online separation and is often designed at a smaller scale, it is often impossible to inject all eluent exiting the first dimension. To address this problem the eluent stream from the first dimension is often split and only a portion of it is injected for second dimension analysis, which leads to a loss in analyte and therefore loss in sensitivity.

Capillary electrophoresis is an ideal choice for a second dimension in two-dimensional separations because it is fast and orthogonal from most chromatographic techniques. For these reasons it has been widely used with LC. (Moore and Jorgenson, 1995; Hooker and Jorgenson, 1997; Lewis et al., 1997; German et al., 2001; Chambers et al., 2011) The ability of droplets to preserve the resolution of chromatographically separated bands has also been demonstrated (Edgar et al., 2009), making droplet

microfluidics an interesting means of storing, handling, and processing fractions from the first dimension. Surprisingly few droplet interfaces for LC-CE have been reported (Niu et al., 2009; Ye et al., 2015), however, and both of these were extremely time consuming offline techniques (>140 hours). An online droplet technique for coupling LC to CE for two dimensional analyses could utilize an array of droplet techniques discussed in Chapter 1.3.3 to prepare sample for the second dimension, but would be much faster than offline techniques.

5.2.2 **Experimental**

Bis-tris was obtained from Sigma Aldrich (St. Louis, Mo) All other materials and chemicals were obtained as described in Chapter 3.3.1. The droplet injector described in Chapter 3 was scaled up to test the possibility of utilizing it for delivery of eluent from a capillary LC column to a capillary for separation by CE. Junctions were constructed via capillary molding in PDMS. PDMS was mixed with curing agent in a 10:1 ratio by mass, poured into a glass dish, and cured on a hotplate at 100 °C. A 150 μm o.d. capillary was placed on the surface of this PDMS with a 90 μm o.d. capillary placed on the surface of the PDMS resting over top of the 150 μm capillary to form a droplet channel (150 μm i.d.) and electrophoresis channel (90 μm i.d.) as shown in Figure 30A. A 360 μm o.d. capillary was positioned perpendicular to the 150 μm o.d. capillary to make a T-junction (as descried in Chapter 3.3.2) built into the droplet channel. Tapers were also added to the ends of the droplet channel and electrophoresis channel for interfacing them with 360 μm o.d. capillaries. A small amount of epoxy was applied at the T-junction and at the point the 150 μm o.d. capillary touched the 90 μm capillary, and then PDMS was poured over the top and cured at 100 °C. This ensured a connection existed between the droplet channel and electrophoresis channel.

On removing capillaries oil waste and buffer inlet reservoir holes were punched into the PDMS. A 10 cm length of 360/75 μm o.d./i.d. capillary (separation capillary) was interfaced with separation

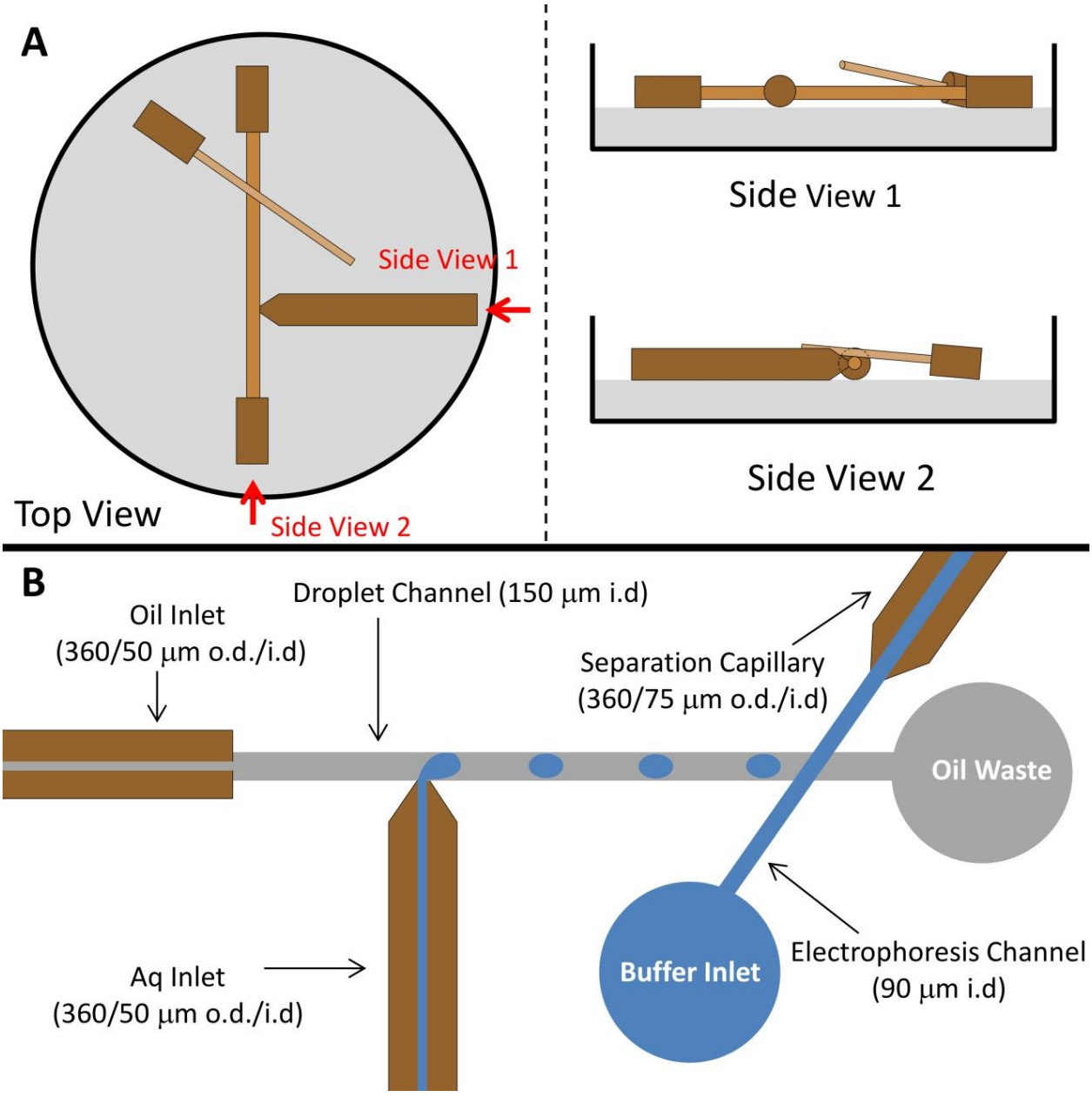

Figure 30: Construction of a droplet injector with built in T-junction for droplet generation. (A) Capillary molds are used to form the droplet channel, electrophoresis channel, and T-junction. Tapers are included on the ends of the droplet channel and electrophoresis channel for interfacing the injector with 360 μm o.d. capillaries. (B) An oil inlet, aqueous inlet, and separation capillary are interfaced with the injector. Reservoir holes are also punched into the PDMS at one end of the droplet and electrophoresis channels.

channel, as shown in Figure 30B. Capillaries (360/50 μm o.d./i.d.) were installed at the oil inlet end of the droplet channel (oil inlet) and perpendicular branch of the T-junction (aqueous inlet). The oil inlet capillary was interfaced with a PHD 2000 syringe pump loaded with a 0.5 μL syringe filled with PFD and the aqueous inlet capillary was attached to a 1 mL plastic disposable insulin syringe filled with an aqueous solution of blue food coloring. The separation channel was corona treated as described in Chapter 3.3.3 and filled with a BGE containing 20 mM bis-tris. Approximately 3 nL droplets were formed on demand by delivering PFD to the droplet channel at 1 μL/min with the syringe pump and controlling the plunger of the aqueous inlet syringe by hand. A field strength of 3000 v/cm was applied with a Spellman CZE 1000R high voltage power supply.

5.2.3 **Results and Discussion**

The scaled up junction was found to work similarly to the injector described in Chapter 4 and had no problems with oil entering the electrophoresis channel. As seen in Figure 31, droplets formed at the T-junction immediately moved down the droplet channel and were injected into the electrophoresis channel. Voltage was kept on throughout the experiment, so droplets injected into the buffer stream were immediately mobilized onto the separation capillary. If a capillary LC column was inserted into the T-junction, eluent from the end of the column could be used to form droplets, which could then be injected and separated by CE. Previous reports of an offline droplet interface for LC-CE (Ye et al., 2015) utilized 40 nL droplets. These droplets were greater than 5% of the separation capillary volume, which lead to excessive band broadening in the second dimension. The 3 nL droplet injections achieved here are less than 1% of the separation capillary volume (440 nL), which means broadening due to the injection volume should be negligible.

Adequate sampling of eluent from the first dimension is especially important in two-dimensional separations. In order to prevent resolution loss, chromatographic bands from the first dimension should be

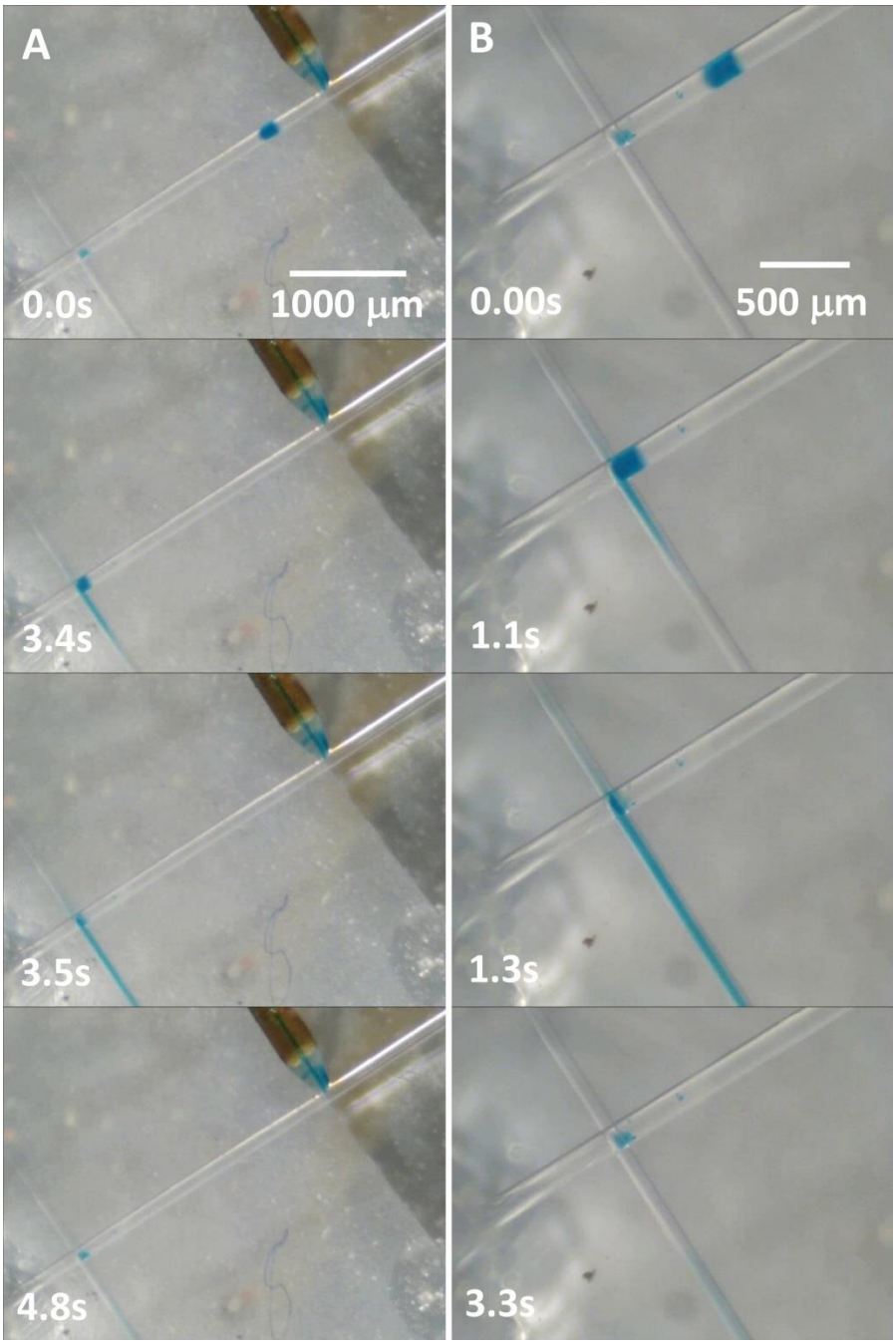

Figure 31: Images captured from video of injection events. (A) Droplets formed at a T-junction travel down the 150 μm i.d. hydrophobic droplet channel and are injected into the 90 μm i.d. hydrophilic electrophoresis channel. Voltage is applied continuously to mobilize droplets immediately as they are injected. (B) Close up images of an injection event.

sampled at least three times by the second dimension. Most online CE separations are therefore less than a minute, with some as fast as 1.5 seconds reported. (Moore and Jorgenson, 1995) To achieve a 1.5 second separation Moore et al. used a field strength of 2,500 V/cm and effective separation length of only 6 cm. A 10 μm i.d. separation capillary was required to avoid excessive joule heating in this report. The use of a low conductivity buffer is another way of preventing excessive joule heating. Bis-tris is a buffering agent similar to many Good buffers commonly used in biochemistry. Because of its large mobility, bis-tris has a particularly low conductivity, (Kelly et al., 2002) which allowed field strengths up to 3,000 v/cm to be applied over a 75 μm i.d. capillary without any detectible current or joule heating. The injector junction was also compatible with this field strength, and showed no signs of arcing or adverse effects due to the high field strength.

Capillary LC separations performed on 75 or 50 μm i.d. capillaries commonly use eluent flow rates of 50-200 nL/min. With a 3 nL droplet volume this would translate to a droplet frequency between 3.6 and 0.9 s^{-1}. With an online second dimension where all first dimension eluent was injected this would necessarily be the injection frequency for the second dimension. In order to separate droplets as fast as they were injected separation times would also need to be between 3.6 and 0.9 seconds. Considering previous reports achieved separations of peptides in 1.5 seconds at 2,500 v/cm field strengths (Moore and Jorgenson, 1995) it seems reasonable that our system could perform separations of tryptic digests and other interesting analytes within this time frame. If so, this would allow a comprehensive two-dimensional separation where all eluent from the first dimension was injected and separated in the second dimension, which would avoid a loss in sensitivity associated with splitting of the eluent stream after the first dimension.

5.2.4 **Conclusions**

The injector presented in Chapter 4 was scaled up to accommodate larger volume droplets. Corona treatment of this junction allowed for injections without any problems of oil entering the electrophoresis channel. It is also demonstrated that the junction can be fabricated using capillary molding rather than photolithography, owing largely to the simplicity of the design. This could allow use of the device by groups who do not have access to expensive photolithography techniques. Future work may explore the possibility of fabricating similar injectors out of different materials such as hard plastics or glass via micromachining. The use of bis-tris is also reported to achieve high field strengths over a short separation capillary with large diameter without excessive joule heating. This allows for the injection of entire 3 nL droplets without excessive band broadening due to injection volume, and could allow for rapid electrophoresis separations. Finally, the integration of a T-junction into the droplet channel of the injector is reported, which could allow for online coupling of LC to CE for future applications in two-dimensional separations.

6. Conclusions

The field of microfluidics has recently seen the sort of breakthrough success that other technologies, such as the integrated circuit, have experienced in the past. The ability to move fluids on a small scale in an automated fashion has the potential to revolutionize a large number of disciplines by reducing the cost associated with traditional handling techniques for wet chemistry. Considering the increasingly cross-disciplinary nature of science and engineering, new and exciting possible applications for microfluidics seem endless. Droplet microfluidics is perhaps one of the most interesting microfluidic techniques, and demonstrates the raw potential of microfluidics better than perhaps any other microfluidic technique.

Despite the exciting potential of microfluidics, technical challenges with fabrication and operation remain a significant hurdle to overcome. Problems with reliability that stem from these technical challenges represent a large barrier to adoption of microfluidics outside of academic research labs. This thesis argues that adoption of simple design principles is the best way of improving device reliability, especially for two-phase flow techniques such as droplet microfluidics which are, by their nature, more complicated than single phase flow techniques. A simple design philosophy could form the basis of a school of thought for microfluidic design which could accelerate its mainstream success. In this thesis a simple design philosophy is used to develop several new droplet microfluidic tools for chemical analysis.

In this work a simple droplet microfluidic capillary viscometer was presented which was capable of determining aqueous and nonaqueous sample viscosities by measuring the physical dimensions of droplets in a flow stream. A large advantage of this technique is that sample viscosity is determined using the relative flow rates of the two phases, which makes knowledge of absolute flow rates and pressure drops on chip unnecessary . Strict control over driving pressures used to move fluids is similarly

unnecessary. This viscometer was capable of processing samples as small as 38 nL, and had both precisions and accuracies better than 1%. Use of the device was demonstrated with crème de menthe peppermint liquor and baby oil, and fluorination of the PDMS surface was used to make the device compatible with samples of human urine. This demonstrates the potential applications of the viscometer for testing consumer goods, bioanalysis, and medical testing. The simple nature of the design, which consists of only a T-junction, also means it could be easily incorporated into many existing droplet platforms with minimal design changes. Spectroscopic detection of droplets was also performed, allowing for simultaneous assay and rheological characterization of samples. Future applications for this viscometer could involve detailed characterization of non-Newtonian fluids.

An operating theory for the droplet microfluidic viscometer was also presented, which was used to develop a second microfluidic droplet viscometer based around measurement of droplet frequency rather than the relative flow rates of the two phases. Large improvements in operating range for aqueous viscosity and shear rate, as well as sensitivity, were made over the first viscometer. Sample volume required was also decreased to 19 nL. Because the slope of the calibration for this viscometer does not depend on oil phase viscosity, the use of fluorinated surfactants in the oil phase was possible. This, along with complete fluorination of the inlet capillaries and PDMS channels, allowed for BSA solutions up to 26 mg/mL to be measured accurately. Many biologically relevant samples have total protein contents similar to this and should be compatible with this viscometer. An additional benefit to using frequency for determination of viscosity is that downstream fluorescence detection can be performed after reagent addition at a T-junction. The measured viscosity is not affected by reagent addition, and is also not affected by refraction of the excitation source off droplets. Some experiments, such as those carried out under variable shear rates or those involving measurement of oil phase viscosity, are more suited for the first viscometer presented. This makes the two techniques complementary in nature.

Because of the complicated nature of biological matrices separation techniques such as chromatography or electrophoresis are often necessary. Despite the widespread use of separation techniques in bioanalytical chemistry a disproportionately small number of droplet microfluidic papers involving bioanalysis utilize separations for droplet assay. This is likely because of challenges associated with removing the oil phase prior to delivery of droplet content to a separation technique. In this work a simple injector consisting of a cross junction with two straight channels interfaced out of plane is detailed which allows for injection and analysis of 750 pL droplets by capillary electrophoresis.

Injector performance was characterized and found to be satisfactory. Overall 750 pL volumes could injected with %RSD's in peak heights of 4.4% and separation efficiencies up to 27,000. The ability to analyze temporal information stored in droplet trains was also explored, and it was found that temporal resolutions down to 15 s were possible with the current configuration. Assay of riboflavin in human urine was demonstrated using the injector to assess compatibility with samples containing proteins. The injector was found to be compatible with the low protein content of urine, indicating the current version may be useful for some low-protein biological samples. The simple nature of this injector could allow for wider use of electrophoretic separations for droplet content analysis by making fabrication and operation of the injector easier than designs previously found in the literature. Future applications of this injector could involve its use for coupling capillary LC to CE for two dimensional separations.

Microfluidics is an exciting emerging field, with droplet microfluidics at the cutting edge of this new technology. To realize the full potential of droplet microfluidics, new robust and rugged tools for droplet handling and analysis need to be developed. Although this thesis details the development of three specific droplet microfluidic tools, it is the author's hope that the simple design principles used will serve as an example to aid others in successful development of new and reliable tools for chemical analysis using droplet microfluidics.

CITED LITERATURE

Abuasi, H. A.; McCabe, J. F.; Carrick, T. E.; Wassell, R. W. Displacement Rheometer: A Method of Measuring Working Time and Setting Time of Elastic Impression Materials. *J. Dent.* **1993**, *21* (6), 360–366.

Adamson, D. N.; Mustafi, D.; Zhang, J. X. J.; Zheng, B.; Ismagilov, R. F. Production of Arrays of Chemically Distinct Nanolitre Plugs via Repeated Splitting in Microfluidic Devices. *Lab Chip* **2006**, *6* (9), 1178.

Ahmad, I.; Rapson, H. D. C. Multicomponent Spectrophotometric Assay of Riboflavine and Photoproducts. *J. Pharm. Biomed. Anal.* **1990**, *8*, 217–223.

Ahmad, I.; Ahmed, S.; Sheraz, M. A.; Vaid, F. H. M. Effect of Borate Buffer on the Photolysis of Riboflavin in Aqueous Solution. *J. Photochem. Photobiol. B.* **2008**, *93* (2), 82–87.

Alberghina, D.; Giannetto, C.; Vazzana, I.; Ferrantelli, V.; Piccione, G. Reference Intervals for Total Protein Concentration, Serum Protein Fractions, and Albumin/Globulin Ratios in Clinically Healthy Dairy Cows. *J. Vet. Diagnostic Investig.* **2011**, *23* (1), 111–114.

AlSuhaimi, A.; Greenway, G. M.; McCreedy, T.; Youngvises, N. PDMS Microfluidic Device with an Integrated Optical Sensor for Determination of Zinc (II) in Pharmaceuticals: Toward the Production of Miniaturized Green Chemistry Analytical Systems. *Spectroscopy Letters*. 2009, pp 370–375.

Amin, S.; Barnett, G. V.; Pathak, J. a.; Roberts, C. J.; Sarangapani, P. S. Protein Aggregation, Particle Formation, Characterization & Rheology. *Curr. Opin. Colloid Interface Sci.* **2014**, *19* (5), 438–449.

Arayanarakool, R.; Shui, L.; Kengen, S. W. M.; van den Berg, A.; Eijkel, J. C. T. Single-Enzyme Analysis in a Droplet-Based Micro- and Nanofluidic System. *Lab Chip* **2013**, *13* (10), 1955–1962.

Bahram-Parvar, M. A Review of Modern Instrumental Techniques for Measurements of Ice Cream Characteristics. *Food Chem.* **2015**, *188*, 625–631.

Banpurkar, A. G.; Duits, M. H. G.; Van Den Ende, D.; Mugele, F. Electrowetting of Complex Fluids: Perspectives for Rheometry on Chip. *Langmuir* **2009**, *25*, 1245–1252.

Baret, J.-C.; Miller, O. J.; Taly, V.; Ryckelynck, M.; El-Harrak, A.; Frenz, L.; Rick, C.; Samuels, M. L.; Hutchison, J. B.; Agresti, J. J.; et al. Fluorescence-Activated Droplet Sorting (FADS): Efficient Microfluidic Cell Sorting Based on Enzymatic Activity. *Lab Chip* **2009**, *9* (13), 1850.

Baroud, C. N.; Gallaire, F.; Dangla, R. Dynamics of Microfluidic Droplets. *Lab Chip* **2010**, *10* (16), 2032.

Bessa, J.; Boeckle, S.; Beck, H.; Buckel, T.; Schlicht, S.; Ebeling, M.; Kiialainen, A.; Koulov, A.; Boll, B.; Weiser, T.; et al. The Immunogenicity of Antibody Aggregates in a Novel Transgenic Mouse Model. *Pharm. Res.* **2015**, 2344–2359.

Bremond, N.; Thiam, A. R.; Bibette, J. Decompressing Emulsion Droplets Favors Coalescence. *Phys. Rev. Lett.* **2008**, *100* (2), 024501.

Brennan, M. D.; Rexius-Hall, M. L.; Elgass, L. J.; Eddington, D. T. Oxygen Control with Microfluidics. *Lab Chip* **2014**, *14* (22), 4305–4318.

Brouzes, E.; Kruse, T.; Kimmerling, R.; Strey, H. H. Rapid and Continuous Magnetic Separation in Droplet Microfluidic Devices. *Lab Chip* **2015**, *15*, 908–919.

Brugarolas, T.; Tu, F.; Lee, D. Directed Assembly of Particles Using Microfluidic Droplets and Bubbles. *Soft Matter* **2013**, *9* (38), 9046.

Burgoyne, F.; Ghorbanian, S.; Qasaimeh, M. A.; Juncker, D. Rapid prototyping of branched microfluidics in PDMS using capillaries http://blogs.rsc.org/chipsandtips/2010/05/03/rapid-prototyping-of-branched-microfluidics-in-pdms-using-capillaries/.

Cahill, B. P.; Land, R.; Nacke, T.; Min, M.; Beckmann, D. Contactless Sensing of the Conductivity of Aqueous Droplets in Segmented Flow. *Sensors Actuators, B Chem.* **2011**, *159* (1), 286–293.

Castillo-Tejas, J.; Alvarado, J. F. J.; Carro, S.; Pérez-Villaseñor, F.; Bautista, F.; Manero, O. Rheology of Wormlike Micelles from Non-Equilibrium Molecular Dynamics. *J. Nonnewton. Fluid Mech.* **2011**, *166* (3-4), 194–207.

Chambers, A. G.; Mellors, J. S.; Henley, W. H.; Ramsey, J. M. Monolithic Integration of Two-Dimensional Liquid Chromatography−Capillary Electrophoresis and Electrospray Ionization on a Microfluidic Device. *Anal. Chem.* **2011**, *83* (3), 842–849.

De Chaumont, F.; Dallongeville, S.; Chenouard, N.; Hervé, N.; Pop, S.; Provoost, T.; Meas-Yedid, V.; Pankajakshan, P.; Lecomte, T.; Le Montagner, Y.; et al. Icy: An Open Bioimage Informatics Platform for Extended Reproducible Research. *Nat. Methods* **2012**, *9* (7), 690–696.

Choi, S.; Park, J.-K. Microfluidic Rheometer for Characterization of Protein Unfolding and Aggregation in Microflows. *Small* **2010**, *6* (12), 1306–1310.

Cole, R. H.; de Lange, N.; Gartner, Z. J.; Abate, A. R. Compact and Modular Multicolour Fluorescence Detector for Droplet Microfluidics. *Lab Chip* **2015**, *15*, 2754–2758.

Culbertson, C. T.; Mickleburgh, T. G.; Stewart-James, S. a.; Sellens, K. a.; Pressnall, M. Micro Total Analysis Systems: Fundamental Advances and Biological Applications. *Anal. Chem.* **2014**, *86* (1), 95–118. 111

Deal, K. S.; Easley, C. J. Self-Regulated, Droplet-Based Sample Chopper for Microfluidic Absorbance Detection. *Anal. Chem.* **2012**, *84*, 1510–1516.

DeLaMarre, M.; Keyzer, A.; Shippy, S. a. Development of a Simple Droplet-Based Microfluidic Capillary Viscometer for Low-Viscosity Newtonian Fluids. *Anal. Chem.* **2015**, 150331162924006.

Desmarais, S. M.; Haagsman, H. P.; Barron, A. E. Microfabricated Devices for Biomolecule Encapsulation. *Electrophoresis*. 2012, pp 2639–2649.

Drössler, P.; Holzer, W.; Penzkofer, A.; Hegemann, P. pH Dependence of the Absorption and Emission Behaviour of Riboflavin in Aqueous Solution. *Chem. Phys.* **2002**, *282* (3), 429–439.

Edgar, J. S.; Pabbati, C. P.; Lorenz, R. M.; He, M.; Fiorini, G. S.; Chiu, D. T. Capillary Electrophoresis Separation in the Presence of an Immiscible Boundary for Droplet Analysis. *Anal. Chem.* **2006**, *78*, 6948–6954.

Edgar, J. S.; Milne, G.; Zhao, Y.; Pahbati, C. P.; Lim, D. S. W.; Chiu, D. T. Compartmentalization of Chemically Separated Components into Droplets. *Angew. Chemie - Int. Ed.* **2009**, *48*, 2719–2722.

Fidalgo, L. M.; Abell, C.; Huck, W. T. S. Surface-Induced Droplet Fusion in Microfluidic Devices. *Lab Chip* **2007**, *7* (8), 984.

Filipe, V.; Jiskoot, W.; Basmeleh, A. H.; Halim, A.; Schellekens, H.; Brinks, V. Immunogenicity of Different Stressed IgG Monoclonal Antibody Formulations in Immune Tolerant Transgenic Mice. *MAbs* **2012**, *4* (6), 740–752.

Filla, L. A.; Kirkpatrick, D. C.; Martin, R. S. Use of a Corona Discharge to Selectively Pattern a Hydrophilic/hydrophobic Interface for Integrating Segmented Flow with Microchip Electrophoresis and Electrochemical Detection. *Anal. Chem.* **2011**, *83*, 5996–6003.

Flint, M.; du Plessis, S. S.; Menkveld, R. Revisiting the Assessment of Semen Viscosity and Its Relationship to Leucocytospermia. *Andrologia* **2014**, *46* (8), 837–841.

Foley, J.; Dorsey, J. Equations for Calculation of Chromatographic Figures of Merit for Ideal and Skewed Peaks. *Anal. Chem.* **1983**, *55* (4), 730–737.

Fu, T.; Wu, Y.; Ma, Y.; Li, H. Z. Droplet Formation and Breakup Dynamics in Microfluidic Flow-Focusing Devices: From Dripping to Jetting. *Chem. Eng. Sci.* **2012**, *84*, 207–217.

Galindo-Rosales, F. J.; Alves, M. A.; Oliveira, M. S. N. Microdevices for Extensional Rheometry of Low Viscosity Elastic Liquids: A Review. *Microfluidics and Nanofluidics*. 2013, pp 1–19.

Garstecki, P.; Fuerstman, M. J.; Stone, H. a; Whitesides, G. M. Formation of Droplets and Bubbles in a Microfluidic T-Junction-Scaling and Mechanism of Break-Up. *Lab Chip* **2006**, *6* (3), 437–446.

German, I.; Roper, M. G.; Kalra, S. P.; Rhinehart, E.; Kennedy, R. T. Capillary Liquid Chromatography of Multiple Peptides with on-Line Capillary Electrophoresis Immunoassay Detection. *Electrophoresis* **2001**, *22* (17), 3659–3667. 112

Groß, G. A.; Thyagarajan, V.; Kielpinski, M.; Henkel, T.; Köhler, J. M. Viscosity-Dependent Enhancement of Fluid Resistance in Water/glycerol Micro Fluid Segments. *Microfluid. Nanofluidics* **2008**, *5*, 281–287.

Gu, F.; Zhou, X.; Zhu, X.; Zhao, M.; Hao, J.; Yu, P.; Mao, L. In Vivo and Continuous Measurement of Bisulfide in the Hippocampus of Rat's Brain by an on-Line Integrated Microdialysis/droplet-Based Microfluidic System. *Analyst* **2015**.

Guillot, P.; Moulin, T.; Kötitz, R.; Guirardel, M.; Dodge, A.; Joanicot, M.; Colin, A.; Bruneau, C.-H.; Colin, T. Towards a Continuous Microfluidic Rheometer. *Microfluid. Nanofluidics* **2008**, *5* (5), 619–630.

Han, Z.; Tang, X.; Zheng, B. A PDMS Viscometer for Microliter Newtonian Fluid. *J. Micromechanics Microengineering* **2007**, *17* (9), 1828–1834.

Haszeldine, R. N.; Smith, F. 129. Organic Fluorides. Part VI. The Chemical and Physical Properties of Certain Fluorocarbons. *J. Chem. Soc.* **1951**, 603.

Hess, D.; Rane, A.; deMello, A. J.; Stavrakis, S. High-Throughput, Quantitative Enzyme Kinetic Analysis in Microdroplets Using Stroboscopic Epifluorescence Imaging. *Anal. Chem.* **2015**, 150416110305008.

Hooker, T. F.; Jorgenson, J. W. A Transparent Flow Gating Interface for the Coupling of Microcolumn LC with CZE in a Comprehensive Two-Dimensional System. *Anal. Chem.* **1997**, *69* (20), 4134–4142.

Hu, L.; Yang, X.; Wang, C.; Yuan, H.; Xiao, D. Determination of Riboflavin in Urine and Beverages by Capillary Electrophoresis with in-Column Optical Fiber Laser-Induced Fluorescence Detection. *J. Chromatogr. B Anal. Technol. Biomed. Life Sci.* **2007**, *856*, 245–251.

Hung, L.-H.; Choi, K. M.; Tseng, W.-Y.; Tan, Y.-C.; Shea, K. J.; Lee, A. P. Alternating Droplet Generation and Controlled Dynamic Droplet Fusion in Microfluidic Device for CdS Nanoparticle Synthesis. *Lab Chip* **2006**, *6* (2), 174.

Inman, B. A.; Etienne, W.; Rubin, R.; Owusu, R. A.; Oliveira, T. R.; Rodriques, D. B.; Maccarini, P. F.; Stauffer, P. R.; Mashal, A.; Dewhirst, M. W. The Impact of Temperature and Urinary Constituents on Urine Viscosity and Its Relevance to Bladder Hyperthermia Treatment. *Int. J. Hyperthermia* **2013**, *29* (3), 206–210.

Isgor, P. K.; Marcali, M.; Keser, M.; Elbuken, C. Microfluidic Droplet Content Detection Using Integrated Capacitive Sensors. *Sensors Actuators B Chem.* **2015**, *210*, 669–675.

Jeong, O. C.; Park, S. W.; Yang, S. S.; Pak, J. J. Fabrication of a Peristaltic PDMS Micropump. *Sensors Actuators A Phys.* **2005**, *123-124*, 453–458.

Jeong, S.-K.; Cho, Y. I.; Duey, M.; Rosenson, R. S. Cardiovascular Risks of Anemia Correction with Erythrocyte Stimulating Agents: Should Blood Viscosity Be Monitored for Risk Assessment? *Cardiovasc. Drugs Ther.* **2010**, *24* (2), 151–160. 113

Ji, J.; Nie, L.; Qiao, L.; Li, Y.; Guo, L.; Liu, B.; Yang, P.; Girault, H. H. Proteolysis in Microfluidic Droplets: An Approach to Interface Protein Separation and Peptide Mass Spectrometry. *Lab on a Chip*. 2012, p 2625.

Ji, J.; Nie, L.; Li, Y.; Yang, P.; Liu, B. Simultaneous Online Enrichment and Identi Fi Cation of Trace Species Based on Micro Fl Uidic Droplets. **2013**.

Joensson, H. N.; Andersson Svahn, H. Droplet Microfluidics-A Tool for Single-Cell Analysis. *Angew. Chemie Int. Ed.* **2012**, *51* (49), 12176–12192.

Kamiyama, T.; Morita, M.; Kimura, T. The Gibbs Energies of Activation of Lysozyme for Viscous Flow in Water + Dimethyl Sulfoxide Solutions at 298.15 K. *J. Solution Chem.* **2008**, *37* (1), 27–34.

Kang, Y. J.; Yoon, S. Y.; Lee, K.-H.; Yang, S. A Highly Accurate and Consistent Microfluidic Viscometer for Continuous Blood Viscosity Measurement. *Artif. Organs* **2010**, *34* (11), 944–949.

Kautz, R. A.; Goetzinger, W. K.; Karger, B. L. High-Throughput Microcoil NMR of Compound Libraries Using Zero-Dispersion Segmented Flow Analysis. *J. Comb. Chem.* **2005**, *7* (1), 14–20.

Kelly, A. E.; Ou, H. D.; Withers, R.; Dötsch, V. Low-Conductivity Buffers for High-Sensitivity NMR Measurements. *J. Am. Chem. Soc.* **2002**, *124* (40), 12013–12019.

Kelly, R. T.; Page, J. S.; Marginean, I.; Tang, K.; Smith, R. D. Dilution-Free Analysis from Picoliter Droplets by Nano-Electrospray Ionization Mass Spectrometry. *Angew. Chemie - Int. Ed.* **2009**, *48*, 6832–6835.

Kilby, J. S. Miniaturized Electronic Circuits. Google Patents 1964.

Kim, J. H.; Jeon, T. Y.; Choi, T. M.; Shim, T. S.; Kim, S.-H.; Yang, S.-M. Droplet Microfluidics for Producing Functional Microparticles. *Langmuir* **2014**, *30* (6), 1473–1488.

Kim, S.-J.; Lai, D.; Park, J. Y.; Yokokawa, R.; Takayama, S. Microfluidic Automation Using Elastomeric Valves and Droplets: Reducing Reliance on External Controllers. *Small* **2012**, *8* (19), 2925–2934.

Küster, S. K.; Fagerer, S. R.; Verboket, P. E.; Eyer, K.; Jefimovs, K.; Zenobi, R.; Dittrich, P. S. Interfacing Droplet Microfluidics with Matrix-Assisted Laser Desorption/ionization Mass Spectrometry: Label-Free Content Analysis of Single Droplets. *Anal. Chem.* **2013**, *85* (3), 1285–1289.

Lan, W. J.; Li, S. W.; Xu, J. H.; Luo, G. S. Rapid Measurement of Fluid Viscosity Using Co-Flowing in a Co-Axial Microfluidic Device. *Microfluid. Nanofluidics* **2010**, *8* (5), 687–693.

Langelier, S. M.; Chang, D. S.; Zeitoun, R. I.; Burns, M. A. Acoustically Driven Programmable Liquid Motion Using Resonance Cavities. *Proc. Natl. Acad. Sci. U. S. A.* **2009**, *106*, 12617–12622.

Lauer, H. H.; McManigill, D. Capillary Zone Electrophoresis of Proteins in Untreated Fused Silica Tubing. *Anal. Chem.* **1986**, *58*, 166–170. 114

Lee, J.; Tripathi, A. Intrinsic Viscosity of Polymers and Biopolymers Measured by Microchip. *Anal. Chem.* **2005**, *77* (22), 7137–7147.

Lewis, K.; Opiteck, G.; Jorgenson, J.; Sheeley, D. Comprehensive on-Line RPLC-CZE-MS of Peptides. *J. Am. Soc. Mass Spectrom.* **1997**, *8* (5), 495–500.

Li, L.; Ismagilov, R. F. Protein Crystallization Using Microfluidic Technologies Based on Valves, Droplets, and SlipChip. *Annu. Rev. Biophys.* **2010**, *39* (1), 139–158.

Liu, H.; Liu, J.; Li, S.; Chen, L.; Zhou, H.; Zhu, J.; Zheng, Z. Fiber-Optic SERS Microfluidic Chip Based on Light-Induced Gold Nano-Particle Aggregation. *Opt. Commun.* **2015**, *352*, 148–154.

Livak-Dahl, E.; Lee, J.; Burns, M. A. Nanoliter Droplet Viscometer with Additive-Free Operation. *Lab Chip* **2013**, *13* (2), 297–301.

Lu, J.; Litster, J. D.; Nagy, Z. K. Nucleation Studies of Active Pharmaceutical Ingredients in an Air-Segmented Microfluidic Drop-Based Crystallizer. *Cryst. Growth Des.* **2015**, 150629124331001.

Maa, Y.-F.; Hsu, C. C. Protein Denaturation by Combined Effect of Shear and Air-Liquid Interface. *Biotechnol. Bioeng.* **1997**, *54* (6), 503–512.

MacCose, M. J. https://proteomicsresource.washington.edu/docs/pressurecell/UWPR_Pressure_Cell_for_packing_capillary_columns.pdf (accessed May 7, 2015).

Marshall, T.; Williams, K. M. Total Protein Determination in Urine: Elimination of a Differential Response between the Coomassie Blue and Pyrogallol Red Protein Dye-Binding Assays. *Clin. Chem.* **2000**, *46* (3), 392–398.

Mazutis, L.; Baret, J.-C.; Treacy, P.; Skhiri, Y.; Araghi, A. F.; Ryckelynck, M.; Taly, V.; Griffiths, A. D. Multi-Step Microfluidic Droplet Processing: Kinetic Analysis of an in Vitro Translated Enzyme. *Lab Chip* **2009**, *9* (20), 2902.

McDonald, J. C.; Duffy, D. C.; Anderson, J. R.; Chiu, D. T.; Wu, H.; Schueller, O. J.; Whitesides, G. M. Fabrication of Microfluidic Systems in Poly(dimethylsiloxane). *Electrophoresis* **2000**, *21* (1), 27–40.

McDonnell, A. G.; Gopesh, T. C.; Lo, J.; O'Bryan, M.; Yeo, L. Y.; Friend, J. R.; Prabhakar, R. Motility Induced Changes in Viscosity of Suspensions of Swimming Microbes in Extensional Flows. *Soft Matter* **2015**, *11* (23), 4658–4668.

Moore, A. W.; Jorgenson, J. W. Rapid Comprehensive Two-Dimensional Separations of Peptides via RPLC-Optically Gated Capillary Zone Electrophoresis. *Anal. Chem.* **1995**, *67* (19), 3448–3455.

Mould, S.; Barbas, J.; MacHado, A. V.; Nóbrega, J. M.; Covas, J. A. Measuring the Rheological Properties of Polymer Melts with on-Line Rotational Rheometry. *Polym. Test.* **2011**, *30* (6), 602–610.

Nelson, W. C.; Kavehpour, H. P.; Kim, C.-J. C. J. A Miniature Capillary Breakup Extensional Rheometer by Electrostatically Assisted Generation of Liquid Filaments. *Lab Chip* **2011**, *11*, 2424–2431. 115

Nguyen, E. H.; Schwartz, M. P.; Murphy, W. L. Biomimetic Approaches to Control Soluble Concentration Gradients in Biomaterials. *Macromol. Biosci.* **2011**, *11* (4), 483–492.

Nguyen, N.-T.; Yap, Y.-F.; Sumargo, A. Microfluidic Rheometer Based on Hydrodynamic Focusing. *Meas. Sci. Technol.* **2008**, *19* (8), 085405.

Niu, X. Z.; Zhang, B.; Marszalek, R. T.; Ces, O.; Edel, J. B.; Klug, D. R.; deMello, A. J. Droplet-Based Compartmentalization of Chemically Separated Components in Two-Dimensional Separations. *Chem. Commun. (Camb).* **2009**, 6159–6161.

Niu, X.; Pereira, F.; Edel, J. B.; De Mello, A. J. Droplet-Interfaced Microchip and Capillary Electrophoretic Separations. *Anal. Chem.* **2013**, *85*, 8654–8660.

Pan, M.; Rosenfeld, L.; Kim, M.; Xu, M.; Lin, E.; Derda, R.; Tang, S. K. Y. Fluorinated Pickering Emulsions Impede Interfacial Transport and Form Rigid Interface for the Growth of Anchorage-Dependent Cells. *ACS Appl. Mater. Interfaces* **2014**, *6* (23), 21446–21453.

Pei, J.; Nie, J.; Kennedy, R. T. Parallel Electrophoretic Analysis of Segmented Samples on Chip for High-Throughput Determination of Enzyme Activities. *Anal. Chem.* **2010**, *82*, 9261–9267.

Pennell, T.; Suchyna, T.; Wang, J.; Heo, J.; Felske, J. D.; Sachs, F.; Hua, S. Z. Microfluidic Chip to Produce Temperature Jumps for Electrophysiology. *Anal. Chem.* **2008**, *80* (7), 2447–2451.

Pipe, C. J.; McKinley, G. H. Microfluidic Rheometry. *Mech. Res. Commun.* **2009**, *36* (1), 110–120.

Piyankarage, S. C.; Augustin, H.; Grosjean, Y.; Featherstone, D. E.; Shippy, S. A. Hemolymph Amino Acid Analysis of Individual Drosophila Larvae. *Anal. Chem.* **2008**, *80*, 1201–1207.

Piyankarage, S. C.; Featherstone, D. E.; Shippy, S. A. Nanoliter Hemolymph Sampling and Analysis of Individual Adult Drosophila Melanogaster. *Anal. Chem.* **2012**, *84* (10), 4460–4466.

PubMed. Pubmed search for “micro” http://www.ncbi.nlm.nih.gov/pubmed/?term=micro (accessed Feb 8, 2015).

Richards, J. L. Viscosity and the Shapes of Macromolecules: A Physical Chemistry Experiment Using Molecular-Level Models in the Interpretation of Macroscopic Data Obtained from Simple Measurements. *J. Chem. Educ.* **1993**, *70* (8), 685.

Roach, L. S.; Song, H.; Ismagilov, R. F. Controlling Nonspecific Protein Adsorption in a Plug-Based Microfluidic System by Controlling Interfacial Chemistry Using Fluorous-Phase Surfactants. *Anal. Chem.* **2005**, *77*, 785–796.

Rogers, M.; Leong, C.; Niu, X.; de Mello, A.; Parker, K. H.; Boutelle, M. G. Optimisation of a Microfluidic Analysis Chamber for the Placement of Microelectrodes. *Phys. Chem. Chem. Phys.* **2011**, *13*, 5298–5303.

Rogers, S. A.; Calabrese, M. A.; Wagner, N. J. Rheology of Branched Wormlike Micelles. *Curr. Opin. Colloid Interface Sci.* **2014**, *19* (6), 530–535. 116

Roman, G. T.; Wang, M.; Shultz, K. N.; Jennings, C.; Kennedy, R. T. Sampling and Electrophoretic Analysis of Segmented Flow Streams Using Virtual Walls in a Microfluidic Device. *Anal. Chem.* **2008**, *80*, 8231–8238.

Rowe, H. Impact Factors 2014 http://blogs.rsc.org/rscpublishing/2015/06/25/impact-factors-2014/ (accessed Feb 8, 2015).

Van Ruymbeke, E.; Lee, H.; Chang, T.; Nikopoulou, A.; Hadjichristidis, N.; Snijkers, F.; Vlassopoulos, D. Molecular Rheology of Branched Polymers: Decoding and Exploring the Role of Architectural Dispersity through a Synergy of Anionic Synthesis, Interaction Chromatography, Rheometry and Modeling. *Soft Matter* **2014**, *10* (27), 4762.

Salazar Vázquez, B. Y.; Salazar Vázquez, M. A.; Jáquez, M. G.; Bracho Huemoeller, A. H.; Intaglietta, M.; Cabrales, P. Blood Pressure Directly Correlates with Blood Viscosity in Diabetes Type 1 Children but Not in Normals. *Clin. Hemorheol. Microcirc.* **2010**, *44* (1), 55–61.

Schneider, C. A.; Rasband, W. S.; Eliceiri, K. W. NIH Image to ImageJ: 25 Years of Image Analysis. *Nature Methods*. 2012, pp 671–675.

Schneider, T.; Kreutz, J.; Chiu, D. T. The Potential Impact of Droplet Microfluidics in Biology. *Anal Chem*. 2013, pp 3476–3482.

Schultz, K. M.; Furst, E. M. High-Throughput Rheology in a Microfluidic Device. *Lab Chip* **2011**, *11* (22), 3802–3809.

Scott, D. E.; Willis, S. D.; Gabbert, S.; Johnson, D.; Naylor, E.; Janle, E. M.; Krichevsky, J. E.; Lunte, C. E.; Lunte, S. M. Development of an on-Animal Separation-Based Sensor for Monitoring Drug Metabolism in Freely Roaming Sheep. *Analyst* **2015**, *140* (11), 3820–3829.

Segur, J. B.; Oberstar, H. E. Viscosity of Glycerol and Its Aqueous Solutions. *Ind. Eng. Chem.* **1951**, *43* (9), 2117–2120.

Shagawa, T.; Torii, H.; Kato, F.; Ogi, H.; Hirao, M. Relationship between Viscosity Change and Specificity in Protein Binding Reaction Studied by High-Frequency Wireless and Electrodeless MEMS Biosensor. *Jpn. J. Appl. Phys.* **2015**, *54* (6), 068001.

Shah, G. J.; Ding, H.; Sadeghi, S.; Chen, S.; Kim, C.-J. "CJ"; van Dam, R. M. On-Demand Droplet Loading for Automated Organic Chemistry on Digital Microfluidics. *Lab Chip* **2013**, *13* (14), 2785.

Shalliker, R. A.; Catchpoole, H. J.; Dennis, G. R.; Guiochon, G. Visualising Viscous Fingering in Chromatography Columns: High Viscosity Solute Plug. *J. Chromatogr. A* **2007**, *1142*, 48–55.

Siegel, G. J.; Agranoff, B. W.; Albers, R. W.; Fisher, S. K.; Uhler, M. D. *Basic Neurochemistry*; Lippincott-Raven, 1999.

Skeggs, L. T. Persistence ... and Prayer: From the Artificial Kidney to the Autoanalyzer. *Clin. Chem.* **2000**, *46* (9), 1425–1436. 117

Slaney, T. R.; Nie, J.; Hershey, N. D.; Thwar, P. K.; Linderman, J.; Burns, M. A.; Kennedy, R. T. Push-Pull Perfusion Sampling with Segmented Flow for High Temporal and Spatial Resolution in Vivo Chemical Monitoring. *Anal. Chem.* **2011**, *83*, 5207–5213.

Sloop, G. D. A Unifying Theory of Atherogenesis. *Med. Hypotheses* **1996**, *47* (4), 321–325.

Smith, C. a.; Li, X.; Mize, T. H.; Sharpe, T. D.; Graziani, E. I.; Abell, C.; Huck, W. T. S. Sensitive, High Throughput Detection of Proteins in Individual, Surfactant-Stabilized Picoliter Droplets Using Nanoelectrospray Ionization Mass Spectrometry. *Anal. Chem.* **2013**, *85* (8), 3812–3816.

Solomon, D. E.; Vanapalli, S. A. Multiplexed Microfluidic Viscometer for High-Throughput Complex Fluid Rheology. *Microfluid. Nanofluidics* **2014**, *16* (4), 677–690.

Song, H.; Tice, J. D.; Ismagilov, R. F. A Microfluidic System for Controlling Reaction Networks in Time. *Angew. Chemie Int. Ed.* **2003**, *42* (7), 768–772.

Song, H.; Chen, D. L.; Ismagilov, R. F. Reactions in Droplets in Microfluidic Channels. *Angew. Chemie Int. Ed.* **2006**, pp 7336–7356.

Srinivasan, V.; Pamula, V. K.; Fair, R. B. An Integrated Digital Microfluidic Lab-on-a-Chip for Clinical Diagnostics on Human Physiological Fluids. *Lab Chip* **2004**, *4*, 310–315.

Srivastava, N.; Burns, M. A. Analysis of Non-Newtonian Liquids Using a Microfluidic Capillary Viscometer. *Anal. Chem.* **2006**, *78* (5), 1690–1696.

Srivastava, N.; Davenport, R. D.; Burns, M. A. Nanoliter Viscometer for Analyzing Blood Plasma and Other Liquid Samples Viscometer That Quickly , Easily , and Inexpensively Mea-. *Anal. Chem.* **2005**, *77* (2), 383–392.

Stefan Stephanus du Plessis, Sheila Gokul, A. A. Semen Hyperviscosity: Causes, Consequences, and Cures. *Front. Biosci.* **2013**, No. 1, 224–231.

Stokes, J. R.; Boehm, M. W.; Baier, S. K. Oral Processing, Texture and Mouthfeel: From Rheology to Tribology and beyond. *Current Opinion in Colloid and Interface Science*. 2013, pp 349–359.

Sun, S.; Slaney, T. R.; Kennedy, R. T. Label Free Screening of Enzyme Inhibitors at Femtomole Scale Using Segmented Flow Electrospray Ionization Mass Spectrometry. *Anal. Chem.* **2012**, *84* (13), 5794–5800.

Tabeling, P. A Brief Introduction to Slippage, Droplets and Mixing in Microfluidic Systems. *Lab Chip* **2009**, *9* (17), 2428.

Teh, S.-Y.; Lin, R.; Hung, L.-H.; Lee, A. P. Droplet Microfluidics. *Lab Chip* **2008**, *8* (2), 198–220. 118

Terry, S. C.; Jerman, J. H.; Angell, J. B. A Gas Chromatographic Air Analyzer Fabricated on a Silicon Wafer. *IEEE Transactions on Electron Devices*. 1979, pp 1880–1886.

Theberge, A. B.; Courtois, F.; Schaerli, Y.; Fischlechner, M.; Abell, C.; Hollfelder, F.; Huck, W. T. S. Microdroplets in Microfluidics: An Evolving Platform for Discoveries in Chemistry and Biology. *Angew. Chemie Int. Ed*. 2010, pp 5846–5868.

Ting, T. H.; Yap, Y. F.; Nguyen, N.-T.; Wong, T. N.; Chai, J. C. K.; Yobas, L. Thermally Mediated Breakup of Drops in Microchannels. *Appl. Phys. Lett.* **2006**, *89* (23), 234101.

Trivedi, V.; Doshi, A.; Kurup, G. K.; Ereifej, E.; Vandevord, P. J.; Basu, A. S. A Modular Approach for the Generation, Storage, Mixing, and Detection of Droplet Libraries for High Throughput Screening. *Lab Chip* **2010**, *10* (18), 2433–2442.

Velve Casquillas, G.; Fu, C.; Le Berre, M.; Cramer, J.; Meance, S.; Plecis, A.; Baigl, D.; Greffet, J.-J.; Chen, Y.; Piel, M.; et al. Fast Microfluidic Temperature Control for High Resolution Live Cell Imaging. *Lab Chip* **2011**, *11* (3), 484–489.

Vickers, J. A.; Caulum, M. M.; Henry, C. S. Generation of Hydrophilic Poly(dimethylsiloxane) for High-Performance Microchip Electrophoresis. *Anal. Chem.* **2006**, *78*, 7446–7452.

Wang, M.; Roman, G. T.; Perry, M. L.; Kennedy, R. T. Microfluidic Chip for High Efficiency Electrophoretic Analysis of Segmented Flow from a Microdialysis Probe and in Vivo Chemical Monitoring. *Anal. Chem.* **2009**, *81*, 9072–9078.

Wang, M.; Hershey, N. D.; Mabrouk, O. S.; Kennedy, R. T. Collection, Storage, and Electrophoretic Analysis of Nanoliter Microdialysis Samples Collected from Awake Animals in Vivo. *Anal. Bioanal. Chem.* **2011**, *400*, 2013–2023.

Wang, W.; Zhang, M.-J.; Chu, L.-Y. Microfluidic Approach for Encapsulation via Double Emulsions. *Curr. Opin. Pharmacol.* **2014**, *18*, 35–41.

Ward, T.; Faivre, M.; Abkarian, M.; Stone, H. a. Microfluidic Flow Focusing: Drop Size and Scaling in Pressure versus Flow-Rate-Driven Pumping. *Electrophoresis* **2005**, *26*, 3716–3724.

Wu, L.; Wang, Z.; Zong, S.; Cui, Y. Rapid and Reproducible Analysis of Thiocyanate in Real Human Serum and Saliva Using a Droplet SERS-Microfluidic Chip. *Biosens. Bioelectron.* **2014**, *62*, 13–18.

Xiao, Z.; Niu, M.; Zhang, B. Droplet Microfluidics Based Microseparation Systems. *J. Sep. Sci.* **2012**, *35* (10-11), 1284–1293.

Xu, J. H.; Li, S. W.; Tan, J.; Luo, G. S. Correlations of Droplet Formation in T-Junction Microfluidic Devices: From Squeezing to Dripping. *Microfluid. Nanofluidics* **2008**, *5* (6), 711–717.

Ye, L.; Wang, X.; Han, J.; Gao, F.; Xu, L.; Xiao, Z.; Bai, P.; Wang, Q.; Zhang, B. Two Dimensional Separations of Human Urinary Protein Digest Using a Droplet-Interfaced Platform. *Anal. Chim. Acta* **2015**, 1–9. 119

Zheng, B.; Ismagilov, R. F. A Microfluidic Approach for Screening Submicroliter Volumes against Multiple Reagents by Using Preformed Arrays of Nanoliter Plugs in a Three-Phase Liquid/Liquid/Gas Flow. *Angew. Chemie Int. Ed.* **2005**, *44* (17), 2520–2523.

Zheng, B.; Roach, L. S.; Ismagilov, R. F. Screening of Protein Crystallization Conditions on a Microfluidic Chip Using Nanoliter-Size Droplets. *J. Am. Chem. Soc.* **2003**, *125* (37), 11170–11171.

Zheng, B.; Tice, J. D.; Roach, L. S.; Ismagilov, R. F. A Droplet-Based, Composite PDMS/glass Capillary Microfluidic System for Evaluating Protein Crystallization Conditions by Microbatch and Vapor-Diffusion Methods with on-Chip X-Ray Diffraction. *Angew. Chemie Int. Ed.* **2004**, *43* (19), 2508–2511.

Zhou, H.; Li, G.; Yao, S. A Droplet-Based pH Regulator in Microfluidics. *Lab Chip* **2014**, *14* (11), 1917–1922.

Zhu, Y.; Fang, Q. Integrated Droplet Analysis System with Electrospray Ionization-Mass Spectrometry Using a Hydrophilic Tongue-Based Droplet Extraction Interface. *Anal. Chem.* **2010**, *82* (19), 8361–8366.

APPENDIX A –PERMISSIONS

RightsLink®

Home | Create Account | Help | Live Chat

Title: Development of a Simple Droplet-Based Microfluidic Capillary Viscometer for Low-Viscosity Newtonian Fluids

Author: Michael F. DeLaMarre, Alec Keyzer, Scott A. Shippy

Publication: Analytical Chemistry

Publisher: American Chemical Society

Date: May 1, 2015

LOGIN

If you're a copyright.com user, you can login to RightsLink using your copyright.com credentials. Already **a RightsLink user** or want to learn more?

PERMISSION/LICENSE IS GRANTED FOR YOUR ORDER AT NO CHARGE

This type of permission/license, instead of the standard Terms & Conditions, is sent to you because no fee is being charged for your order. Please note the following:

- Permission is granted for your request in both print and electronic formats, and translations.
- If figures and/or tables were requested, they may be adapted or used in part.
- Please print this page for your records and send a copy of it to your publisher/graduate school.
- Appropriate credit for the requested material should be given as follows: "Reprinted (adapted) with permission from (COMPLETE REFERENCE CITATION). Copyright (YEAR) American Chemical Society." Insert appropriate information in place of the capitalized words.
- One-time permission is granted only for the use specified in your request. No additional uses are granted (such as derivative works or other editions). For any other uses, please submit a new request.

BACK CLOSE WINDOW

Title: Development of a Simplified Microfluidic Injector for Analysis of Droplet Content via Capillary Electrophoresis

Author: Michael F. DeLaMarre, Scott A. Shippy

Publication: Analytical Chemistry

Publisher: American Chemical Society

Date: Oct 1, 2014

PERMISSION/LICENSE IS GRANTED FOR YOUR ORDER AT NO CHARGE

This type of permission/license, instead of the standard Terms & Conditions, is sent to you because no fee is being charged for your order. Please note the following:

- Permission is granted for your request in both print and electronic formats, and translations.
- If figures and/or tables were requested, they may be adapted or used in part.
- Please print this page for your records and send a copy of it to your publisher/graduate school.
- Appropriate credit for the requested material should be given as follows: "Reprinted (adapted) with permission from (COMPLETE REFERENCE CITATION). Copyright (YEAR) American Chemical Society." Insert appropriate information in place of the capitalized words.
- One-time permission is granted only for the use specified in your request. No additional uses are granted (such as derivative works or other editions). For any other uses, please submit a new request.

BACK CLOSE WINDOW

UNIVERSITY OF ILLINOIS
AT CHICAGO

Office for the Protection of Research Subjects (OPRS)
Office of the Vice Chancellor for Research (MC 672)
203 Administrative Office Building
1737 West Polk Street
Chicago, Illinois 60612-7227

Notice of Determination of Human Subject Research

September 8, 2014

20140850-84637-1

20140850-84637-1

Michael DeLaMarre
Chemistry
845 W Taylor ST, Room 4500
M/C 111
Chicago, IL 60607
Phone: (312) 996-5420

RE: **Protocol # 2014-0850**
Development of a simplified microfluidic injector for analysis of droplet content via capillary electrophoresis

Sponsor: None

Dear Michael DeLaMarre:

☐ The UIC Office for the Protection of Research Subjects received your "Determination of Whether an Activity Represents Human Subjects Research" application, and has determined that this activity **DOES NOT meet the definition of human subject research** as defined by 45 CFR 46.102(f).

You may conduct your activity without further submission to the IRB.

If this activity is used in conjunction with any other research involving human subjects or if it is modified in any way, it must be re-reviewed by OPRS staff.

APPENDIX B – SUPPORTING INFORMATION

B1. Derivation of Equations For Use With Rectangular Channels.

The channels used in the microfluidic device presented are cylindrical, but most laboratories utilize microfluidic devices fabricated with photolithography techniques, which form rectangular channels. Poiseuille's law has been used previously for microfluidic viscometry using rectangular channels by Han et al. (Han et al., 2007) Han et al. use a version of Poiseuille's law derived for rectangular channels as shown below

$$v = \left(\frac{2hw}{h+w}\right)^2 \frac{|\Delta P|}{32\eta l} \quad \text{B1}$$

where *v* is the linear velocity of a fluid with viscosity η flowing through a rectangular channel with height h, width w, and length l, and with pressure drop over the length of the channel equal to ΔP. By using the cross sectional area of the channel, h×w, the equation can be expressed in terms of flow rate (Φ).

$$\Phi = \frac{4h^3w^3}{(h+w)^2} \frac{|\Delta P|}{32\eta l} \quad \text{B2}$$

The aqueous and oil flow rates can be substituted into the expression of α to derive the following equation for a droplet viscometer with rectangular channels

$$\alpha = \frac{\Phi_{oil}}{\Phi_{aq}} = \left(\frac{w_{oil}}{w_{aq}}\right)^3 \left(\frac{h+w_{aq}}{h+w_{oil}}\right)^2 \left(\frac{\eta_{aq}}{\eta_{oil}}\right)\left(\frac{|\Delta P|_{oil}}{|\Delta P|_{aq}}\right)\left(\frac{l_{aq}}{l_{oil}}\right) \quad \text{B3}$$

where w_{oil} and w_{aq} are the widths of the oil and aqueous inlets, h is the height of all channels, η_{aq} and η_{oil} are the aqueous and oil phase viscosities, ΔP_{aq} and ΔP_{oil} are the pressure drops over the aqueous and oil inlets, and l_{aq} and l_{oil} are the lengths of the aqueous and oil inlets. The equation assumes all channels have

the same height, which is usually the case with devices made via photolithography. Assuming the pressure terms cancel, the remaining constant terms can be grouped and form the slope the calibration, *m*.

$$\alpha = m\eta_{aq} \tag{B4}$$

$$m = \left(\frac{w_{oil}}{w_{aq}}\right)^3 \left(\frac{h + w_{aq}}{h + w_{oil}}\right)^2 \left(\frac{1}{\eta_{oil}}\right)\left(\frac{l_{aq}}{l_{oil}}\right) \tag{B5}$$

B2. PDMS T-Junction device construction.

PDMS T-junctions may be created using a molding technique involving the use of fused silica capillaries as molds to form cylindrical channels. This technique is useful for research groups who want to utilize microfluidics who don't have access to photolithography equipment and has been detailed in Chips and Tips, a blog dedicated to miniaturization in chemistry hosted by the Royal Society of Chemistry. (Burgoyne et al., 2010) Additional capillary molding techniques based on those previously published in Chips and Tips were developed and used to make devices for several projects detailed in this chapter, and are detailed below.

T-junctions with various dimensions are formed by first mixing PDMS with curing agent in a 10:1 ratio by mass. This PDMS is then poured into a glass dish, degassed in a vacuum desiccator, and cured on a hotplate at 100 ℃ until it solidified. Fused silica capillaries are positioned in the shape of a T on this surface, as shown in Figure 32A. Prior to positioning, the tip of the capillary which formed the side branch of the T is sanded to a point using a sanding disc attached to a rotary cutting tool. The tip of this point is then blunted by sanding to on sand paper by hand so that it had the shape of a truncated cone, as shown in Figure 33A. To hold capillaries in place, a small drop of uncured PDMS is placed over the capillaries where they intersect, as shown in Figure 32B. After degassing, this drop of PDMS is cured on a hotplate. Uncured PDMS is then poured over the entire surface to entirely submerge the molding capillaries. After degassing this second PDMS layer is heat cured on a hotplate, as shown in Figure 32C.

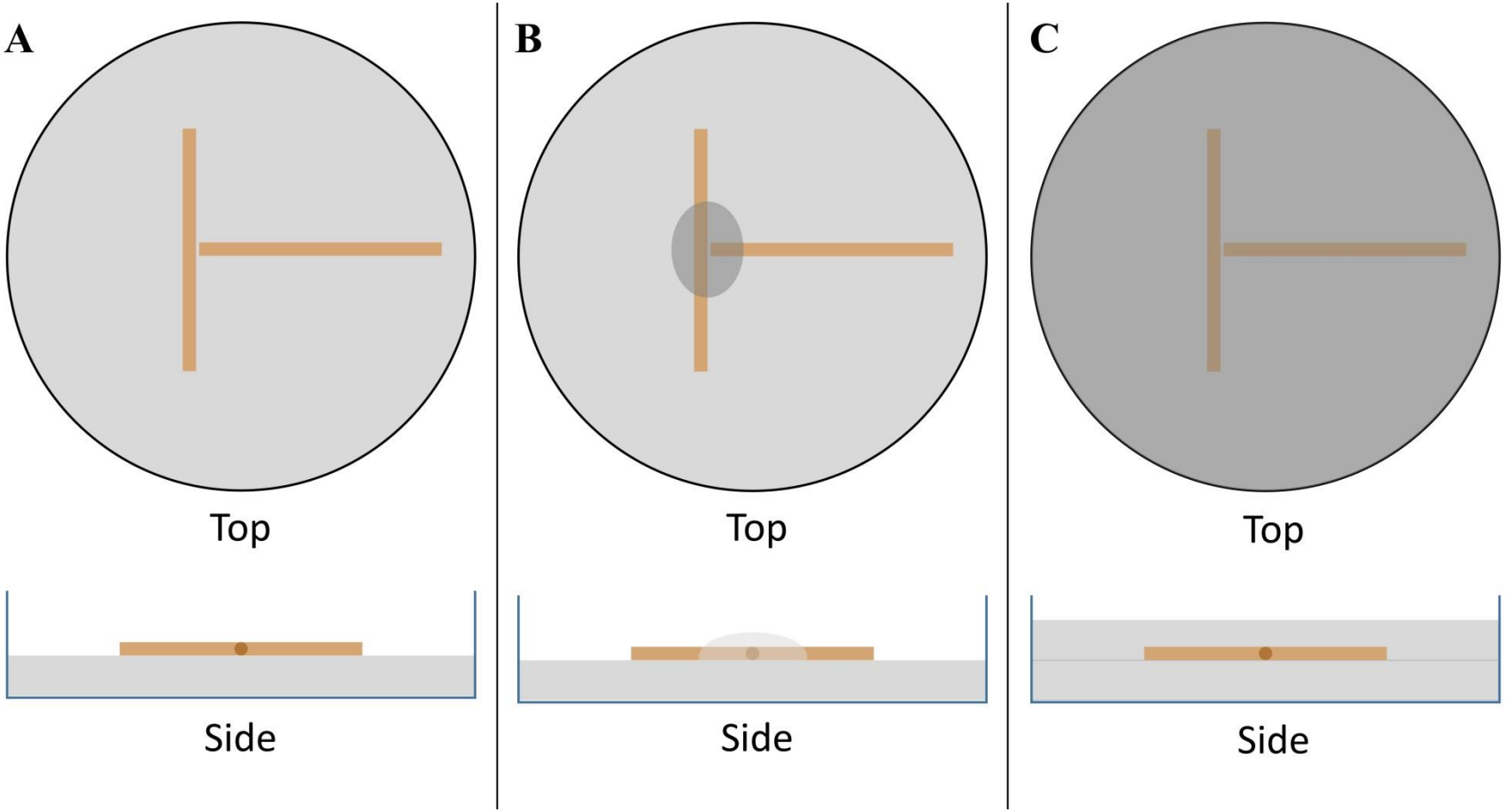

Figure 32: Capillary molding technique for fabrication of PDMS microfluidic devices with cylindrical channels. (A) Capillaries are placed on a cured PDMS surface in a dish in the shape of a T. (B) A drop of uncured PDMS is placed over the capillaries and cured to hold them in place. (C) A second layer of PDMS is formed by pouring uncured PDMS into the dish, submerging the molding capillaries.

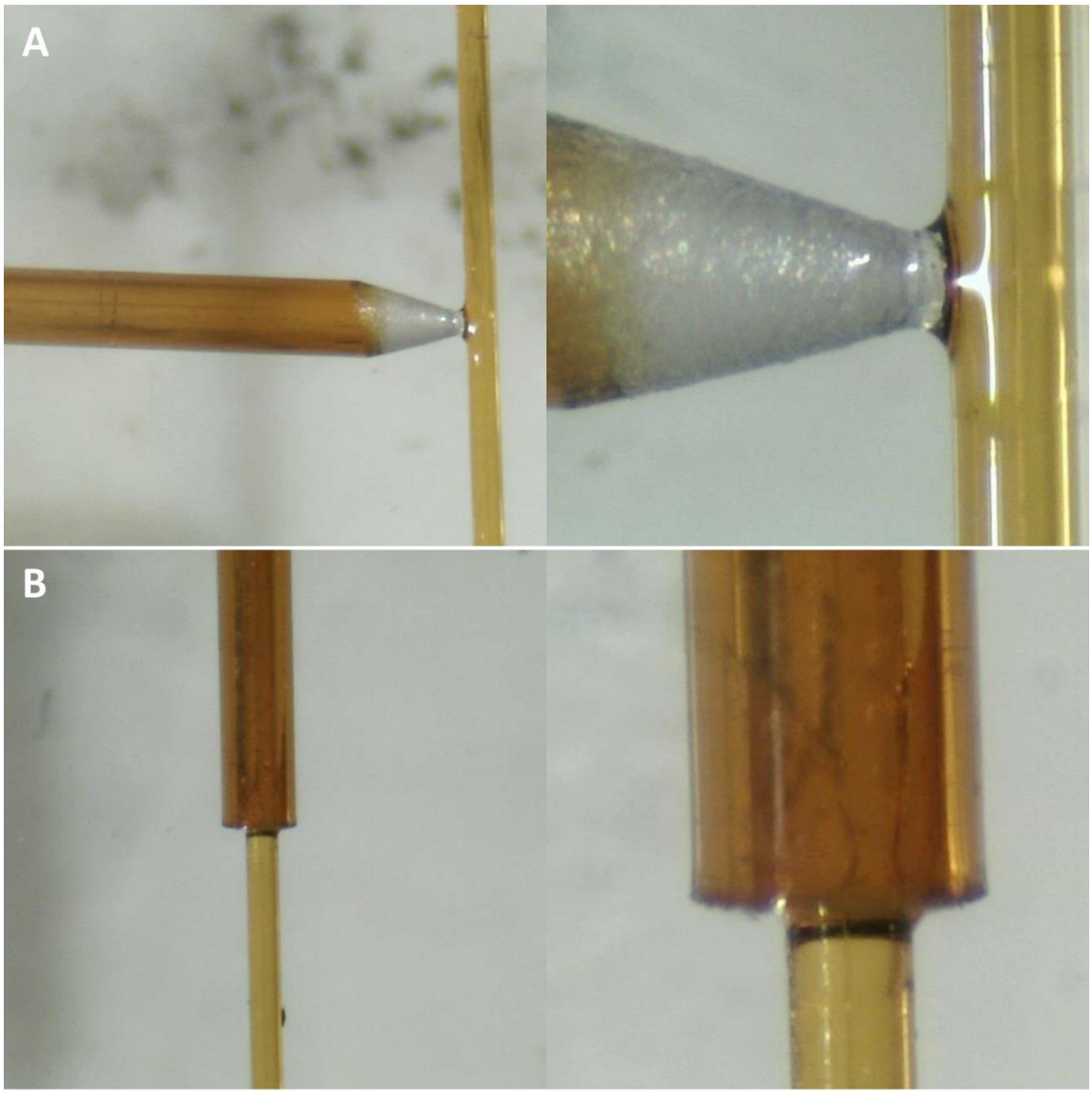

Figure 33: Images of capillary mold features. (A) A 360 μm o.d. capillary with the tip sanded into the shape of a truncated cone placed in the shape of a T with a 150 μm o.d. capillary. Epoxy is used to form a connection between the two capillaries. (B) A taper built by threading a piece of a 360/180 μm o.d./i.d. capillary over a 150 μm o.d. capillary. The tip of the 360 μm o.d. capillary has been sanded flat and epoxy is used to fill the space between the two capillaries.

After molding, capillaries must be removed to leave behind cylindrical channels. Cuts are made around capillaries with a flat razor, as shown in Figure 34A. Care must be taken to cut around the capillaries, and not through them. After cuts are made the capillaries can be pulled out from the edge of the device, as shown in Figure 34B. Because PDMS fills the small gap between the two capillaries, a thin wall of PDMS will exist between the resulting channels. On installing a capillary at the side branch of the device, it is important to push the capillary all the way into the main channel. This breaks the thin wall of PDMS, connecting the channels. The installed capillary can then be pulled back so that it just barely protrudes into the junction space. This avoids the creation of a PDMS flap from the thin PDMS wall, which can impede flow. Devices with 90, 150, or 360 μm i.d. channels can be made with this molding technique depending on the o.d. of the capillaries used. Various wires can also be purchased with other diameters.

Fully connected channels can be formed by applying a small drop of epoxy to the truncated cone tip of the mold capillary, as seen in Figure 33A. This is done after placing capillaries in the shape of a T but before fixing them in place with a PDMS drop. Only enough epoxy should be applied to wet the surface of the capillaries, and small amounts of excess epoxy will be pulled up into the mold capillary by capillary action. After the epoxy dries the junction can be fabricated as described above. When removing capillaries, the side branch capillary should be removed before the main branch capillary to avoid leaving epoxy debris in the channel.

Tapers can be formed in channels to allow interfacing of larger o.d. capillaries with smaller on-chip channels. Tapers can be formed by threading smaller o.d. capillaries through larger o.d. capillaries, as shown in Figure 33B. Prior to assembly, the end of the large i.d. capillary should be sanded flat using a rotary cutting tool first, then with sand paper by hand. To ensure the smaller i.d. capillary is centered, it is important to use the smallest i.d. available for the larger o.d. capillary while still allowing the smaller i.d. capillary to be threaded through the larger one. Tapers from 360 μm down to 150 μm and 90 μm were

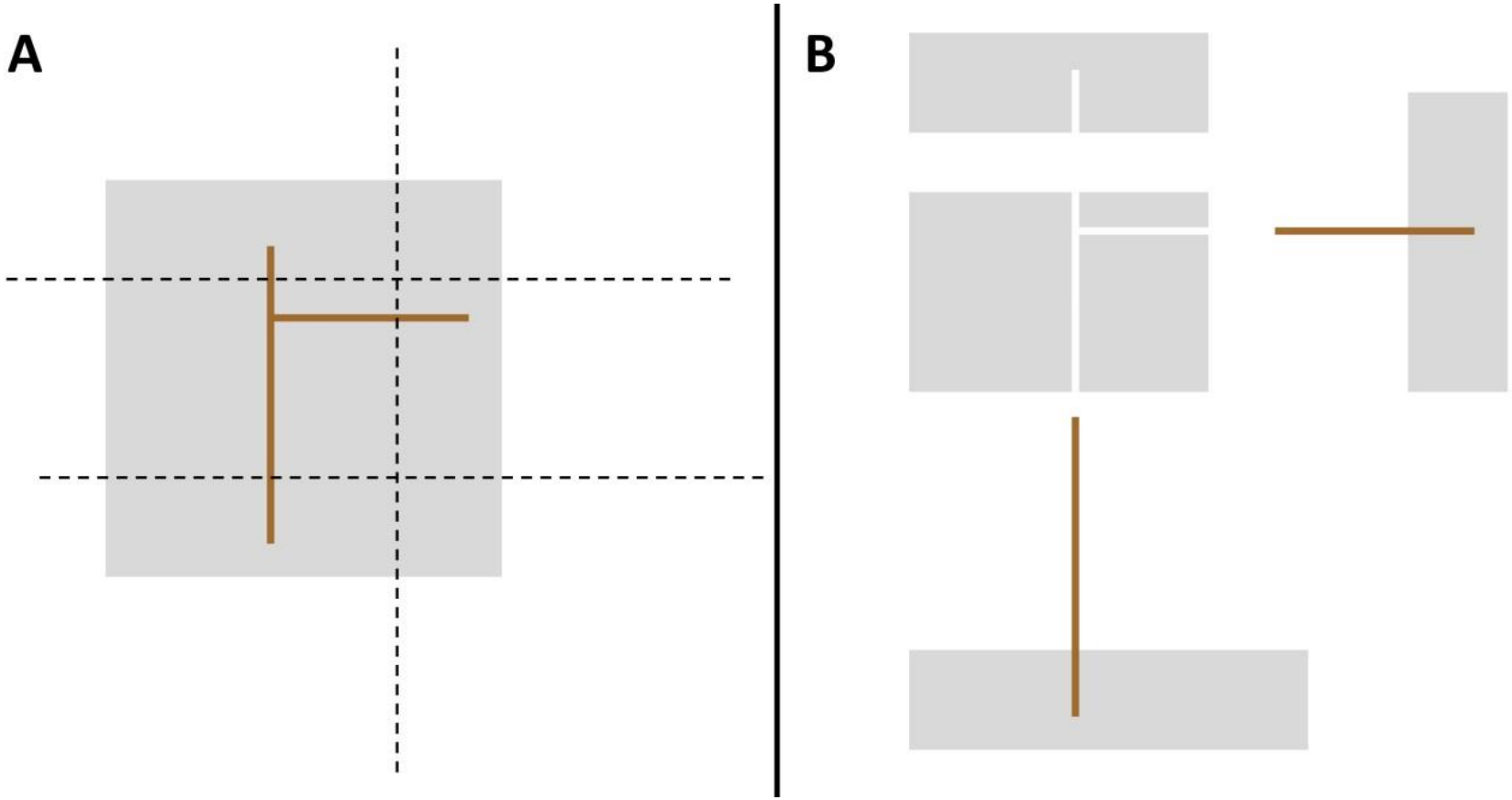

Figure 34: Removal of mold capillaries. (A) PDMS is first with a flat razor as shown by the dotted lines. Cuts are made around the mold capillaries, and care is taken not to cut through the capillaries. (B) Capillaries are pulled out of the device, leaving behind cylindrical channels in the shape of a T.

made this way. Typically the two capillaries of a junction must be the same diameter. If different diameters are used, the truncated cone tip of the side branch will go above or below the main channel capillary and no connection will be made. The use of 360 μm tapers at both ends of a molding capillary used for a main channel raises it off the surface of the PDMS slightly. This allows 360 μm o.d. capillaries to be used as the side branch of the junction.

Several issues can arise in the fabrication process originating from debris in channels. Molding capillaries should be cleaned with ethanol or another solvent prior to use. This is especially important when sanding capillaries, as any glass dust which is not washed away will become embedded in the PDMS channel, which can affect surface properties of the PDMS. Often PDMS will fill the small gap between the two capillaries used to mold a taper, which can leave behind a PDMS flap when capillaries are removed. This flap may also break off and become debris in the channel. To avoid this, epoxy can be applied over the channel mold capillary, and then the taper capillary can be slid over top of this epoxy. Only enough epoxy to wet the surface should be used. Epoxy sometimes breaks off capillaries and forms debris in channels. Channels can sometimes be cleaned of debris by first lubricating them with PFD, then threading a clean capillary of the same diameter used for molding in one end of the channel and out the other. Another problem often arises when PDMS is cured for too long. This hardens the PDMS, making it slightly brittle. Molding capillaries tend to strip or break channels when removed, causing roughened surfaces on the interior wall of the channel. To avoid this, mold capillaries should be removed slowly by wiggling the mold capillary back and forth as it is slowly pulled out.

B3. Viscosity corrections for laboratory temperature.

Temperature is an extremely important variable to control in viscosity measurements because slight changes in lab temperature may have a large impact on sample viscosity. Often the viscosities of standards are only known at specific temperatures, which restrict the temperatures at which sample

measurements may be easily performed. Rather than controlling temperature while performing calibrations, ambient temperature was measured using a thermocouple and fits of temperature vs. viscosity data were used to calculate viscosity of all standards at the ambient room temperature. These calculated viscosities were used for constructing calibration curves and calculating theoretical slope of calibration curves.

The LINEST function of Excel was used along with viscosity vs. temperature data for various aqueous glycerol solutions available in the literature (Segur and Oberstar, 1951) to devise the set of polynomial fit equations of the form $\eta=aT^3+bT^2+cT+d$, as shown in Figure 35. Fit parameters for the glycerol solutions used are reported in Table I. The oil phase viscosity was used in calculations related to calibration curve predictions, and had to be similarly adjusted for room temperature. For white mineral oil standards a 3rd order polynomial fit of viscosity vs. temperature data available from the manufacturer was performed, as shown in Figure 36. Fit parameters for white mineral oil standards are reported in Table II. An Arrhenius plot of viscosity vs. temperature data for PFD available in the literature (Haszeldine and Smith, 1951) was constructed and used along with the measured room temperature to perform viscosity adjustments, as seen in Figure 37.

B4. References

Han, Z.; Tang, X.; Zheng, B. A PDMS Viscometer for Microliter Newtonian Fluid. J. Micromechanics Microengineering 2007, 17 (9), 1828–1834.

Haszeldine, R. N.; Smith, F. 129. Organic Fluorides. Part VI. The Chemical and Physical Properties of Certain Fluorocarbons. J. Chem. Soc. 1951, 603.

Segur, J. B.; Oberstar, H. E. Viscosity of Glycerol and Its Aqueous Solutions. Ind. Eng. Chem. 1951, 43 (9), 2117–2120.

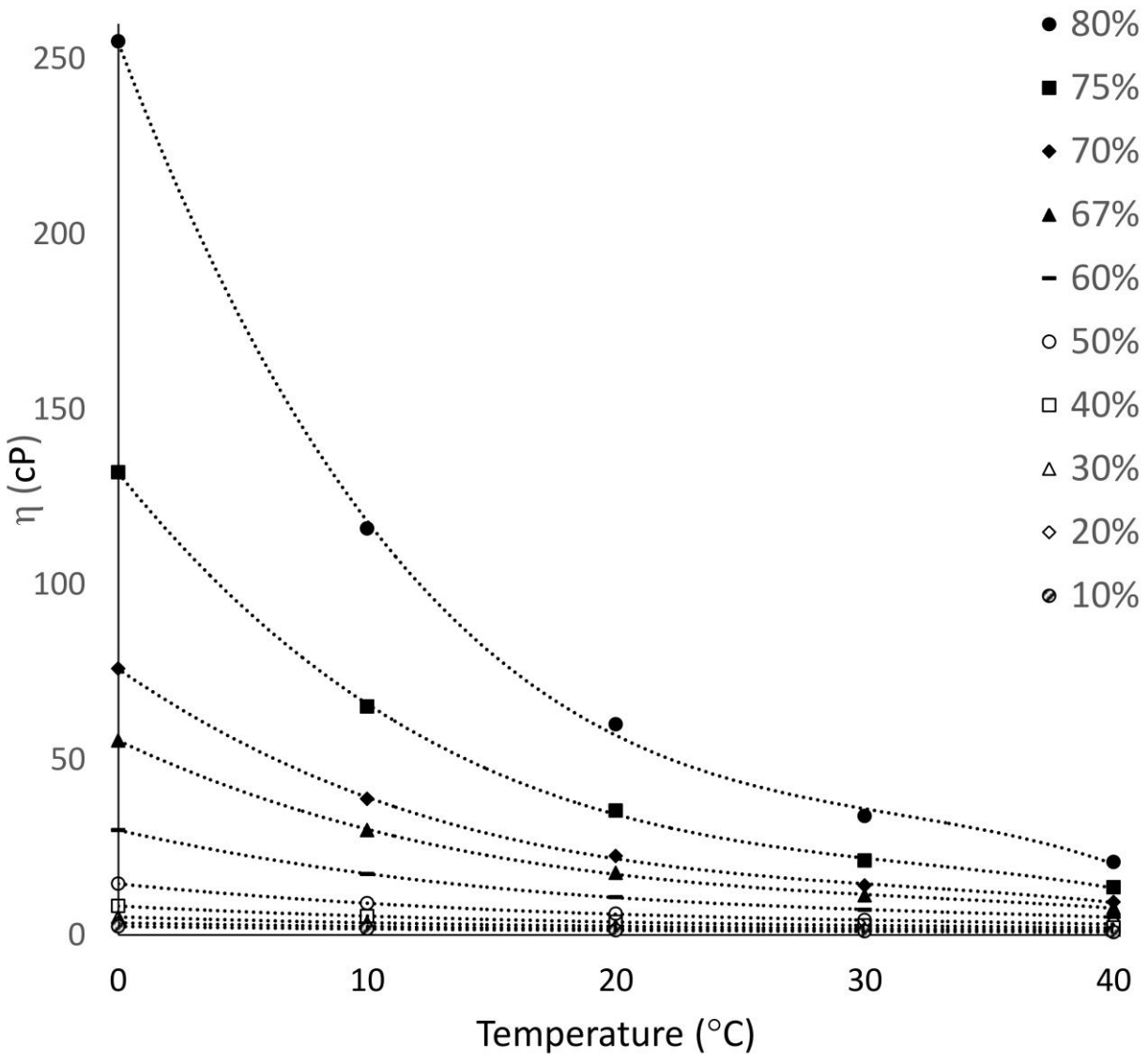

Figure 35: A plot of viscosity vs. temperature for glycerol solutions (10%-80% wt/wt) obtained from the literature. (Segur and Oberstar, 1951) A 3rd order polynomial fit was performed on the data using the LINEST function of Excel.

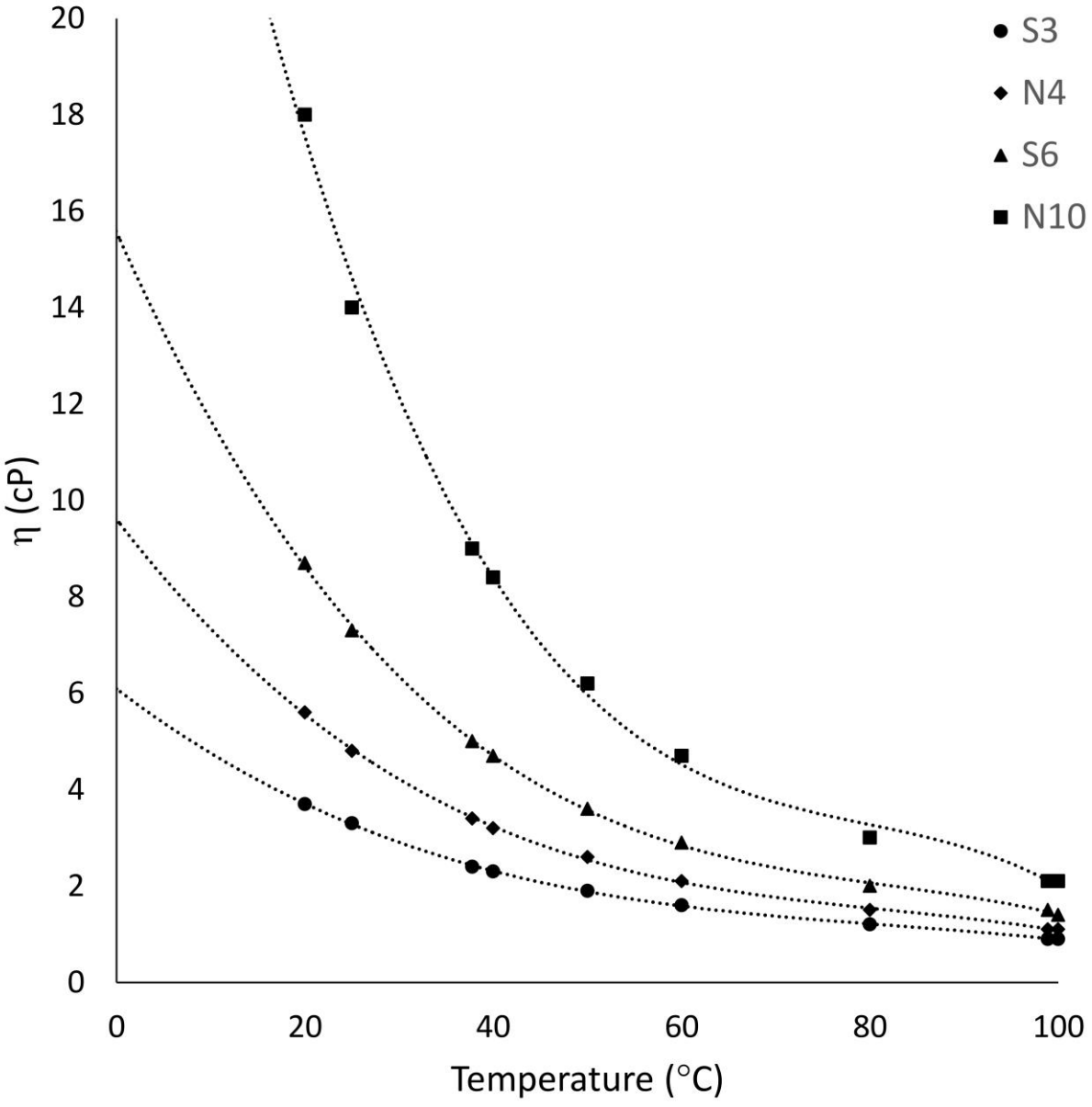

Figure 36: A plot of viscosity vs. temperature for white oil mineral standards obtained from the manufacturer. A 3rd order polynomial fit was performed on the data using the LINEST function of Excel.

Table I: LINEST 3rd order polynomial fit parameters for glycerol solution temperature vs. viscosity data available in the literature. (Segur and Oberstar, 1951) These parameters were used with a function of the form $\eta=aT^3+bT^2+cT+d$ to predict glycerol standard viscosities at the measured room temperature.

wt%	a	b	c	d	R^2
10	-1.6×10^{-5}	1.79×10^{-3}	-8.6×10^{-2}	2.439	1.000
20	-2.08×10^{-5}	2.49×10^{-3}	-1.256×10^{-1}	3.440	1.000
30	-3.7×10^{-5}	4.2×10^{-3}	-2.02×10^{-1}	5.14	1.000
40	-7.3×10^{-5}	8.05×10^{-3}	-3.59×10^{-1}	8.2460	1.000
50	-1.6×10^{-4}	1.7×10^{-2}	-7.1×10^{-1}	1.458×10^{1}	1.000
60	-3.7×10^{-4}	3.9×10^{-2}	-1.59	2.99×10^{1}	1.000
67	-9×10^{-4}	8.8×10^{-2}	-3.3	5.54×10^{1}	1.000
70	-1.4×10^{-3}	1.4×10^{-1}	-4.9	7.6×10^{1}	1.000
75	-2.53×10^{-3}	2.5×10^{-1}	-8.8	1.32×10^{2}	1.000
80	-6×10^{-3}	5.5×10^{-1}	-1.9×10^{1}	2.54×10^{2}	0.999

Table II: LINEST 3rd order polynomial fit parameters for temperature vs. viscosity data of white mineral oil viscosity standards available from the manufacturer. These parameters were used with a function of the form $\eta=aT^3+bT^2+cT+d$ to predict viscosities at the measured room temperature.

Standard	a	b	c	d	R^2
S3	-6.5×10^{-6}	1.6×10^{-3}	-1.49×10^{-1}	6.09	1.000
N4	-1.1×10^{-5}	2.8×10^{-3}	-2.5×10^{-1}	9.6	0.999
S6	-2.0×10^{-5}	5.0×10^{-3}	-4.4×10^{-1}	1.56×10^{1}	1.000
N10	-6×10^{-5}	1.3×10^{-2}	-1.1	3.5×10^{1}	0.997

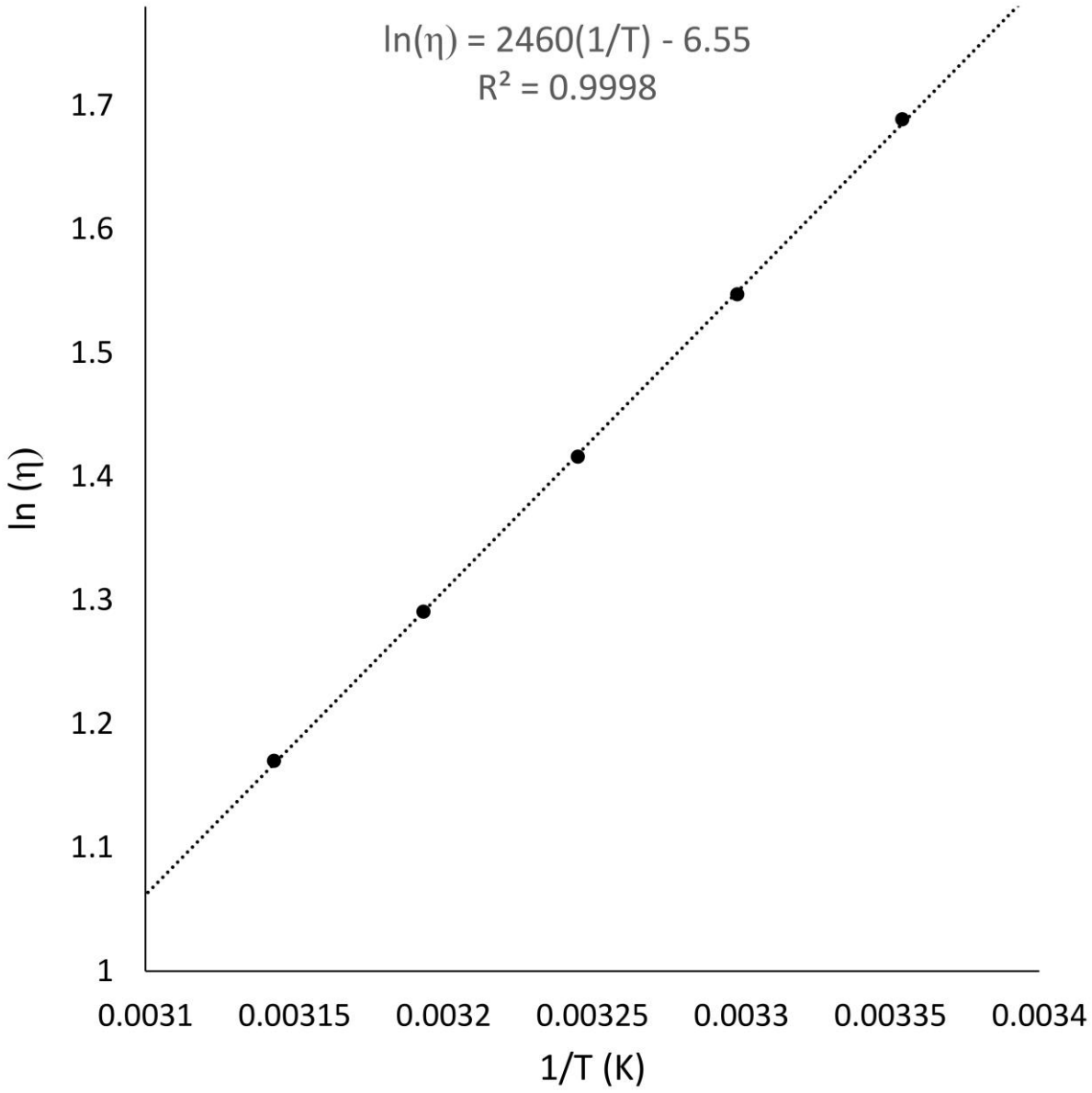

Figure 37: An Arrhenius plot constructed using temperature and viscosity (cP) values obtained from the literature. (Haszeldine and Smith, 1951) The fit equation was used to determine the PFD phase viscosity at the measured room temperature for each experiment.

VITA

NAME: Michael Francis DeLaMarre

EDUCATION: Ph.D, Analytical Chemistry, 2015

University of Illinois at Chicago

B.S., Professional Chemistry, 2009

Grand Valley State University

TEACHING EXPERIENCE: **Teaching Assistant •**

University of Illinois at Chicago

Chemistry and Life (CHEM 100)

General Chemistry 1 (CHEM 112)

General Chemistry 2 (CHEM 114)

Honors General Chemistry 1 (CHEM 116)

Honors General Chemistry 2 (CHEM 118)

Analytical Chemistry (CHEM 222)

Chemical Separations (CHEM 528)

Adjunct Professor

Grand Valley State University

General Chemistry 1 (CHM 115)

Quantitative Analysis (CHM 222)

HONORS: Deans List, GVSU

Recipient of the 2014 Fall TA Appreciation Award in Chemistry

PUBLICATIONS (PEER-REVIEWWED)

Flaherty, R. J.; Nshime, B.; DeLaMarre, M.; DeJong, S; Scott, P.; Lantz, A. W. Cyclodextrins as Complexation and Extraction Agents for Pesticides From Contaminated Soil. *Chemosphere*. **2013**. 91, 912-920.

DeLaMarre, M. F.; Shippy, S. A. Development of a Simplified Microfluidic Injector for Analysis of Droplet Content via Capillary Electrophoresis. *Anal. Chem*. **2014**. 86, 10193-10200.

DeLaMarre, M. F., Keyzer, A., Shippy, S. A. Development of a Simple Droplet-based Microfluidic Capillary Viscometer for low-viscosity Newtonian fluids. *Anal. Chem*. **2015**. 87, 4649–4657.

PRESENTAIONS

Estimation of pesticide-cyclodextrin association constants by affinity capillary electrophoresis. Poster presentation at Pittcon 2009 (McCormick Place, Chicago, IL, March 2009).

A computational exploration of binding between pesticides and native cyclodextrins. Poster presentation at the 13th Midwest Undergraduate Computational Chemistry Conference (Northwestern University, Evanston, IL, July 2009).

A computational exploration of binding between pesticides and native cyclodextrins. Poster presentation at the West Michigan Regional Undergraduate Science Research Conference (Van Andel Institute, Grand Rapids, MI, October 2009).

Replicate analysis of undiluted hemolymph from a single fruit fly. Oral presentation at Pittcon 2013 (Pennsylvania Convention Center, Philadelphia, PA, March 2013).

Development of a Droplet-Based Microfluidic Viscometer. Poster presentation at the 11TH Annual CBC Symposium (University of Chicago, Chicago, IL, October 2013).

Development of a segmented flow based viscosity sensor. Oral presentation at Pittcon 2014 (McCormick Place, Chicago, IL, March 2014).

A simple injector for droplet content analysis via capillary electrophoresis. Poster presentation at CBC Tech Day: Cutting-Edge Technologies — Driving Science Forward (Prentice Women's Hospital Conference Center, Chicago, IL, June 2014).

WORK EXPERIENCE

Research Assistant | Grand Valley State University | Allendale, MI | May 2008 to Aug 2008

Research Topics: Determination of affinity constants via CE and NMR as well as computational modeling of inclusion complexes

Chemistry Stockroom | Grand Valley State University | Allendale, MI | Sept 2008 to Oct 2009

Duties: Solution and lab preparation and chemical/equipment inventory